MODIFICATION OF BISMUTH PHOSPHATE BASED NANOMATERIAL AS SUNLIGHT SENSITIVE PHOTOCATALYSTS

NG JIT JANG

MASTER OF ENGINEERING SCIENCE

FACULTY OF ENGINEERING AND GREEN TECHNOLOGY

UNIVERSITI TUNKU ABDUL RAHMAN

JUNE 2021

MODIFICATION OF BISMUTH PHOSPHATE BASED NANOMATERIAL AS SUNLIGHT SENSITIVE PHOTOCATALYSTS

By

NG JIT JANG

A dissertation submitted to the Faculty of Engineering and Green Technology,

Universiti Tunku Abdul Rahman,

in partial fulfillment of the requirements for the degree of

Master of Engineering Science

February 2021

Modification of Bismuth Phosphate based Nanomaterial as Sunlight Sensitive Photocatalysts

ABSTRACT

This research highlighted Bismuth Phosphate ($BiPO_4$) photocatalysts' modification to enhanced solar-driven photocatalysis for endocrine-disrupting compounds. Pure $BiPO_4$ was prepared through a simple sol-gel approach. Incorporation of graphitic carbon nitride (g-C_3N_4) and Silver (Ag) nanoparticles onto $BiPO_4$ via simple thermal deposition and photodeposition, respectively. The $BiPO_4$/g-C_3N_4 was synthesized with different g-C_3N_4 loading weight percentages: 0.5wt%, 1.5wt% and 2.5wt% whereas the weight percentages for Ag/$BiPO_4$ were 1.0wt%, 3.0wt% and 5.0wt%. Field Emission Scanning Electron Microscope (FESEM) and High-Resolution Transmission Electron Microscopy (HRTEM) investigated the surface morphology while the XRD investigated the structure and particle size of as-prepared $BiPO_4$/g-C_3N_4 and Ag/$BiPO_4$. UV-vis Diffuse Reflectance Spectra (UV-DRS) spectrum depicted increment of dopant loading weight percentages leads to increasing light absorption of as-synthesized photocatalysts. Furthermore, Time-Resolved Photoluminescence (TRPL) spectra show the charge carrier lifetime increased with high dopant loading. Photodegradation of 2,4-Dichlorophenols (2,4-DCPs) was conducted to investigate the photodegradation efficacy of $BiPO_4$/g-C_3N_4 and Ag/$BiPO_4$ in the presence of natural sunlight. With 1.0g of each photocatalyst being added into 50ppm of 2,4-DCPs. The results concluded that both g-C_3N_4 and Ag nanoparticles present in $BiPO_4$ manage to enhance the photocatalytic activity under sunlight irradiation compared to pure $BiPO_4$. In

addition, the results for photodegradation of 2,4-DCPs matched well with the characterization results of UV-DRS and TRPL spectra which agreed that the highest dopant loading weight percentage of g-C_3N_4 and Ag possesses the highest light absorption and lowest recombination rate of electron-hole pairs. After 90 min of 2,4-DCPs photodegradation, 0.5wt%, 1.5wt% and 2.5wt% of $BiPO_4$/g-C_3N_4 achieved 55%, 77% and 100% of 2,4-DCP removal, respectively. On the other hand, 69%, 66%, 76% of 2,4-DCPs photodegradation efficiency after 5hr were achieved by 1.0wt% Ag/$BiPO_4$, 3.0wt% Ag/$BiPO_4$, and 5.0wt% Ag/$BiPO_4$, respectively. The enhanced photodegradation of 2,4-DCPs under sunlight irradiation is mainly contributed by prolonged the charge carriers' lifetime by incorporation with g-C_3N_4. Moreover, the existence of g-C_3N_4 further enhanced the light absorbance to harvest the entire sunlight energy and produce excessive active radicals. Besides that, Ag's incorporation acted as an electron trap to separate the electrons and holes produced in $BiPO_4$ under sunlight excitation. This separation prevented the generated electrons and holes from recombining to form heat. Therefore, Ag nanoparticles' presence retarted the recombination formation, allowing free electrons to react and form active radicals responsible for the degradation of 2,4-DCPs. A scavenging test was conducted to determine the active radical species. Superoxide anion (O_2^-) and holes (h^+) radical are the main active radicals for $BiPO_4$/g-C3N4. Similarly, O_2^- and hydroxyl (•OH) radicals are responsible for the photodegradation for Ag/BiPO4. A recycling test was conducted to investigate the stability and reusability of both as-synthesized photocatalysts. Photodegradation efficiency of 2.5wt% $BiPO_4$/g-C_3N_4 and Ag/$BiPO_4$ retained above 70% after four cycles of photocatalytic activities.

ACKNOWLEDGEMENT

First of all, I would like to express my utmost gratitude to my supervisor, Ts. Dr. Leong Kah Hon for guiding me patiently throughout the whole research period. My sincere thanks also go to my co-supervisor, Dr. Sim Lan Ching for providing help and support during the research study. Furthermore, I am truly grateful to Universiti Tunku Abdul Rahman for assisting my research work by providing research fund UTARRF (IPSR/RMC/UTARRF/2018-C2/L03).

I would also like to extend my thanks to the technicians of the laboratory, Mr. Choong Man Kit, Ms. Ng Suk Ting, Mr. Yong Yzyy Jeng, and Pn. Zila Binti Mohd Tahir of the Faculty of Engineering and Green Technology (FEGT) department for their help in offering me their resources in running the program.

Finally, I am extremely grateful to my parents for their love and encouragement throughout my research study. I would like to offer my special thanks to Ms. Hoo Sie Kei, who also offer me reassurance and support constantly.

APPROVAL SHEET

This dissertation entitled "**MODIFICATION OF BISMUTH PHOSPHATE BASED NANOMATERIAL AS SUNLIGHT SENSITIVE PHOTOCATALYSTS"** was prepared by NG JIT JANG and submitted as partial fulfillment of the requirements for the degree of Master of Engineering Science at Universiti Tunku Abdul Rahman.

Approved by:

_____

(TS. DR. LEONG KAH HON) Date:……..

Supervisor

Department of Environmental Engineering

Faculty of Engineering and Green Technology

Universiti Tunku Abdul Rahman

_____

(DR. SIM LAN CHING) Date:……..

Co-supervisor

Department of Chemical Engineering

Lee Kong Chian Faculty of Engineering and Science

Universiti Tunku Abdul Rahman

FACULTY OF ENGINEERING AND GREEN TECHNOLOGY

UNIVERSITI TUNKU ABDUL RAHMAN

Date: _____

SUBMISSION OF DISSERTATION

It is hereby certified that **Ng Jit Jang** (ID No: **18AGM07449**) has completed this dissertation entitled "MODIFICATION OF BISMUTH PHOSPHATE BASED NANOMATERIAL AS SUNLIGHT SENSITIVE PHOTOCATALYSTS" under the supervision of Ts. Dr. Leong Kah Hon (Supervisor) from the Department of Environmental Engineering, Faculty of Engineering and Science, and Dr. Sim Lan Ching (Co-Supervisor) from the Department of Chemical Engineering, Lee Kong Chian Faculty of Engineering and Science.

I understand that University will upload a softcopy of my dissertation in pdf format into UTAR Institutional Repository, which may be made accessible to UTAR community and public.

Yours truly,

_____

(Ng Jit Jang)

DECLARATION

I, NG JIT JANG hereby declare that the dissertation is based on my original work except for quotations and citations which have been duly acknowledged. I also declare that it has not been previously or concurrently submitted for any other degree at UTAR or other institutions.

_____

(NG JIT JANG)

Date _____

TABLE OF CONTENTS

LIST OF TABLES

LIST OF FIGURES

LIST OF SYMBOLS AND ABBREVIATIONS

Symbols/Abbreviations

$^{\bullet}O_2^-$	Superoxide radical anion
$(NH_4)H_2PO_4$	Ammonium dihydrogen phosphate
$^{\bullet}OH$	Hydroxyl radicals
2,4-DCP	2,4-dichlorophenol
2,4-DCPs	2,4-Dichlorophenols
ACN	Acetonitrile
$AgNO_3$	Silver Nitrate
AOPs	Advanced oxidation processes
Bi	Bismuth
$Bi(NO_3)_3{\bullet}5H_2O$	Bismuth (III) nitrate pentahydrate
$BiPO_4$	Bismuth Phosphate
BQ	Benzoquinone
C	Carbon
C	Concentration
$C_2H_8O_7$	Absolute ethanol
CB	Conduction band
C_o	Initial Concentration
CO_2	Carbon dioxide
DMSO	Dimethylsulfoxide
e^-	Electrons
E_C	Energy of free electrons
E_{CB}	Band edge potential for conduction band

EDCs	Endocrine Disrupting Compounds
EDTA	Ethylenediaminetetraacetic acid disodium salt
EDX	Electron dispersive X-ray
E_g	Band-gap energy
eV	Electron volt
E_{VB}	Band edge potential for valance band
FESEM	Field Emission Scanning Electron Microscope
FTIR	Fourier Transform Infrared Spectra
g-C_3N_4	Graphitic Carbon Nitride
h^+	Photogenerated holes
H_2O	Water
HPLC	High Performance liquid chromatography
HRTEM	High-Resolution Transmission Electron Microscopy
hv	Photon energy
IPA	Isopropanol
k	Apparent rate constant of first order reaction
LSPR	Localized Surface Plasmon Resonance
MB	Methylene Blue
MO	Methylene Orange
N	Nitrogen
NHE	Normal hydrogen electrode
NIR	Near infra-red
O	Oxygen
O_2	Oxygen molecules

OH^{--}	Hydroxyl ions
P	Phosphorus
PO_4^{3--}	Phosphate group
R	diffuse reflectance
R^2	Correlation coefficient
RhB	Rhodamine B
Silver	Ag
SPR	Surface Plasmon Resonance
TiO_2	Titanium dioxide
TRPL	Time Resolved Photoluminescence
UV	Ultraviolet Light
UV-DRS	UV-vis Diffuse Reflectance Spectra
VB	Valence band
WHO	World Health Organization
wt%	Weight percentage
X	Electronegativity of semiconductor
XRD	X-ray Diffraction

CHAPTER 1

INTRODUCTION

1.1 Background

Water is an essential element for all life on Earth. Roughly 71% of Earth's surface is covered with water and 60% of the adult human body is water. Water also played an important role in domestic water usage for indoor and outdoor household purposes such as cooking, bathing, watering and drinking. All living organisms on Earth are dependent on water to complete their life cycles. In this modern era, increased industrialization and urbanization due to the high human population resulted in severe water contamination. Although humans acknowledged the importance of water, yet 80% of the untreated world's wastewater is discharged into the water bodies, leading to reduced availability of clean water and increased water-borne disease, jeopardizing the health of all living organisms (Denchak, 2018). The agricultural sector, which plays a pivotal role in the world economy's growth, is the leading cause of water contamination (Stoyanova and Harizanova, 2019). Fertilizers, animal waste, and pesticides are washed into water bodies, such as lakes and rivers, by rain causing severe water pollution (Singh et al., 2020). Therefore, proper and effective wastewater treatments are required to overcome the drastic increment of water pollution.

Implementing wastewater treatment is to dispose of industrial and human effluents without having an adverse impact on human health and the environment. The conventional wastewater treatment method has been applied to overcome water-related environmental problems. Traditional wastewater treatment can be categorized into biological, chemical and physical processes that can eliminate or reduce the wastewater pollutants before being discharged into water bodies. Physical processes remove solids or organic matter from wastewater, whereas biological and chemical processes involve removing dissolved matter and chemicals or heavy metals (Samer, 2015). Biological processes have drawbacks such as requiring close monitoring of microorganisms, optimum environment required, slow processes and sludge bulking (Crini and Lichtfouse, 2019). On the other hand, chemical processes especially advanced oxidation processes have superior advantages such as no production of sludge, rapid degradation of pollutants, and mineralization of contaminants, which attracted the attention of researchers (Chong et al., 2010). Among these advanced oxidation processes, heterogeneous photocatalysis emerged as a promising wastewater treatment that possesses the ability to convert a wide variety of water persistent organic compounds into harmless, biodegradable compounds by utilizing semiconductor catalysts.

Photocatalysis can be defined as the change in the rate of a chemical transformation under the light's action in the presence of a catalyst that absorbs light and is involved in the chemical reactions (Serpone et al., 2012; Serpone and Emeline, 2012). Photocatalyst, most of the semiconductors, is a substance that absorbs light and acts as a catalyst to alter chemical reactions. A good

photocatalyst possesses criteria such as low cost, environmentally friendly, ability to utilize a wide range of the solar spectrum, chemically and physically stable (Deng et al., 2019). In general, photocatalysis can be illustrated by four steps: (i) generation of electron-hole pairs attributed to light absorption; (ii) photoexcited electron charges separation; (iii) allocation of electrons and holes to the surface of photocatalysis; and (iv) occurrence of redox reaction photocatalyst surface. The excited electron is used for reduction, whereas the generated hole is used for oxidation. In part (iii), recombination of photogenerated electrons and photogenerated holes will occur and dissipate the harnessed energy into heat or light emission (Zhang, Zhang and Gong, 2014; Gershon et al., 2015; Xiang, Cheng, and Yu., 2015). In these modern days, photocatalysis technology has been studied extensively. It is an effective way to solve the arising problems related to environmental pollution and its ability to utilize the abundance of renewable solar energy from the sun.

Titanium dioxide (TiO_2) is one of the conventional photocatalysts that was vastly studied due to its superior characteristics such as nontoxicity, excellent chemical stability and low cost (Lee and Schmuki, 2014). However, TiO_2 has a large bandgap energy (~3.2 eV) that only allows absorption of UV light which is a huge drawback as sunlight contains less than 5% of UV light. In addition, the low separation efficiency of photogenerated electron-hole pairs is another flaw of TiO_2 that limits the photodegradation performance (Qi et al., 2017). Thus, it is crucial to search for alternative semiconductors.

Therefore, introducing Bismuth Phosphate ($BiPO_4$), a potential alternative to conventional semiconductor, is an innovative inorganic non-metal salt of bismuth-based oxy-acid semiconductor that has exceptional characteristics, such as non-poisonous, good crystallinity, biologically and chemically stable. (Jun et al., 2015; Jun et al., 2016; Lei, Changcun and Jing, 2011). It has been stated that $BiPO_4$ possessed a higher photocatalysis in comparison to Titanium Oxide (TiO_2) on organic degradation due to the lower recombination rate of $BiPO_4$ (Xu et al., 2013). This is attributed to the inductive effect of a phosphate group (PO_4^{3-}) that allows the efficient separation of photogenerated electron-hole pairs (Pan and Zhu, 2010). To further enhance its unique properties, it will be modified with graphitic carbon nitride (g-C_3N_4) and silver nanoparticles (Ag). g-C_3N_4 is a semiconductor with a relatively small energy bandgap contributing to better visible light absorbance and the polymeric nature of g-C_3N_4 facilitating the effective generation of photoexcited electron-hole pairs (Ong et al., 2016). Apart from that, Ag nanoparticles are a noble metal that possesses Surface Plasmon Resonance (SPR) that enhances the visible light absorption leading to increment of quantum yield during the photocatalysis process (Nainanni, Thakur and Chaskar, 2012). Thus, the incorporation of both g-C_3N_4 and Ag nanoparticles will further enhance the light absorbance ability of $BiPO_4$ and prolong the lifespan of the charge carriers of $BiPO_4$ during the photodegradation of pollutants.

1.2 Problem Statement

Endocrine Disrupting Compounds (EDCs) is an exogenous substance or mixture that alters the endocrine system's function, causing a negative impact on the health of an organism (Locatelli et al., 2016). It possesses the ability to directly activate or inactivates the endocrine target receptors via inhibition of endocrine function. Exposure to EDCs also leads to disturbance of hormone synthesis (Guilivo et al., 2016). Pesticides, industrial chemicals, heavy metals, herbicides, artificial sweeteners, pharmaceuticals and personal care products are some of the main sources for EDCs (Tijani et al., 2013). According to the World Health Organization (WHO) stated that EDCs might cause breast cancer, abnormal growth patterns, and neurodevelopment delay in children (Mehrabani-Zeinabad, 2016). Conventional treatment methods, such as coagulation-flocculation process, activated carbon process, adsorption process, biological trickling filter and membrane filtration, had been used for the removal of EDCs with low satisfactory results with secondary pollutants (Choi et al., 2006; Westerhoff et al., 2005; Huang et al., 2016; Bellona and Drewes, 2007; Badia-Fabregat, Oller and Malato, 2015). Contrarily, advanced oxidation processes achieved promising results with complete mineralization of EDCs into carbon dioxide and water without any secondary pollutants (Dolar et al., 2012; Choquette et al., 2014).

Bismuth Phosphate proves to have advantages as compared to conventional semiconductors, however, $BiPO_4$ still needs to overcome some of its drawbacks, namely poor absorptive performance in visible light, and wide

energy bandgap. Consequently, it is essential to enhance $BiPO_4$ for better visible light absorption and hinder the recombination rate of electron-hole pairs.

Various modification methods had been conducted to improvise $BiPO_4$ (Pan et al., 2012; Zong et al., 2015; Liu et al., 2014; Huang et al., 2013). Incorporation of small energy bandgap graphitic carbon nitride ($g\text{-}C_3N_4$) broadens the solar absorbance of $BiPO_4$, which enables $BiPO_4$ to harness more energy and prolong the lifetime of charge carriers, leading to improved photodegradation efficiency (Zou et al., 2016; Li et al., 2014). Furthermore, photodeposition of noble metal onto the surface of $BiPO_4$ yields positive results. Noble metals could generate Surface Plasmon Resonance (SPR) that leads to disturbance in the surrounding matrix's dielectric constant, enabling visible light absorption (Nainani and Chaskar, 2012). In addition, noble metal also can function as an electron trapping epicenter that enables the rapid transmission of an electron from $BiPO_4$ retarding the recombination rate of photoexcited electron-hole pairs, prolonging the photocatalytic efficacy of $BiPO_4$ (Wu et al., 2009). Hence, this illustrates that both dopants can enhance $BiPO_4$ in terms of visible light absorption and hinder the recombination rate of photogenerated electrons.

1.3 Objectives

The current study's objectives are to mitigate the specified drawbacks of $BiPO_4$ by incorporating graphitic carbon nitride (g-C_3N_4) that will improve the visible light absorbance and promote electron-hole pairs separation efficiency. Separately, doping with noble metal (silver) enhances the visible light absorbance through the SPR effect. Subsequently, modified $BiPO_4$ photocatalysts were assessed by photodegradation of 2,4-Dichlorophenols (2,4-DCPs) a form of EDC pollutant in the presence of sunlight. This study includes the sustainability evaluation of as-prepared photocatalyst in environmental remediation applications. The objectives of this study are:

1. To modify bismuth phosphate through incorporation with silver nanoparticles and graphitic carbon nitride.
2. To characterize the synthesized photocatalysts for their various physical and chemical properties.
3. To study the mechanism and electron mobility of the synthesized photocatalyst through photodegradation of 2,4-Dichorophenol under sunlight irradiation.
4. To study the reusability of the modified nanocomposite photocatalysts.

CHAPTER 2

INTRODUCTION

2.1 Endocrine Disrupting Compounds

Endocrine Disrupting Compounds (EDCs) is defined as exogenous chemicals, or a mixture of chemicals that interfere with any aspect of hormone action (Zoeller et al., 2012). The importance of hormones in the human body is crucial as they play an important role in reproductive function, regulation of response to various nutritional demands, body and brain development, adaptation, and maintenance of bodily processes and health (Gore et al., 2014). EDCs are widely used in various fields such as plastics, cleaning products, cosmetics, pesticides and industrial processes (Kabir et al., 2015). For the benefits of industrial use, EDCs are designed not to decay quickly and have long half-lives (Lubrano et al., 2013). Some EDCs will break down into different harmful compounds through metabolism. Thus, EDCs can be easily detected in food, daily products and the environment, even for those EDCs that were being banned in the past (Yang et al., 2006). According to the World Health Organization (WHO), EDCs may cause breast cancer, abnormal growth patterns, and neurodevelopment delay. One of the standard ways of EDCs entering the human body system is through bioaccumulation. In highly contaminated environments, industrial chemicals leach into the soil, air, and water bodies. Microorganisms and plants will be consumed traces of EDCs, then

moving up the food chain, the human will end up with the highest concentrations of EDCs in the body system. The exposure route of EDCs into the human body is mainly via oral consumption, inhalation, dermal contact, biological transfer from the placenta or mother's milk. Table 2.1 contained some information regarding the type of EDCs and their sources. Therefore, it is undeniable that the removal of EDCs is essential for current and future society.

Table 2.1: Sources or uses of EDCs (Gore et al., 2014)

EDCs	Sources/Uses
Phthalates, triclosan, parabens, pesticide	Cosmetic, personal care products, anti-bacterial, sunscreens, medications, intravenous tubing.
Dichlorodiphenyltrichloroethane (DDT), chlorpyrifos, vinclozolin, pyrethroids	Pesticides used in agriculture, home, public disease vector control.
Brominated Flame Retardants (BFRs)	Flame retardants for household furniture.
Bisphenol A (BPA), phenol	Food and beverage containers.
Polychlorinated biphenyls (PCBs)	Contaminated soil or groundwater by industrial waste or pesticides.

2.1.1 2-4 Dichlorophenols

2-4 Dichlorophenols (2,4-DCPs) is classified under endocrine-disrupting compounds that are concerned by researchers and the public. It is a colourless crystalline solid with a medicinal odour. The routes of human exposure to 2,4-DCPs are inhalation, dermal contact and ingestion. 2,4-DCPs is widely used as a precursor in the production of herbicides and pesticides. The agricultural sector that is heavily dependent on herbicides and pesticides is one of the main contributors to the presence of 2,4-DCPs in water bodies. Herbicides and pesticides are washed into the river or lake by rainwater and storm runoff.

Furthermore, discharge of 2,4-DCPs into water bodies by the industrial sector involved in the production of herbicides and pesticides also contributed to the increased risk of 2,4-DCPs exposure to the surrounding environment (Czapicka, 2004; Ahlborg et al., 1980). As 2,4-DCPs is water recalcitrant, it will be retained in the water bodies for a long duration (Huang et al., 2017). Although conventional wastewater treatment methods have been implemented to treat 2,4-DCPs, the effort remains futile as those methods have severe drawbacks such as the production of secondary pollutants and high maintenance cost (Ahn et al., 2002; Tomei et al., 2012; Ranjit et al., 2008; Matafonova et al., 2006; Bhishma and Kumar, 2015). Table 2.2 displayed various conventional treatment method for 2,4-DCPs.

Table 2.2: Conventional methods for 2,4-DCPs treatment.

Method	**Target**	**Condition**	**Removal efficiency (%)**	**Reference**
Enzyme Treatment using laccase	2,4-DCP	-Reaction time 1 day	88	Ahn et al., 2002
Two Phase Partitioning Bioreactors	2,4-DCP	-Reaction time 500 min -feed of 320mg/L	91	Tomei et al., 2012
Fenton's method	2,4-DCP	-H_2O_2 (580mg/L) -Fe^{2+} (20mg/L) -pH (2.5) -120min	71	Ranjit et al., 2008
Aeration Pond	2,4-DCP	-Reaction time 2 days	56-77.6	Matafonova et al., 2006
Biodegradation	2,4-DCP	-Reaction time 20days	75-80	Bhishma and Kumar, 2015

2.2 Heterogeneous Photocatalysis

Heterogeneous photocatalysis emerged as a promising wastewater treatment method for degrading a wide variety of harmful water persistent organic compounds without producing secondary pollutants. It is a form of advanced nanotechnology that utilizes photocatalysts that harvest energy from the light source to degrade recalcitrant water compounds to form carbon dioxide and water as end products. Previous studies done on photocatalysts are shown in Table 2.3. In general, the photocatalytic process mechanism initiated when the photocatalyst harnessed sufficient energy from light irradiation to photoexcite electrons to bridge through the energy bandgap from the valence band to the conduction band, leading to the generation of electron-hole pairs. Electron (e^-) was produced at the conduction band, whereas holes (h^+) were generated at the valence band (Molinari et al., 2002). The photogenerated electron will reduce oxygen (O_2) to superoxide anion radicals ($\bullet O_2^-$) at the conduction band. At the valence band, the photogenerated holes will convert water (H_2O) and hydroxyl ions (OH^-) into hydroxyl radicals ($\bullet OH$). Both radicals are essential in the removal of organic pollutants existing in wastewater. The mechanism below shows the general equation for the occurrence of an oxidation-reduction process during photocatalysis (Coronado et al., 2013):

$$Photocatalyst + hv \rightarrow {e^-}_{CB} + {h^+}_{VB} \quad (1)$$

$${e^-}_{CB} + O_2 \rightarrow \bullet {O_2}^- \quad (2)$$

$${h^+}_{VB} + H_2O \rightarrow \bullet OH + H^+ \quad (3)$$

$$h^{+}_{VB} + OH^{-} \rightarrow \bullet OH \quad (4)$$

$$Pollutant + \bullet OH, \bullet O_2^{-} \rightarrow CO_2 + H_2O \quad (5)$$

Table 2.3: Various types of photocatalysts applied in wastewater treatments.

Photocatalyst	Experimental Conditions	Pollutant	Efficiency	Reference
NiAl	The double Ni/Al layered double hydroxides were synthesized via the co-precipitation method. The experiment was carried out under UV light sources.	2,4-DCP	Attained 94% degradation efficiency after 150 min of irradiation.	Ramos-Ramírez et al., 2020
$BiVO_4$/RGO	A one-step hydrothermal method was used to synthesized $BiVO_4$/RGO. The experiment was conducted under UV light	2,4-DCP	Attained 55% degradation efficiency after 6h of irradiation.	Tu et al., 2020
TiO_2/ZnO/SnO_2	TiO_2/ZnO/SnO_2 was obtained through the co-precipitation method. The experiment was carried out under UV light.	2,4-DCP	Attained 72% degradation efficiency under 120min of irradiation.	Ali et al., 2020
EG/CeO_2	EG-CeO_2 was synthesized using impregnation ultrasonic agitation. The experiment was carried out under UV light.	2,4-DCP	Attained 98.7% degradation efficiency under 180min irradiation.	Mafa, Mamba and Kuvarega, 2020

Table 2.3: Various types of photocatalysts applied in wastewater treatments (continued).

Photocatalyst	Experimental Conditions	Pollutant	Efficiency	Reference
ZrO_2/TiO_2	The sol-gel method was used to synthesize ZrO_2/TiO_2. The experiment was carried out under UV light	2,4-DCP	Attained 99% degradation efficiency under 150min irradiation.	Guerrero-Araque et al., 2020
$CeO/g\text{-}C_3N_4$	Preparation of $CeO/g\text{-}C_3N_4$ via wet-chemical solution method. The experiment conducted under Visible light.	2,4-DCP	Attained 57% degradation efficiency under 120min irradiation.	Humayun et al., 2019
$S\text{-}TiO_2$	$S\text{-}TiO_2$ was synthesized by the incorporation of sulfur cations into the lattice of TiO_2. Experiments were carried out under UV light.	2,4-DCP	Attained 97% degradation efficiency under 480min irradiation.	Alalm et al., 2018

The photocatalyst is defined as a solid that can stimulate reactions in the presence of light without involving itself in the overall reaction (Mills, Davies and Worsley, 1993). A good photocatalyst possesses criteria such as low cost, environmentally friendly, ability to utilize a wide range of the solar spectrum, chemically and physically stable (Deng et al., 2019). Table 2.4 shows several photocatalysts and their respective bandgap energy. Despite the superior characteristics of photocatalysts, synthesis of highly efficient light-driven photocatalyst remains a challenge as there are drawbacks that required mitigation such as poor absorptive performance, large size, and rapid recombination of photoexcited electron-hole pairs, which hinder the photodegradation efficiencies of photocatalysts (Habisreutinger et al., 2013; Wang et al., 2014).

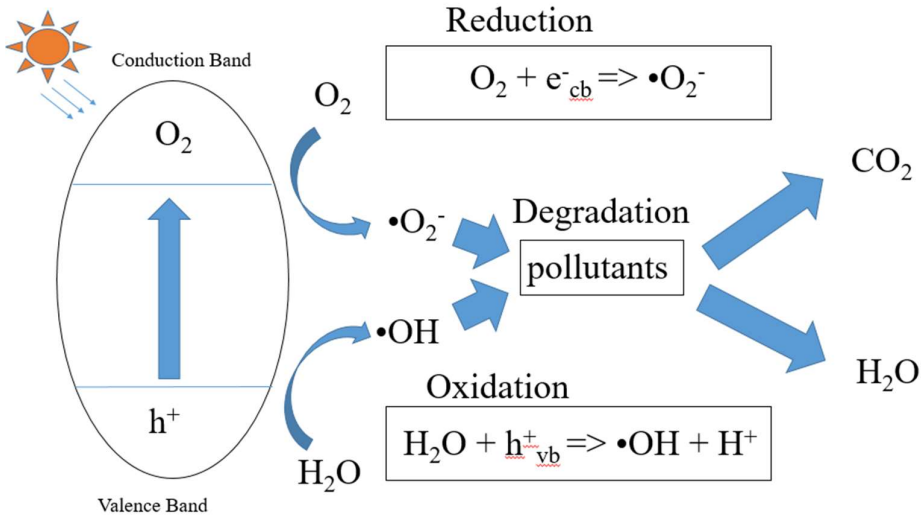

Figure 2.1: Basic mechanism of heterogeneous photocatalysis (Yang and Wang, 2018).

Table 2.4: Various photocatalysts with their respective energy bandgap (Mamba and Mishra, 2016; Wang et al., 2019).

Photocatalyst	Bandgap energy (eV)	Photocatalyst	Bandgap energy (eV)
Fe_2O_3	2.3	ZnO	3.2
TiO_2(rutile)	3.0	TiO_2(anatase)	3.2
WO_3	2.8	CdS	2.5
ZnS	3.7	CeO_2	2.94
SnO_2	3.5	Cu_2O	2.7
$BiPO_4$	3.5	g-C_3N_4	1.7

2.3 Bismuth Phosphate ($BiPO_4$)

Bismuth Phosphate ($BiPO_4$) is a novel inorganic non-metallic salt of oxy-acid photocatalyst with excellent criteria, such as non-poisonous, good crystalline, biologically and chemically stable (Lv et al., 2013; Pan and Zhu, 2011). This has attracted the attention of researchers and various experiments were conducted and reported that $BiPO_4$ possessed high photodegradation ability as compared to commercial Titanium Oxide (TiO_2), contributed by the superior inductive effect of a phosphate group (PO_4^{3-}) which enable high electron hole-pairs separation. (Xu et al., 2013; Pan and Zhu, 2010). It was reported that $BiPO_4$ can be present in 3 types of crystalline phases: (i) monoclinic (nMBIP), (ii) mMBIP, and hexagonal (HBIP) (Darkwah et al.,

2019). Each crystal phase possessed the same energy bandgap and positions of band edge (Pan et al., 2011b). In addition, eight oxygen atoms adjoining a single bismuth atom whereas a phosphorus atom was encircled by four oxygen atoms for each of the crystal's phases. However, each crystal phase exhibited different photocatalytic degradation efficiency as their separation efficacy of the photogenerated electron-hole pairs is different (Pan et al., 2011b). Monoclinic $BiPO_4$ (nMBIP) is reported to have the highest photocatalytic performance due to the scattered Bi-O polyhedron and P-O tetrahedron bond length (Pan et al., 2011a). In addition, research found that $CaIn_2O_4$ and $SrIn_2O_4$ that possessed large dipole moments exhibited higher photocatalytic performance. (Sato et al., 2003). Thus, monoclinic $BiPO_4$ (nMBIP) owns the most partial PO_4^{3-} tetrahedron attributed by the large dipole presence in $BiPO_4$ which resulted in superior photocatalytic performance in energy conversion, environmental remediation, and environmental applications.

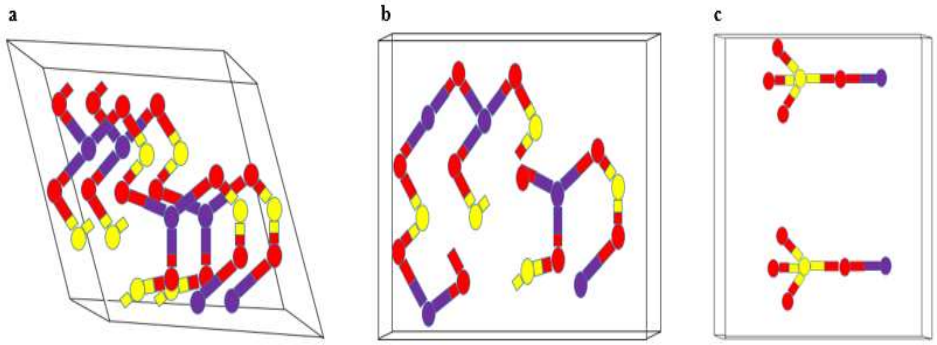

Figure 2.2: **Three $BiPO_4$ crystal structures: (a) HBIP (b) nMBIP (c) mMBIP (Pan and Zhu, 2015).**

2.3.1 Synthesis method for $BiPO_4$

According to past studies, different synthesis routes had different impacts on the morphology, crystalline structure, chemical and physical properties of $BiPO_4$. There are various types of $BiPO_4$ structures, such as nanowires, nano-rods, nanocubic, nanofiber and nano-flowers, that can be acquired by different approaches of synthesis method which resulted in different levels of photocatalytic activities. Figure 2.3 displays the different structures that were successfully synthesized by other researchers (Geng et al., 2005; Liu et al., 2014; Lin et al., 2007).

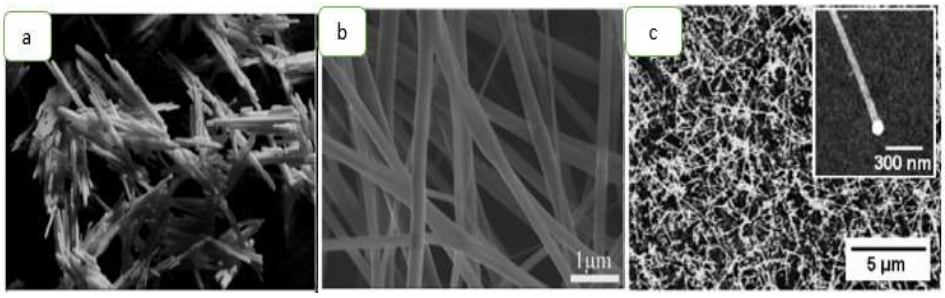

Figure 2.3: Various morphology of $BiPO_4$: (a) Nanorods (b) Nanofiber (c) Nanowire (Geng et al., 2005; Liu et al., 2014; Lin et al., 2007)

A solvothermal method is a chemical reaction of solvents confined in a totally closed vessel with controlled temperature via heating and autogenous pressure condition which help the solutions to attain their respective critical points (Byrappa and Yoshimura, 2001). The solvothermal method is a common synthesis approach for powdery nanostructure compounds that utilized organic solvent (Walton, 2002). The technique begins with an injection of a proper

percentage of reagent mixture and a precursor, followed by stirring (Zhong and Mirkovic, 2011). Next, the mixture is relocated into a sealed vessel autoclave for the crystallization process with controlled temperature, set duration and self-generated pressure. Temperature and time held vital roles in specific component crystallization (Yoshimura and Byrappa, 2008). Organic solvents that were widely applied in the solvothermal synthesis procedure are 1,4-butanediol, methyl alcohol, amines, and toluene. In addition, the solvothermal method owns various significant benefits such as (i) low-pressure reaction requirement, (ii) relatively low temperature for reaction, (iii) ability to control highly hydro sensitive precursors, (iv) simple determination of morphology and crystal phase end products and (v) high purify of end products (Liu et al., 2016). Furthermore, the synthesis of $BiPO_4$ adopting the solvothermal method possessed higher photocatalytic activities as surface oxygen vacancy generated via 450°C calcination leading to the enhancement of photogenerated charges' lifetime, which resulted in 2 times better of Methylene Blue photodegradation efficiency as compared to commercial TiO_2 (Wei et al., 2015). There was also a research on controlled solvothermal synthesis method by varying reaction time which successfully synthesized $BiPO_4$ that has higher photocatalytic efficacy with controlled morphology and crystal phases, possessed nano-cocoon and monoclinic nanorods structures (Xue et al. 2009).

The hydrothermal synthesis method is mainly for the production of the powdery nanostructure end product. Crystalline nanostructure was prepared by an appropriate ratio of the mixture of precursors and suitable agents into a solvent. Next, the mixture was contained in sealed stainless steel lined Teflon

autoclave and transferred into the oven for a set amount of heating duration, pressure and temperature. The internal pressure of the Teflon autoclaves and the amount of solutions dictated by the specific temperature (M. Malekshahi Byranvand et al., 2013). Hydrothermal is similar to the solvothermal method in terms of dissolving most of the materials with appropriate solvent by altering the pressure and temperature. However, the primary solvent utilized by hydrothermal is distilled water. Subsequently, the hydrothermal method is favored for the synthesis of $BiPO_4$ with nanorods structure. It was reported that nanorods $BiPO_4$ synthesized via hydrothermal method exhibited superior Methylene Blue photodegradation performance in comparison with ultrasound irradiation method in terms of the efficiency of photoexcited holes and lifetime of charge carrier (Cheng et al., 2014). Furthermore, $BiPO_4$ prepared by hydrothermal method attained complete removal of phenol in 4 hours (Liu et al., 2013). In addition, $BiPO_4$ that was synthesized via hydrothermal method performed twofold better at photodecomposition of benzene in comparison to TiO_2 (Long et al., 2012).

Microwave irradiation is known as a favorable practice in the synthesis process of photocatalyst as it is able to control the crystalline and structure of $BiPO_4$ which is significant for tuning of photocatalytic properties. The microwave irradiation method has advantages such as the microwave couples with the molecules that exist in the reaction mixture directly with the quick rise in temperature, fast reaction, and zero hazardous waste is produced due to the green synthesis process (Palou, 2007). The study of Li et al. (2011) reports $BiPO_4$ synthesized via microwave irradiation method with distinct

morphologies and size in its nanostructures exhibits superior efficacy in the methyl orange (MO) photodegradation. The above findings concluded $BiPO_4$ in hexagonal phases possessed better MO photodegradation activities compared to monoclinic phase $BiPO_4$. As present in the supercapacitor's studies of Vadivel et al. (2016), synthesizing $BiPO_4$ using the surfactant of Ethylenediaminetetraacetic acid (EDTA) through the simple microwave approach, the photocatalyst demonstrates superior cyclic stability. Its capacitance retention is found 92% after 500 cycles at a 1 Ag^{-1} current density (Vadivel et al., 2016). Apart from that, the hierarchical flower-like $BiPO_4$ microspheres are synthesized through the method of microwave-aided hydrothermal reaction with bismuth nitrate ($Bi(NO_3)_3$) and ionic liquid [C4 mim] [PF6] (1-butyl-3-methylimidazolium hexafluorophosphate) in the 160 °C water. The ionic liquid [C4 mim] [PF6] plays a dominant role as the raw materials of phosphorus, surface modified agent as well as template (Lv et al., 2015). The study shows that the modification of synthesized $BiPO_4$ with [C4mim] [PF6], attained 94% of RhB photodegradation in 1 hr UV irradiation, whereas the synthesized $BiPO_4$ without the modification of ionic liquid demonstrates 75% photodegradation efficiency under the same context.

With the many synthesis methods for $BiPO_4$ available, we adopted the sol-gel method compared to the rest because it is a chemical method that allows the production of particles with a defined size, dimension, structure and composition (Rao, Mukherjee and Reddy, 2017). Furthermore, the sol-gel method processes require low processing temperature and less energy for the synthesis of photocatalysts, making it economical and sustainable (Rao,

Mukherjee and Reddy, 2017). As mentioned above, a different synthesis method of photocatalyst will produce photocatalysts with a different structure that possesses the other photocatalytic ability. Furthermore, the sol-gel method has been widely applied to synthesise various photocatalyst namely, TiO_2, WO_3, SnO_2 and ZnO (Li, White and Lim 2004; Mahato et al., 2009; Gu et al., 2003; Bessière et al., 2001). Thus, applying the sol-gel method for synthesis is essential as this method provides better control over the shape and size of photocatalysts and yields and improves photocatalysis performance.

2.3.2 Modification of $BiPO_4$

Similar to other photocatalysts, $BiPO_4$ required additional modifications to improvise its photodegradation efficiency further. Despite having unique properties, $BiPO_4$ has low photo-sensing in visible and near-infrared region absorbance attributed by the wide energy bandgap which constrained the full utilization of the solar spectrum resulting in the limitation of $BiPO_4$ as a sustainable photocatalyst. Furthermore, it possesses a shorter charge carrier lifetime that increases the electron and hole potential to recombine and form heat. Therefore, modifications to $BiPO_4$ are required to mitigate their drawback. To date, some outstanding improvising approaches such as doping, heterojunction structure formation and phase junction are adopted on $BiPO_4$ [Zhu et al., 2014; Maeda and Domen, 2007; Guo et al., 2018]. Table 2.5 depicts different modification methods conducted on $BiPO_4$.

One of the methods to enhance the photocatalytic performance of $BiPO_4$ photocatalyst is phase junction, where the lifetime of the charged carrier can be prolonged. By utilizing the photocatalysts' band alignment with various phases and structures, phase junction aids the separation efficiency of photoexcited electrons and photogenerated hole pairs at the surfaces of photocatalysts. When the alignment of the photocatalyst's band edge is well-matched, the separation of photogenerated electron-hole pairs will occur efficiently and lead to the improvement of photocatalytic ability (Zhu et al., 2014; Guo et al., 2018; Wang and Li, 2018). Besides, heterojunction is a substitute method that helps to facilitate separation efficacy of photogenerated active electrons and photoinduced holes at the interface between $BiPO_4$ and the semiconductor as it is attributed to the band alignment or noble metal attributed to the Schottky junction barrier. Doping is one of the approaches that can retard the recombination rate and narrow the bandgap energy by introducing the element of either metal or non-metal into the lattice or surface or $BiPO_4$ to produce a donor or receptor. It is vital to select dopants with optimum concentration as the excessive concentration will achieve undesirable results of photocatalytic activity. As a case in point, the occurrence of the total surface coating was caused by excessive dopant loading, which restricts the photocatalytic degradation activities as the core photocatalyst is inhibited from the generation of photogenerated electron-hole pairs. Hence, the determination of optimum dopant loading concentration is essential in order to enhance the performance of pristine $BiPO_4$, for a vast improvement in photodegradation efficiency.

Table 2.5: Various studies on the modification of $BiPO_4$.

Modification	Synthesis Parameter	Application	Light Source	Efficiency	Reference
$Zn_3(PO_4)_2$	Co-precipitation, 900°C	Sulfadiazine photodegradation	UV	Achieved complete removal of sulfadiazine after 240min. The rate of mineralization of composite is 3 times of $Zn_3(PO_4)_2$ and 1.5 times of $BiPO_4$.	Naciri et al., 2020
BiOCl	facile in situ chemical transformation method, 80°C, 12h	Rhodamine B (RhB) photodegradation	UV	$BiPO_4$/BiOCl-40% completely decompose RhB in 45min. $BiPO_4$/BiOCl-40% performed 3.18 times higher than Pure BiOCl.	Zhang et al., 2020
Bi_2S_3	One-pot precipitation route, anion exchange	Photoreduction of toxic Cr (VI) to harmless Cr (III)	Visible light	$BiPO_4/Bi_2S_3$ synthesized in DEG attained 95% photoreduction of Cr (VI) to Cr (III) after 20min visible light irradiation.	Geioushy et al., 2020

Table 2.5: Various studies on the modification of $BiPO_4$ (continued).

Modification	Synthesis Parameter	Application	Light Source	Efficiency	Reference
$ZnAl_2O_4$	Co-precipitation and hydrothermal method, pH=1, 180°C, 24h, 60°C, 24h	Methylene Blue (MB) photodegradation	UV	1wt% $ZnAl_2O_4/BiPO_4$ degraded MB under UV irradiation 2.47 and 18.10 times faster than pure $ZnAl_2O_4$ and $BiPO_4$, respectively.	Tian et al., 2020
Carbon Dots (CDs)	Surface group-mediated nucleation reaction, 12 h standing, 60°C, 2h	reduction of 4-nitrophenol to 4-aminophenol	Visible light	reduction of 4-nitrophenol to 4-aminophenol is enhanced around 2.5 times under visible light irradiation, $CDs/BiPO_4$ showed better stability and reusability than $BiPO_4$.	Chang et al., 2020

In addition, solar energy is abundant energy that is distributed in UV (5%), visible (45%) and NIR (50%), which should be utilized. Artificial light will only provide a single light source, whereas solar energy will have three light sources. Thus, two noteworthy modification approaches are to be prioritized: extend the solar spectrum's absorption and enhance photoexcited electron separation for better photocatalytic performance. Therefore, incorporating graphitic carbon nitride (g-C_3N_4) and Silver (Ag) are selected to modify $BiPO_4$ in the current study.

2.4 Graphitic Carbon Nitride (g-C_3N_4)

The g-C_3N_4 is a 2-D π-conjugated polymeric semiconductor that owns narrow energy bandgap, physicochemical stability and simple synthesis (Ong et al., 2016). Figure 2.4 displayed the 2D structure and morphology of g-C_3N_4 (Zhang et al., 2013; Wen et al., 2017). g-C_3N_4 displayed better visible light absorption attributed to a 2.7eV small energy bandgap. The polymeric nature of g-C_3N_4 allows multiple excitations from the absorption of a single photon contributing to the effective generation of active radicals for the degradation of pollutants (Cui et al., 2016). Thus, g-C_3N_4 is used for the modification of different photocatalysts in other studies. Zhao et al. fabricated Sb_2MoO_6/g-C_3N_4 heterojunction through physical mixing method for 24h and calcination at 180°C for 2h. 7.5% Sb_2MoO_6/g-C_3N_4 achieved 94% photodegradation of rhodamine B (RhB) after 40min visible light irradiation and attained better H_2

evolution (Zhao et al., 2020). Furthermore, Wang et al. synthesized $Ba_5Nb_4O_{15}/BiPO_4$ by constructing heterojunction for efficient facilitation charge transfer. $Ba_5Nb_4O_{15}/BiPO_4$ (1:20) exhibited 2.345 times higher H_2 evolution in using visible light as the light source (Wang et al., 2019). Samsudin et al. enhanced $BiVO_4$ using g-C_3N_4 through a wet-impregnation method that minimized the recombination rate of the photo charge carrier. 0.8wt% g-$C_3N_4/BiVO_4$ exhibited 2.25 times H_2 evolution compared to unmodified $BiVO_4$ (Samsudin et al., 2020).

Apart from that, Ghattavi and Nezamzadeh-Ejhieh synthesized AgBr/g-C_3N_4 using the deposition-precipitation method. A visible light experiment was conducted to investigate the performance of AgBr/g-C_3N_4. It attained a high yield of methyl orange (MO) photodegradation contributed by a reduced recombination rate (Ghattavi and Nezamzadeh-Ejhieh, 2020). Liu et al. used a one-step calcination method to decorate g-C_3N_4 with Ag for broadening light absorbance and lower recombination rate of photoexcited electron and photogenerated hole. By utilizing visible light irradiation, Ag/g-C_3N_4 achieved 98.7% MO removal in 2h and fully converted 4-nitrophenol to 4-aminophenol in 70 s (Liu et al., 2020). Referring to the above studies regarding modification of different semiconductors using g-C_3N_4, it was deduced that incorporating g-C_3N_4 allows better visible light absorption and higher facilitating of photogenerated efficiency, resulting in bandgap improvement and retarding the recombination rate of photogenerated electrons.

Figure 2.5 shows the proposed photodegradation mechanism of Methylene Orange (MO) using g-C_3N_4 decorated TiO_2 (Zhang et al., 2017). Compared to TiO_2, g-C_3N_4 can harness energy from visible light irradiation to provide electrons hole pairs for TiO_2. Besides, the presence of g-C_3N_4 allows higher separation efficiency of electron-hole pairs as the photogenerated electron will be transferred from CB of g-C_3N_4 to CB of TiO_2 for reduction purpose whereas the photogenerated hole will be transported from VB of TiO_2 to VB of g-C_3N_4. This condition reduces the recombination rate of electron-hole pairs effectively resulting in higher photocatalytic performance. Subsequently, Wang et al. (2020) also utilized g-C_3N_4 incorporation for better photodegradation of p-nitrophenol using Fe doped ZnS ($Zn_{0.94}Fe_{0.04}S$) photocatalyst as shown in Figure 2.6. During solar light irradiation, both g-C_3N_4 and $Zn_{0.94}Fe_{0.04}S$ are involved in electron-hole pair generation, leading to the production of large amounts of electron-hole pairs for high-efficiency photodegradation. Due to CB position difference, photogenerated electrons tend to transfer from CB of g-C_3N_4 to CB of $Zn_{0.94}Fe_{0.04}S$ contributing to the occurrence of highly efficient reductive reaction at CB of $Zn_{0.94}Fe_{0.04}S$. On the other hand, the photogenerated holes at the VB of $Zn_{0.94}Fe_{0.04}S$, unable to oxidize H_2O/OH^- for the generation of •OH radicals due to edge potential lower than redox potential, are transported to VB of g-C_3N_4, allow recombination rate of photogenerated electrons and holes to slow down, providing a better p-nitrophenol degradation condition (Wang et al., 2020). Table 2.6 shows different past studies conducted on the modification of photocatalysts using g-C_3N_4. Hence, modification of $BiPO_4$ with g-C_3N_4 is expected to broaden solar spectrum absorbance and prolong the charge carriers' lifetime.

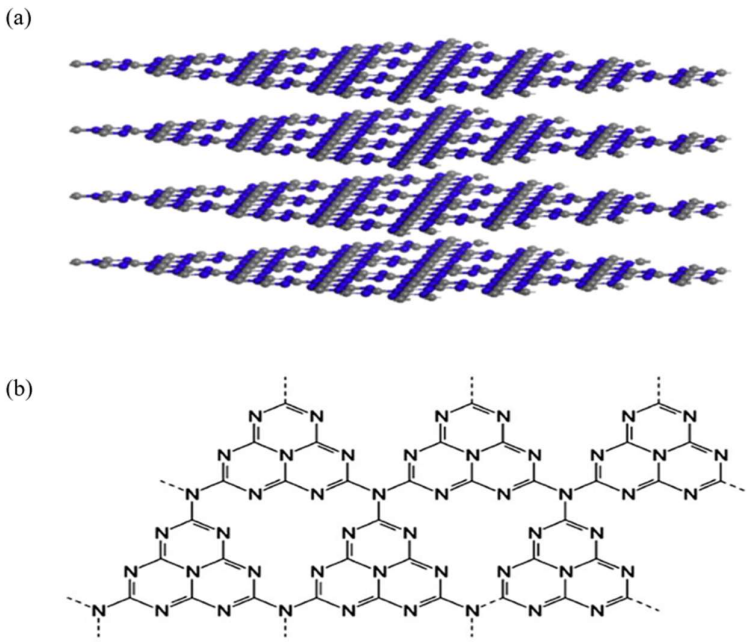

Figure 2.4: (a) 2D structure and (b) structure of g-C_3N_4 (Zhang et al., 2013; Wen et al., 2017).

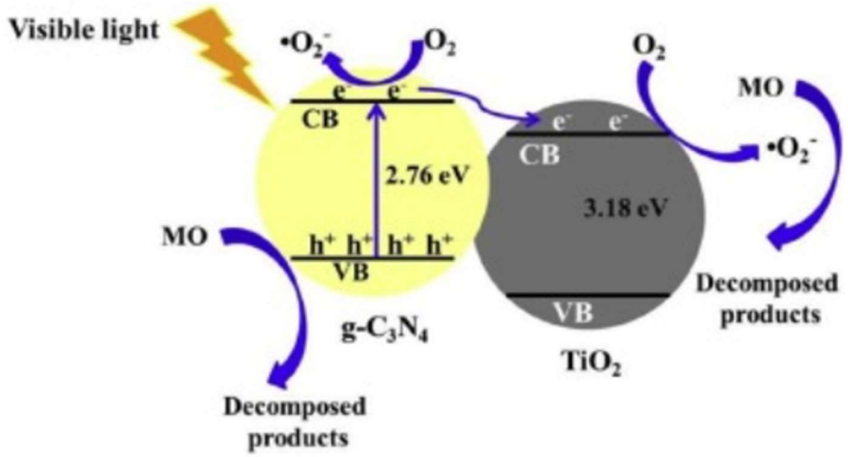

Figure 2.5: Proposed mechanism of MO degradation using g-C_3N_4/TiO_2 in the presence of visible light irradiation (Zhang et al., 2017).

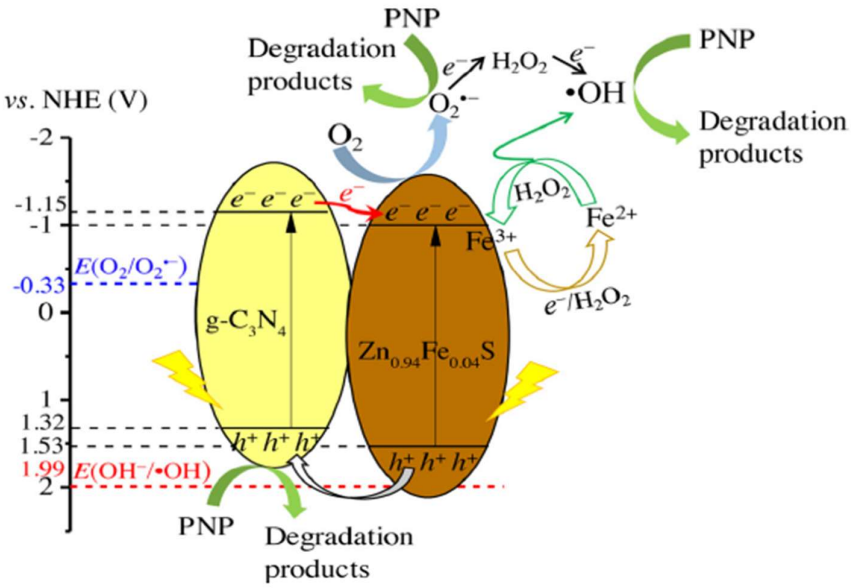

Figure 2.6: Proposed p-nitrophenol degradation mechanism using g-C_3N_4/ $Zn_{0.94}Fe_{0.04}S$ under solar irradiation (Wang et al., 2020).

Table 2.6: Studies of modification on different photocatalysts using g-C_3N_4.

Modification	Application	Light Source	Result	Reference
Sb_2MoO_6/g-C_3N_4	Rhodamine B(RhB) photodegradation and hydrogen (H_2) evolution	Visible light	7.5% Sb_2MoO_6/g-C_3N_4 exhibited a 6.6- and 5.5-times higher rate of RhB degradation and H_2 evolution compared to pure g-C_3N_4 respectively.	Zhao et al., 2020
$Ba_5Nb_4O_{15}$	H_2 evolution	Visible light	$Ba_5Nb_4O_{15}$/g-C_3N_4 achieved 2.35 times higher H_2 evolution.	Wang et al., 2019
$BiVO_4$	H_2 evolution	visible light	0.8 wt% g-C_3N_4/$BiVO_4$ achieved 2.25 times better H_2 evolution.	Samsudin et al., 2020

Table 2.6: Studies of modification on different photocatalysts using g-C_3N_4 (continued).

Modification	Application	Light Source	Result	Reference
AgBr	Methyl orange (MO) photodegradation	Visible light	Modified composites showed 1.6- and 1.3-times greater MO degradation than AgBr and g-C_3N_4 respectively.	Ghattavi and Nezamzadeh-Ejhieh, 2020
Ag	MO and 4-nitrophenol photodegradation	Visible light	Ag/g-C_3N_4 successfully removed 98.7% of MO in 2h and completely removed 4-nitrophenol in 70s	Liu et al., 2020

2.5 Silver Nanoparticles (Ag)

Silver (Ag) is a noble metal that exhibits significant advantages when used as a dopant for $BiPO_4$. Ag as a noble metal acts as an excellent electron acceptor for facilitating quick electron transfer from both exterior and inner $BiPO_4$ under light irradiation which hinders the recombination rate of electron-hole pairs. Likewise, Ag particles can generate Surface Plasmon Resonance (SPR) with $BiPO_4$ leading to disturbance in the dielectric constant of the surrounding matrix (Nainanni, Thakur and Chaskar, 2012). This enables $BiPO_4$ to absorb visible light which indirectly enhances the photocatalytic activity of $BiPO_4$ and increases the quantum yield for the photocatalysis process. Noble metal possesses superior visible light absorption attributed to SPR effect, which is defined as a collective oscillation of electrons generated at the interface of noble metal and photocatalysts. Referring to Figure 2.7, surface plasmon oscillation of metal electrons was generated by the coupling relation between incident oscillating electromagnetic field, the incoming irradiation, and noble metal nanoparticles (Bumaidad and Madkour, 2014). The metal electron density is polarized to one side and oscillates in resonance with the light frequency as lightwaves travel through the noble metal nanoparticles. The above phenomenon resulted in Localized Surface Plasmon Resonance (LSPR) (Fong and Yung, 2013). After excitation of LSPR, the surface plasmon will decay and transfer the harnessed energy to the electron located at the CB of noble metal nanoparticles, producing highly energetic electrons known as hot electrons. The excited electron will be donated to the semiconductor (Paul and Giri, 2018).

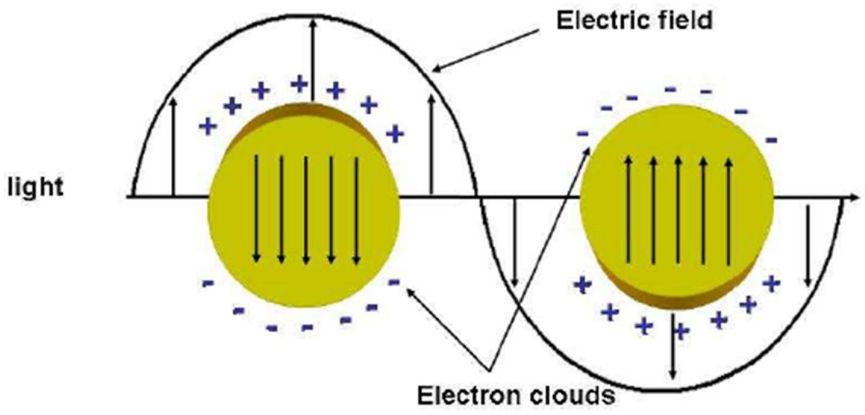

Figure 2.7: Surface plasmon resonance oscillation of metal electrons (Bumaidad and Madkour, 2014)

Numbers of research had been conducted on doping of noble metal Silver. Iliev et al. (2006) have shown that deposition of Ag on the surface of TiO_2 has significantly increased the photocatalytic degradation of oxalic acid, which is also contributed by the higher rate of oxygen reduction (Iliev et al., 2006). According to Wu et al (2009), Ag ions act as an electron-hole separation center below optimum dosage concentration, increasing photocatalytic efficiency. In contrast, Ag ions will act as electron-hole recombination center when Ag ions exceed the optimum concentration, which leads to a negative effect in photocatalytic processes (Wu et al., 2009). Thus, attracted by Ag's superior characteristic, several kinds of research had been conducted using Ag to modify different photocatalysts. Chen and Li (2020) applied a one-pot hydrothermal synthesis method to fabricate Ag/TiO_2 for the plasmonic resonance and hinder the photogenerated electron recombination rate. The 2% Ag/TiO_2 achieved 98% conversion of p-ethyl bromobenzene to p-ethyl biphenyl

in 24h under visible light irradiation (Chen and Li, 2020). Paul et al. (2020) synthesized Ag/g-C_3N_4 through thermal polymerization between two precursors. 1mmol Ag/g-C_3N_4 96% of MB photodegradation in 2h under visible light irradiation (Paul et al., 2020). Abirami et al. (2020) successfully fabricated Ag/$PbTiO_3$ composite via a simple hydrothermal method. 0.03% Ag/$PbTiO_3$ attained 92.8% MB removal in 150min under UV light irradiation (Abirami et al., 2020).

Furthermore, Dawound et al. (2020) managed to synthesize silver doped zirconium oxide (Ag/ZrO_2) using milk powder through a single-step solution combustion method. Silver (6 mol %) doped ZrO_2 attained 95% Rhodamine B removal within 105 min under visible light irradiation (Dawound et al., 2020). Silver-doped NiO was fabricated via a sol-gel method using *Cydonia oblonga* plant extract by Ghazal et al. (2020). The composites degraded 75% of RhB under UV light after 200min. In addition, Ag/NiO also exhibited an inhibitory effect on cancer cells (Ghazal et al., 2020). Figure 2.8 shows the proposed mechanism of azo dyes photodegradation using Ag decorated TiO_2. Deposition of Ag nanoparticles onto the surface of TiO_2 enhanced the photocatalytic performance of TiO_2 by acting as electron traps. After harnessing sufficient energy, photoexcited electrons bridged through the energy bandgap and produced electron-hole pairs. Because of the Fermi level difference, the photoexcited electron was transferred from CB of TiO_2 to CB of Ag nanoparticles effectively preventing the electron at CB of TiO_2 to recombine back to VB of TiO_2. Accumulation of electrons at Ag nanoparticles react with O_2 to form O_2^- radicals. For this study, Ag nanoparticles act as electron traps

that prolong the photogenerated electron's life, hindering the recombination rate of photogenerated active electrons (Sobana Muruganadham and Swaminathan, 2006). Furthermore, Wang et al. (2015) carried an experiment involving degradation of Rhodamine B (RhB) using Ag/$Na_2Ta_2O_6$ nanocomposites under visible light irradiation and the proposed mechanism is depicted in Figure 2.9. Under visible light irradiation, Ag nanoparticles generate hot-electrons via SPR effect, then the hot electrons reduce O_2 to O_2^- radicals. The photoexcited electron at Ag nanoparticles also took part in the degradation of RhB (Wang et al., 2015). Table 2.7 summarized various past studies that modified photocatalysts using silver nanoparticles. Hence, Ag is the preferable choice for this thesis, with a controlled concentration of Ag ions which enable $BiPO_4$ to absorb visible light which indirectly enhances the photocatalytic activity and increases the quantum yield for the photocatalysis process.

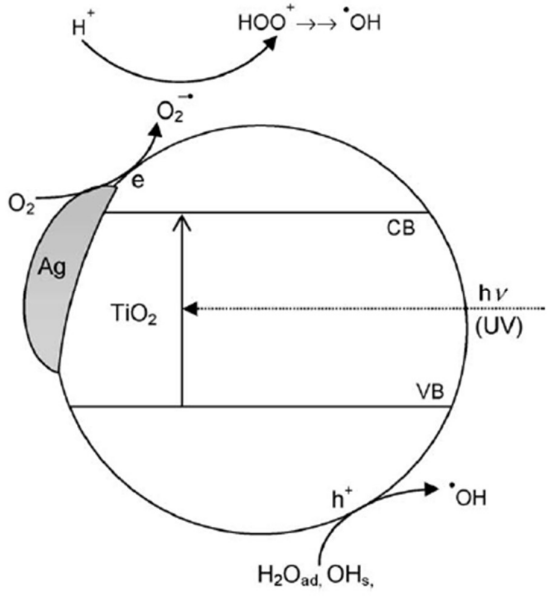

Figure 2.8: Proposed mechanism of azo dye degradation using Ag/TiO_2 (Sobana Muruganadham and Swaminathan, 2006).

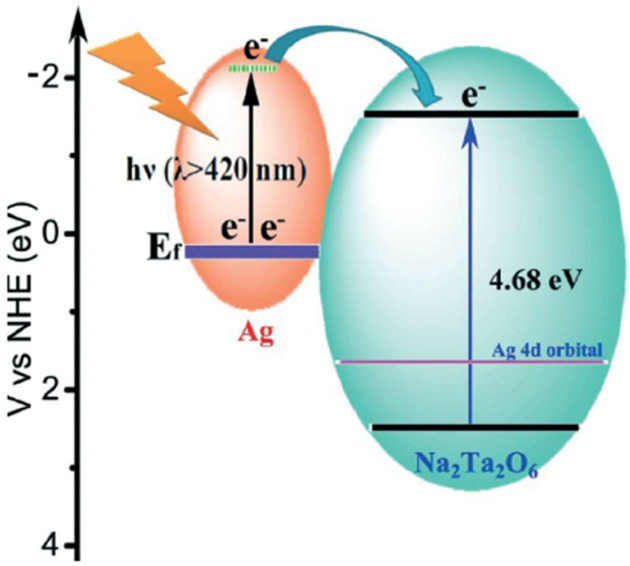

Figure 2.9: Mechanism of RhB degradation using $Ag/Na_2Ta_2O_6$ (Wang et al., 2015).

Table 2.7: Studies of modification of photocatalysts using Ag nanoparticles.

Modification	Application	Light Source	Result	Reference
TiO_2	Conversion of p-ethyl bromobenzene to p-ethyl biphenyl	Visible light	Ag/TiO_2 achieved 98% conversion of p-ethyl bromobenzene to p-ethyl biphenyl. Decoration of Ag provides visible light absorption enhancement.	Chen and Li, 2020
$g\text{-}C_3N_4$	Methyl Blue (MB) photodegradation	Visible light	$Ag/g\text{-}C_3N_4$ attained complete removal of MB in 2 h. Composite possessed efficient facilitation of charge transfer and visible light absorption.	Paul et al., 2020
$PbTiO_3$	MB photodegradation	UV light	$Ag/PbTiO_3$ achieved 92.8% MB removal and exhibited excellent reusability. Increased number of active sites on the surface of photocatalyst and presence of Ag that hinder the recombination of the electron-hole pairs.	Abirami et al., 2020

Table 2.7: Studies of modification of photocatalysts using Ag nanoparticles (continued).

Modification	Application	Light Source	Result	Reference
ZrO_2	Rhodamine B (RhB) photodegradation	Visible light	Silver doped ZrO_2 achieved 95% removal of RhB in 105min.	Dawoud et al., 2020
NiO	RhB photodegradation and inhibition of cancer cells	UV light	Ag-doped NiO attained 75% RhB removal after 200min and showed an inhibitory effect on cancer cells.	Ghazal et al., 2020

CHAPTER 3

MATERIALS AND RESEARCH METHODOLOGY

3.1 Materials

This chapter covers the materials and synthesis methods used in the research in the preparation of modified $BiPO_4$ photocatalyst composites. All the chemicals used in this research are of analytical purity and were used without further purification. It also includes the characterization methods adopted to examine the materials' physical and chemical properties. Next, it shows procedures of photocatalytic evaluation, active radical detection and stability test of the photocatalyst.

For the synthesis of photocatalysts, Bismuth (III) nitrate pentahydrate ($Bi(NO_3)_3 \bullet 5H_2O$) (≥98.0%, Sigma Aldrich, USA) and Ammonium dihydrogen phosphate ($(NH_4)H_2PO_4$) (Merck KGaA, Germany) were used as precursors. Ethyl glycol ($C_2H_6O_2$) (R & M Chemicals, UK) was used as a stabilizing medium. Absolute ethanol ($C_2H_8O_7$) (95%, Hmbg Chemicals, Germany), Nitric acid (HNO_3) (R & M Chemicals, UK) and ultrapure water were used for washing purpose. Silver nitrate ($AgNO_3$) (Merck KGaA, Germany) and urea (NH_2CONH_2) (R & M Chemicals, UK) were used as dopants. 2,4-Dichlorophenols (2,4-DCP) (Merck KGaA, Germany) was used as a synthetic pollutant.

For high-performance liquid chromatography (HPLC), Acetonitrile (ACN) (gradient grade, Merck KGaA, Germany) and ultrapure water were used as mobile phase in HPLC analysis. In scavenging test, Dimethylsulfoxide, (DMSO) (99.0%, Ajax Finechem Pty Ltd, Australia) Benzoquinone (BQ) (≥98.0%, Sigma-Aldrich, USA), Isopropyl Alcohol (IPA) (99.9%, Hmbg Chemical, Germany) and Ethylenediaminetetraacetic acid disodium (EDTA) (99.0% ChemSoln, Malaysia) were used as scavenging reagents for each radical

3.2 Synthesis of photocatalysts

3.2.1 Preparation of $BiPO_4$

$BiPO_4$ is synthesized by a simple sol-gel route. Typically, 0.031 mmol of Bi $(NO_3)_3 \cdot 5H_2O$ is diluted into 10 mL ethylene glycol in a beaker under magnetic stirring until a clear bismuth precursor solution is formed. Then, 0.04 mmol of $NH_4H_2PO_4$ was added into the above solution under magnetic stirring over 30 min. Eventually, the resulting precipitated $BiPO_4$ was collected by centrifugation and washed with deionized water and absolute ethanol and then dried at 60°C for 12 h (Zhang et al., 2018).

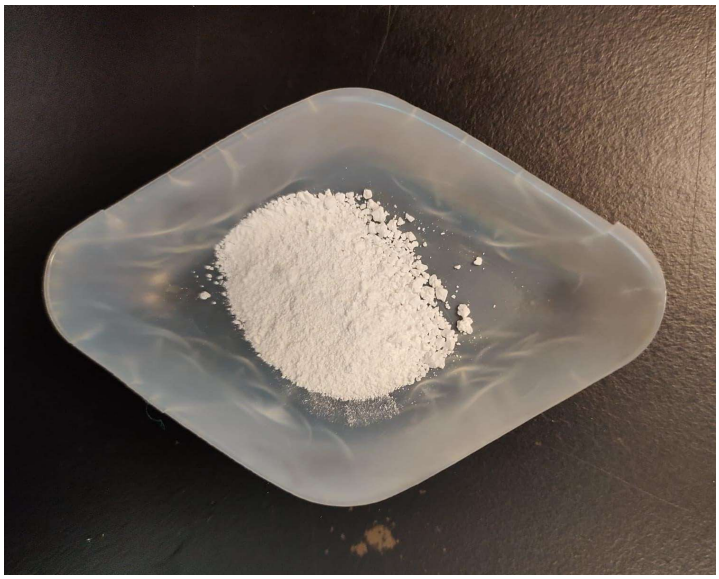

Figure 3.1: Pure $BiPO_4$

3.2.2 Preparation of g-C_3N_4

g-C_3N_4 was prepared by a thermal decomposition method using urea as the precursor. 10 g of the urea was placed in a pastry dish evenly (Zheng, Zhang, and Li, 2017). It was then dried at 80°C for 24 h in an oven. The dry urea was then placed in a crucible before it was placed in a muffle furnace and heated to 550° C for 3 h. The yellow product was washed with nitric acid and ultra-pure water repeated three times to remove any impurities (Liu et al., 2011). Then, the collected sample was dried in the oven at 80°C overnight.

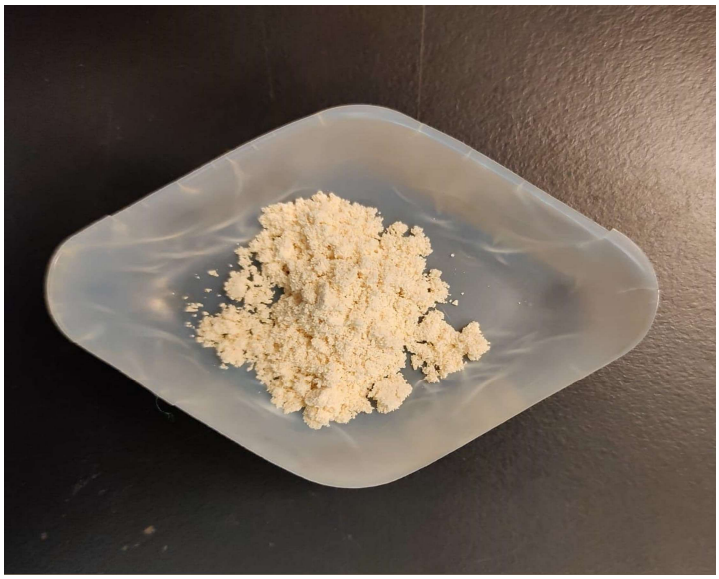

Figure 3.2: Pure g-C_3N_4

3.2.3 Preparation of $BiPO_4$/g-C_3N_4 composite

A different ratio of 0.5wt%, 1.5wt%, 2.5wt% of g-C_3N_4 were well dispersed with a sonicator for 30 mins. Next, 0.4g of $BiPO_4$ was added to the solutions and stirred for 1 h subjected to 70°C heating. The resulting suspension was then washed repeatedly with ultrapure water. The products were dried overnight at 60°C.

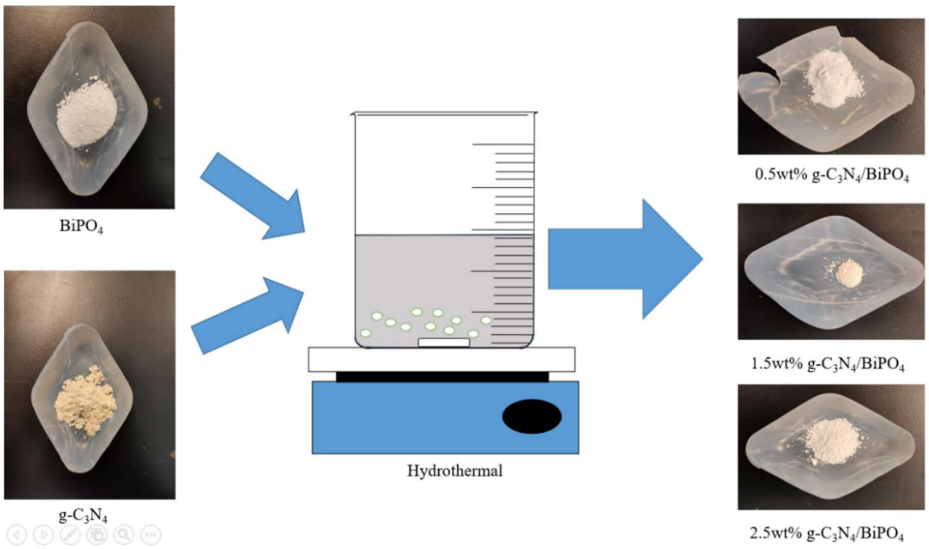

Figure 3.3: Modification of $BiPO_4$ with g-C_3N_4

3.2.4 Preparation of Ag/$BiPO_4$ composite

The synthesising Ag/$BiPO_4$ was initiated by adding 12mL of ethylene glycol with 1.0g of prepared $BiPO_4$ with a designated amount of $AgNO_3$, such as 1.0wt%, 3.0wt% and 5.0wt%, respectively to obtain the desired Ag wt% as stated. To promote sustainable photoreduction, the solution was exposed under sunlight with continuous stirring for 60min. Next, the obtained precipitate was centrifuged at 2000 rpm for 5 minutes. The produced Ag/$BiPO_4$ was then washed with ethanol and deionized water, respectively. Finally, the product was dried at 90°C overnight.

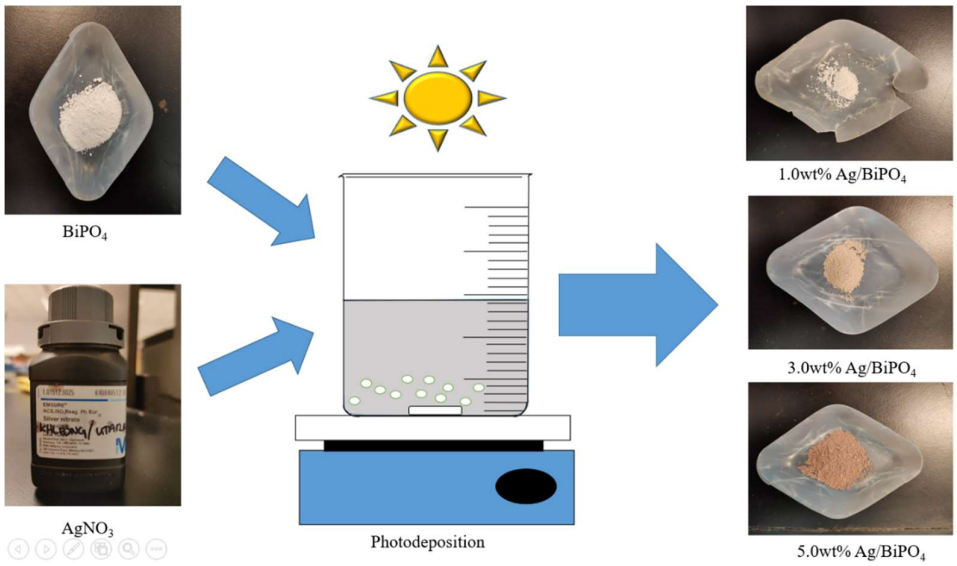

Figure 3.4: Modification of $BiPO_4$ with Ag.

3.3 Characterizations

3.3.1 Field Emission Scanning Electron Microscope (FESEM)

The morphology and composition of $BiPO_4$/g-C_3N_4 and Ag/$BiPO_4$ were characterized by field emission scanning electron microscopes (FESEM). The samples were placed on an adhesive carbon tape on an aluminum stub before coated using Jeol JFC-1600 Auto Fine Coater, then the coated samples were inserted into a Jeol JSM 7601-f field emission scanning microscope at 0.1 to 10^{-4} Pa vacuum condition.

3.3.2 Electron Dispersive X-ray (EDX)

Electron dispersive X-ray study (EDX) analysis was conducted to investigate the elemental composition of products using Joel JSM 7601-f equipment coupled with oxford Instruments X-Max energy Dispersive X-Ray

Diffractometer. The samples were also inserted into a Jeol JFC-1600 Auto Fine Coater coating and 0.1 to 10^{-4} Pa pressure condition.

3.3.3 X-ray Powder Diffraction (XRD)

Determination of the crystalline phase of the composite was done via X-ray powder diffraction (XRD) using Cu Kα(λ=1.5418Å) radiation. This analysis was carried out from 10º to 80º range at 2 º min^{-1} resolution.

3.3.4 Fourier Transform Infrared (FTIR) spectra

Fourier transform infrared (FTIR) spectra were carried out in the range of 400 to -4000cm^{-1} at 2cm^{-1} spectral resolution to determine the functional groups' presence in the composites using the Perkin Elmer Spectrum 400 Spectrophotometer. The samples were ground and added with potassium bromide (KBr) at a 1:10 ratio before compressed into a disc. The disc was fitted into a sample cell in Perkin Elmer Spectrum 400 Spectrophotometer for analysis.

3.3.5 UV-vis diffuse reflectance spectra (UV-DRS)

UV-vis diffuse reflectance spectra (UV-DRS) determine the optical diffuse reflectance spectra of the product with the $BaSO_4$ as a standard white reference. The spectrums of the products were analyzed from 200nm to 800nm using a Hach DR600 UV-vis spectrophotometer.

3.3.6 Time-Resolved Photoluminescence (TRPL)

Time-Resolved Photoluminescence (TRPL) analysis was conducted to investigate the charge carrier lifetime using Edinburgh FLS 920 with picoseconds pulsed laser under excitation wavelengths of 450 nm.

3.3.7 High-Resolution Transmission Electron Microscopy (HRTEM)

Images of high-resolution transmission electron microscopy were captured at 200kV using the FEI-TECNAI F20 Transmission Electron Microscope under the low-pressure conditions to observe the lattice fringes, particle size and distribution of the photocatalysts.

3.3.8 X-ray Photoelectron Spectroscopy (XPS)

The functional group in the compounds were investigated by X-ray photoelectron spectroscopy (XPS) using PHI Quantera II and monochromatized aluminum radiation (ALKα) in low 10^{-8} Pa vacuum pressure condition of 1487 eV.

3.4 Photocatalytic Evaluation

The photocatalytic activity of prepared photocatalysts was evaluated by the degradation of 2-4 dichlorophenol (2,4-DCP) under sunlight irradiation. 1.0 g of as-synthesized photocatalysts were added into the beakers that contained

20 ppm of 2-4DCP. The absence of catalysts will act as a control for the experiment. The dark reaction was carried out for 24 h to ensure the complete adsorption and desorption equilibrium. Next, the samples were collected at selected intervals. After the dark reaction, photodegradation under sunlight irradiation was carried out for a duration of 5 h. Samples were then taken for every 30 mins intervals. Finally, the collected samples will then be centrifuged and analyzed using High-Performance Liquid Chromatography (HPLC) Analysis. Figure 3.4.1 shows the experimental setup for photocatalytic evaluation. The concentration of 2,4-DCP solution samples was analyzed by High-Performance Liquid Chromatography (HPLC). A standard calibration curve of 2,4-DCPs was obtained before beginning the photocatalytic activity (as shown in Figure 3.4.2). The parameters of the mobile phase for HPLC analysis were tabulated in Table 3.1 below:

Table 3.1. HPLC analysis mobile phase parameters.

Pollutant	**2,4-DCP**
Column	C18 (2.1 x 50 mm, 1.7 μm)
Mobile phase	Acetonitrile: Water (80:20)
Flow rate (mL/min)	0.6
Column temperature (°C)	Room temperature
Sample temperature (°C)	Room temperature
Wavelength (nm)	270
Light	UV
Injection Volume (μL)	20

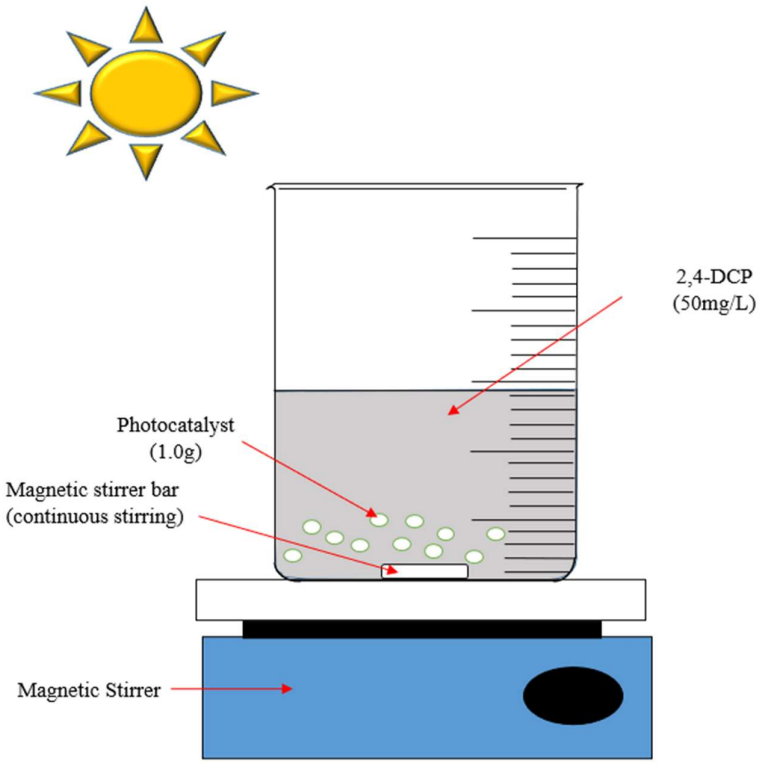

Figure 3.5: The experimental setup for photocatalytic evaluation of as-synthesized photocatalyst.

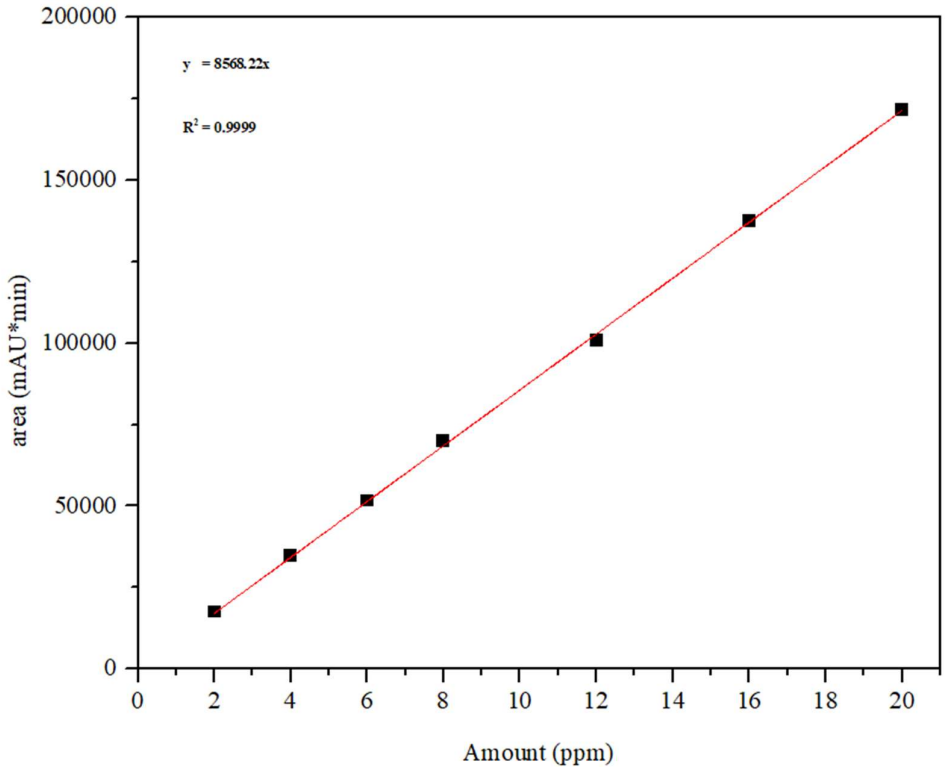

Figure 3.6: Standard calibration curve of 2,4-DCP.

3.5 Recycling Test

Recycling tests are carried out for photodegradation of 2,4-DCP to evaluate the stability of the photocatalysts. After each experiment, the photocatalyst is separated from the solution by centrifugation, washed three times with deionized water, dried at 80ºC for 12 hrs. The recycling tests are repeated 3 times and the results are analysed by HPLC.

3.6 Scavenging Test

To detect the involvement of radical species during the photodegradation of 2,4-DCP, a scavenger test is conducted. The purpose of determining the active radical species is to evaluate the photocatalytic efficiency of the photocatalyst. During the photocatalytic activity of as-prepared photocatalysts, the active radical species generated were electron, $\bullet O_2^-$, H^+ and •OH. Benzoquinone (BQ) was added as for the detection of $\bullet O_2^-$ radicals, Ethylenediamine Tetraacetic Acid Disodium salt (EDTA) can scavenge H^+ while the addition of Isopropyl Alcohol (IPA) functions as the •OH radicals (Wu et al., 2017). Each scavenger was added with an amount of 1mM concentration.

CHAPTER 4

RESULTS AND DISCUSSION

4.1 $BiPO_4$ modified with Graphitic Carbon Nitrate (g-C_3N_4)

A simple thermal deposition method was adopted to modify $BiPO_4$ using g-C_3N_4. The dopant is expected to prolong the lifetime of charge carriers and provide visible light and NIR absorption.

4.1.1 Characterization of $BiPO_4$ modified with Graphitic Carbon Nitrate

Figure 4.1 displays the images of $BiPO_4$/g-C_3N_4 (a-d) FESEM and (e-f) HRTEM. The FESEM images show the cubic structure of pure $BiPO_4$. It can be observed that pure $BiPO_4$ is in nano cubic structure, whereas pure g-C_3N_4 has a single layer nanosheet structure. It is also seen that nano cubic $BiPO_4$ particles were deposited on the surface of g-C_3N_4, forming a composite of $BiPO_4$/g-C_3N_4. In addition, FESEM images also indicate the well homogenous deposition of $BiPO_4$ onto the surface of g-C_3N_4. Figure 4.1 (e) displays the $BiPO_4$ lattice fringes spacing of 0.47nm which is consistent with the (110) plane of $BiPO_4$ (Tian et al., 2017). Furthermore, EDX analysis confirmed the presence of elemental species in the synthesized photocatalysts. Figure 4.2 illustrated the main characteristic peaks of g-C_3N_4 and $BiPO_4$ that were present in the samples which contained the elements: Bi, P, O, C, N. It can observe the element C

exhibited stronger peaks with the increase of g-C_3N_4 content. This is attributed to the successful doping between $BiPO_4$ and g-C_3N_4 that allowed element C from g-C_3N_4 to be present inside the modified composite, resulting in higher element C content and exhibiting a more significant peak. These main characteristic peaks indicated the successful doping of $BiPO_4$/g-C_3N_4 using the simple and facile synthesis method.

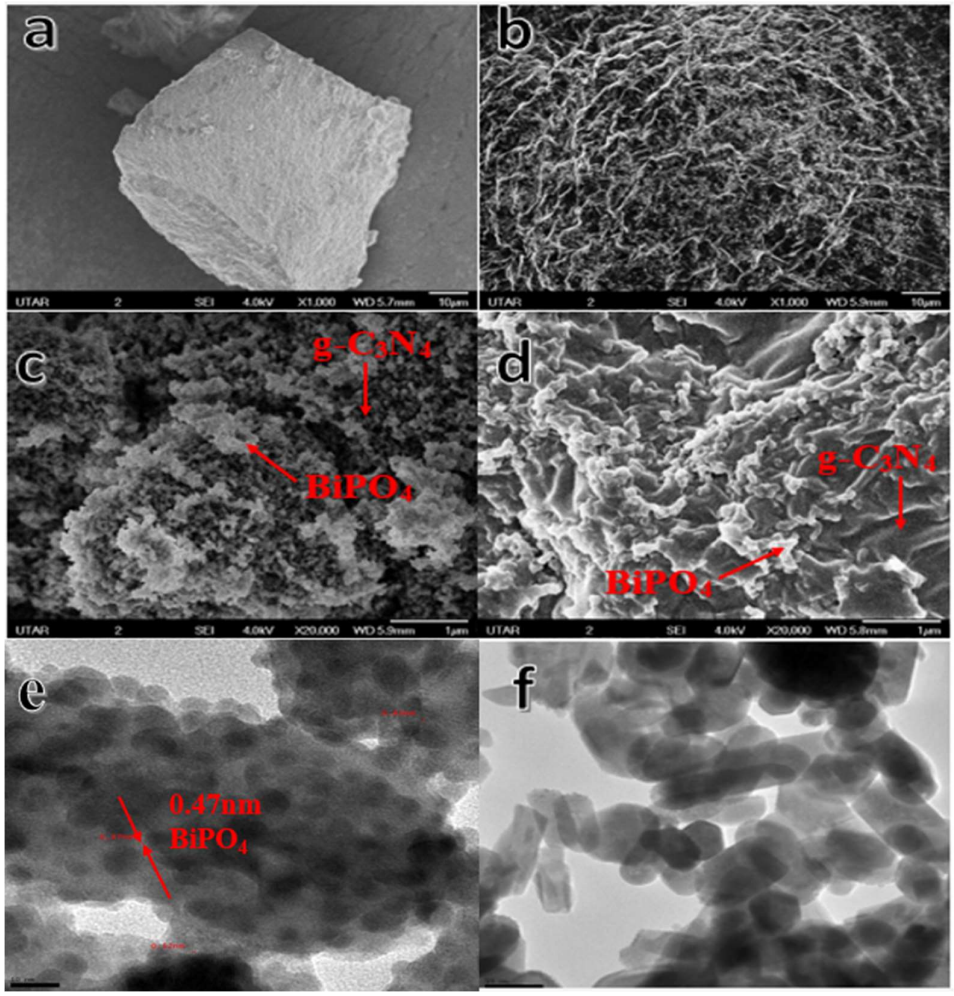

Figure 4.1: FESEM images of as-synthesized photocatalysts: (a) $BiPO_4$, (b) g-C_3N_4, (c) 0.5wt% $BiPO_4$/g-C_3N_4, (d) 2.5wt% $BiPO_4$/g-C_3N_4, (e-f) HRTEM of 2.5wt% $BiPO_4$/g-C_3N_4.

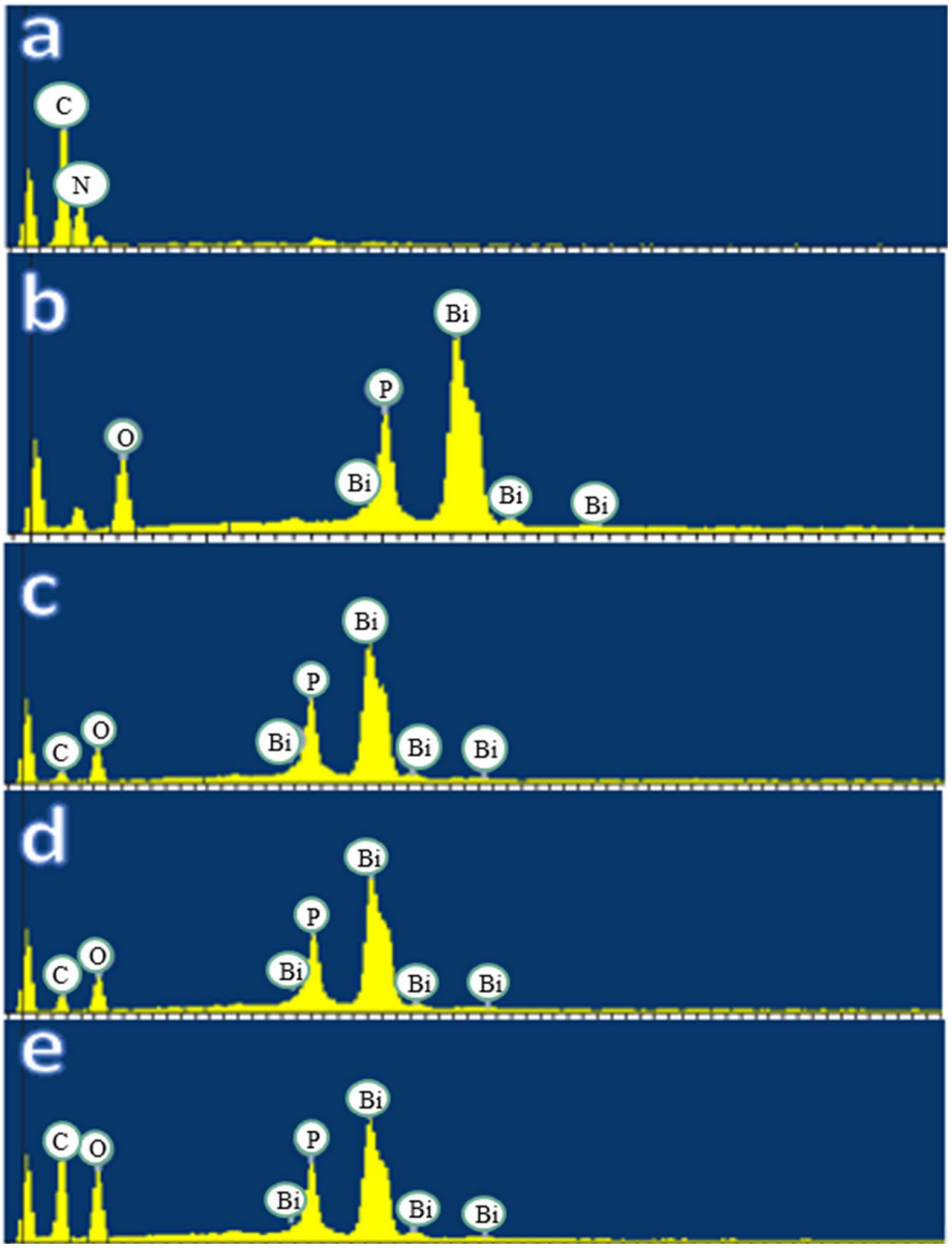

Figure 4.2: Result of EDX analysis: (a) g-C_3N_4, (b) $BiPO_4$, (c) 0.5wt% $BiPO_4$/g-C_3N_4, (d), 1.5wt% $BiPO_4$/g-C_3N_4, and (e) 2.5wt% $BiPO_4$/g-C_3N_4.

Figure 4.3 depicts the XRD spectra of pure $BiPO_4$ and various ratios of $BiPO_4$/g-C_3N_4. The pure $BiPO_4$ detected the presence of peaks at 18.1° (011), 20° (-111), 25.41° (111), 26.53° (200), 29.50° (120), 31.30° (012), 34.14° (-202), 41.85° (211) and 48.68° (212) respectively (JCPDS no.15-0767) (Zhang

et al., 2014). This inferred that the process of heating at 70°C does not change the lattice structure of $BiPO_4$ during the doping process. However, peaks for g-C_3N_4 were not detected in the composite which may be due to its low concentration of g-C_3N_4 in the composite samples (Pan and Xu, 2013).

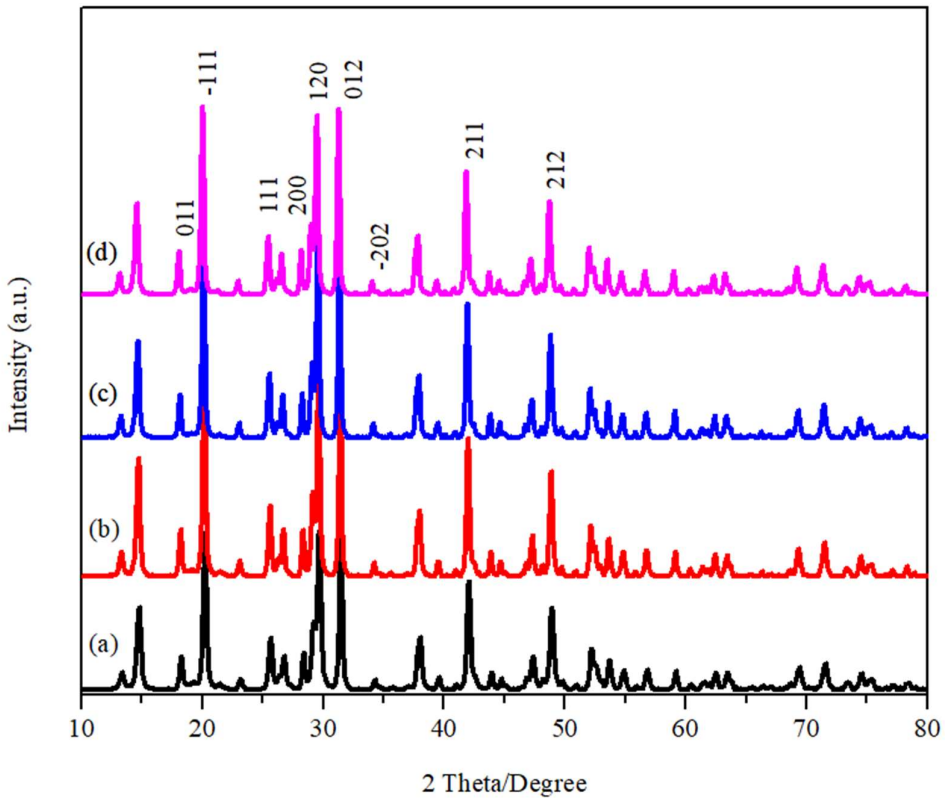

Figure 4.3: XRD pattern of (a) $BiPO_4$, (b) 0.5wt% $BiPO_4$/g-C_3N_4, (c) 1.5wt% $BiPO_4$/g-C_3N_4 (d) 2.5wt% $BiPO_4$/g-C_3N_4.

Figure 4.4 depicted the FTIR spectra for each as-prepared photocatalysts. The PO_4 group presence in $BiPO_4$ has an intense band centred at 1016 cm^{-1} due to the ν_3 stretching vibration. The band representing the presence of δ(O-P-O) and ν_4 (PO_4) were centred at 592 and 543 cm^{-1}, respectively (Romero et al., 1994). The absorption band centred at 3481 and

1615 cm^{-1} represents the ν(O-H) and δ(H-O-H) of water molecules, respectively (Liu et al., 2015). The peaks at 1237 and 1315 cm^{-1} are well correlated with the CN heterocycles stretching modes indicating the presence of g-C_3N_4 in the composite (Liao et al., 2012). In addition, the existence of all leading characteristic absorption bands of g-C_3N_4 and $BiPO_4$ in $BiPO_4$/g-C_3N_4 photocatalyst suggested no structural change of g-C_3N_4 during the doping process. The results obtained from FTIR analysis concluded that the spectra of both $BiPO_4$ and g-C_3N_4 were well detected indicating the two components were of harmonious coexistence. This result is correlated well with the FESEM and HRTEM images.

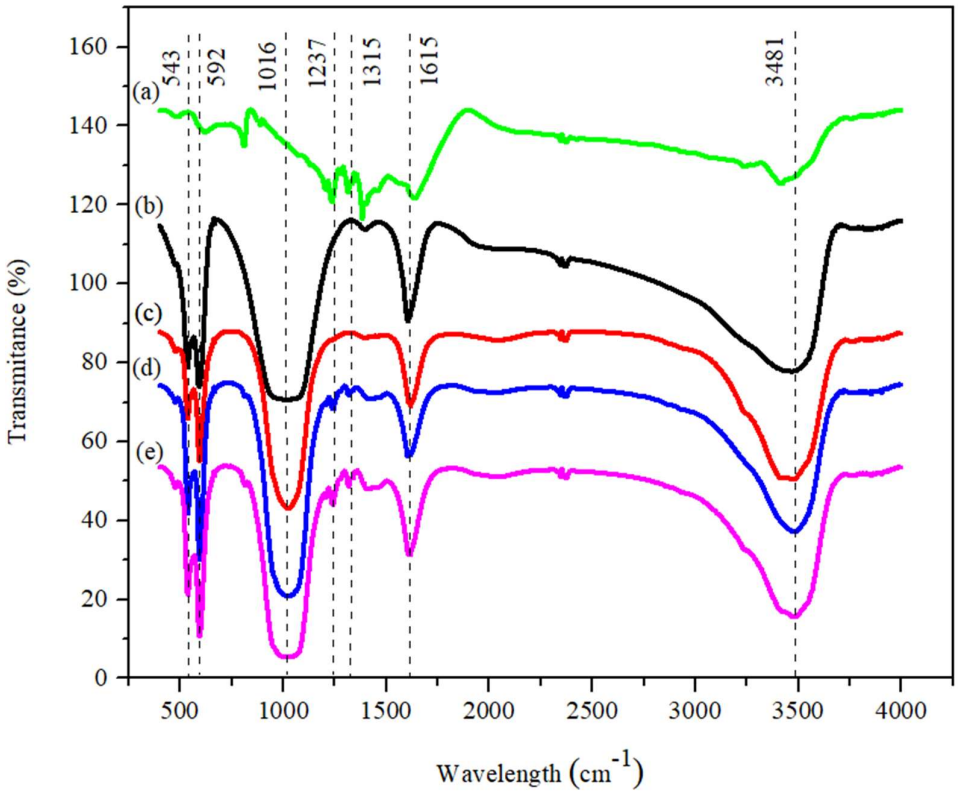

Figure 4.4: FTIR spectra of the as-synthesized photocatalysts: (a) g-C_3N_4, (b) $BiPO_4$, (c) 0.5wt% $BiPO_4$/g-C_3N_4, (d) 1.5wt% $BiPO_4$/g-C_3N_4, and (e) 2.5wt% $BiPO_4$/g-C_3N_4.

XPS analysis was conducted to investigate the elemental composition and surface composition of as-synthesized photocatalysts. The chemical elements P2p, Bi4f, O1s, C1s and N1s are shown in Figure 4.5. Two peaks of P2p displayed in Figure 4.5(b) are situated at 136.19 eV and 138.47 eV, corresponding to the doublet of P $2p_{1/2}$ and P $2p_{3/2}$, respectively (Chen et al., 2015). This depicted that phosphorus is in the pentavalent oxidation state. Bi4f element was presented in Figure 4.5(c), showing binding energy at 165.12 eV and 162.82 eV attributed to Bi $4f_{7/2}$ and Bi $4f_{5/2}$ designated the presence of Bi in trivalent oxidation state (Ran et al., 2019). For O1s element of $BiPO_4$, the binding energy at 535.79 eV and 533.38 eV portrayed in Figure 4.5(d) corresponding to the adsorbed -OH group and the adsorbed oxygen (Li et al., 2014; Zou et al., 2015; Ma et al., 2018; Liang et al., 2018). Furthermore, the binding energies of C1s are located at 289.79 eV, 288.44 eV, and 285.85 eV, where the peaks indicated the presence of graphitic carbon (C-C), C-NH_2 on the fringes of the triazine ring and sp^2 hybrid C atom bonded to a nitrogen-containing aromatic skeleton ring (N-C=N), respectively (Guo et al., 2016; Dou et al., 2018; Cui et al., 2020; Liao et al., 2020). Meanwhile, the N1s element is found to be the peaks in Figure 4.5(f) at binding energies 402.95 eV, 404.41 eV and 405.63 eV indicated the presence of sp^2 hybrid aromatic N atom (C-N=C), N-H and N-N bonding, respectively (Tan et al., 2017). The XPS analysis results further confirm the successful synthesis of $BiPO_4$/g-C_3N_4 nanocomposite.

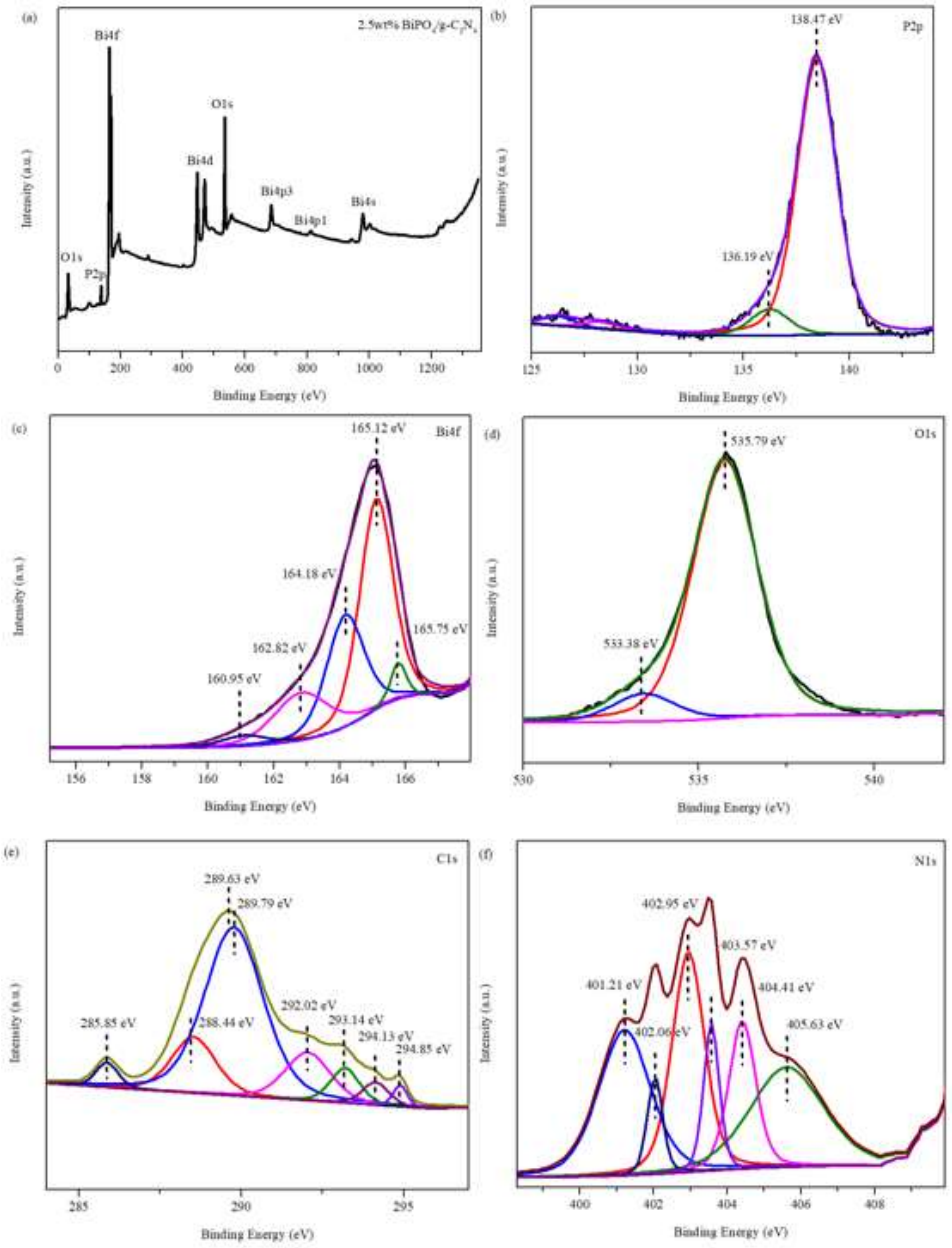

Figure 4.5: XPS spectra of the as-synthesized photocatalysts.

The UV-DRS spectra of $BiPO_4$ and modified $BiPO_4$ photocatalysts are shown in Figure 4.6. This is due to the incorporation of g-C_3N_4 that has a narrow energy bandgap (2.7eV) that allows absorption of light in the visible light range

which attributed to the promotion of visible light absorption in the solar spectrum and higher photocatalytic ability in the presence of sunlight irradiation (He et al., 2018). It can be observed that there is a slight red shift towards the visible light region due to the incorporation of g-C_3N_4 as compared to pure $BiPO_4$. This strongly indicates the enhanced light absorbance ability of $BiPO_4$ that will lead to a reduction in bandgap energy. The bandgap energy for $BiPO_4$ 0.5wt% $BiPO_4$/g-C_3N_4, 1.5wt% $BiPO_4$/g-C_3N_4, and 2.5wt% $BiPO_4$/g-C_3N_4 were 3.76, 3.65, 3.59, 3.47 eV, respectively. Referring to Figure 4.7, the incorporation of g-C_3N_4 has enhanced the light absorbance ability of $BiPO_4$ and reduces its band energy. This will lead to an enhanced photocatalytic activity attributed to the increased charge carrier's life span.

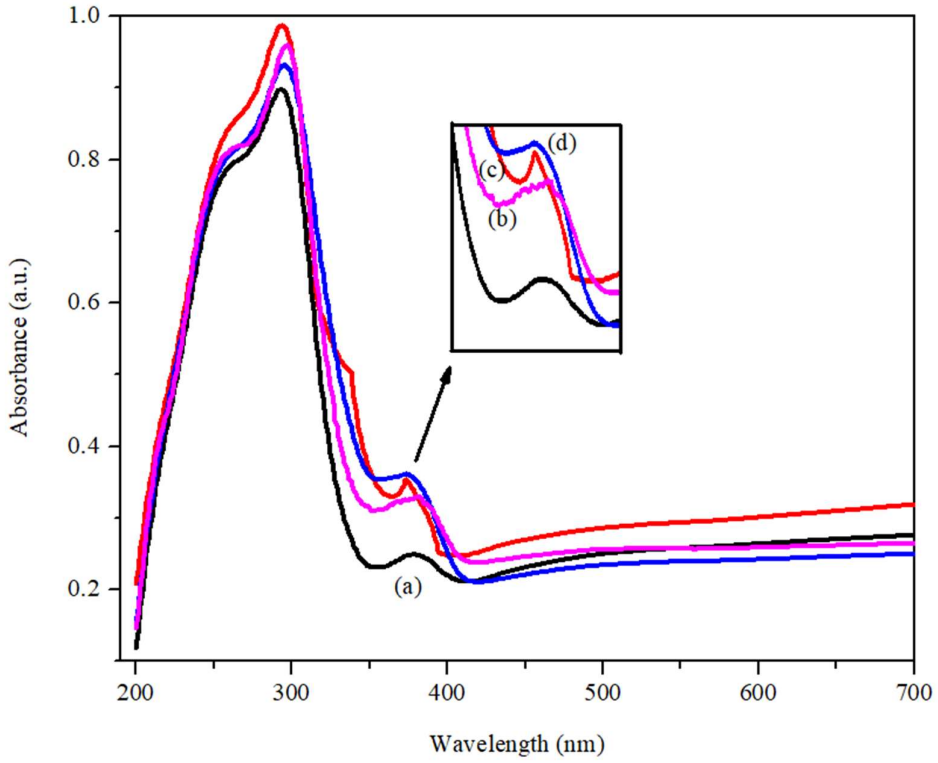

Figure 4.6: UV-DRS spectra of as-prepared (a) $BiPO_4$, (b) 2.5wt% $BiPO_4$/g-C_3N_4, (c) 0.5wt% $BiPO_4$/g-C_3N_4, and (d) 1.5wt% $BiPO_4$/g-C_3N_4.

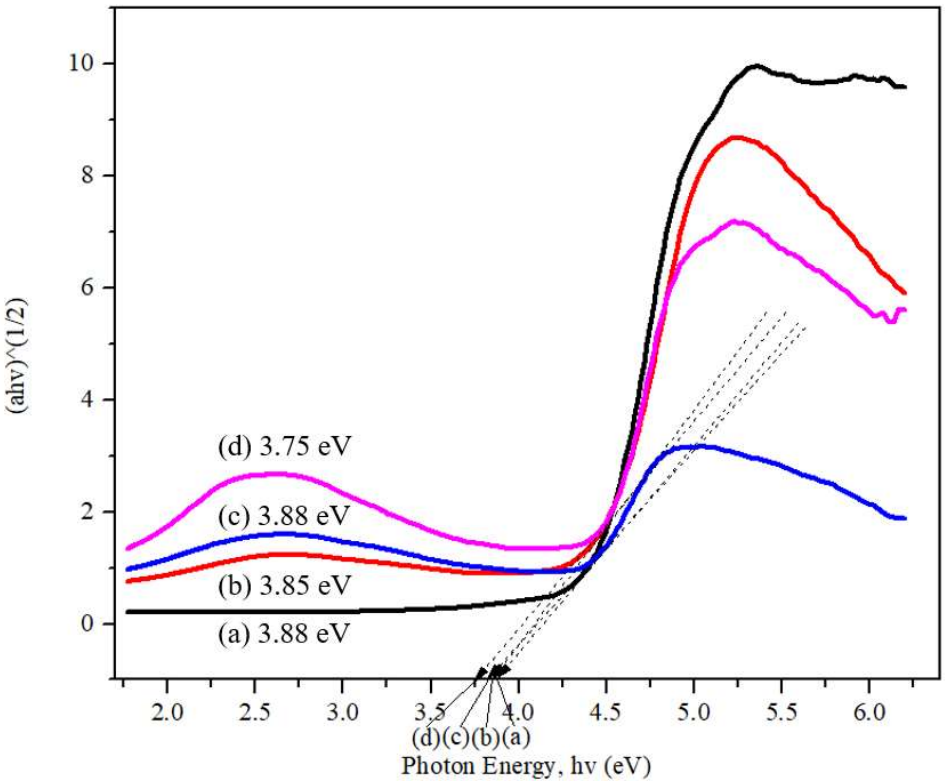

Figure 4.7: Bandgap energy of (a) $BiPO_4$, (b) 0.5wt% g-C_3N_4/$BiPO_4$, (c) 1.5wt% g-C_3N_4/$BiPO_4$, and (d) 2.5wt% g-C_3N_4/$BiPO_4$.

Figure 4.8 shows the time-resolved photoluminescence spectra of the photocatalysts. At 2.5ns to 10ns time region, it is observed that 2.5wt% $BiPO_4$/g-C_3N_4 exhibited a longer charge carrier lifetime, whereas pure $BiPO_4$ possessed the shortest charge carrier lifetime. This proves that the incorporation of g-C_3N_4 has drastically prolonged the lifespan of the charge carrier by reduces its bandgap energy. This analysis indicated that 2.5wt% $BiPO_4$/g-C_3N_4 composite samples had the best photocatalytic performance as it possessed the lowest recombination rate. It can be concluded that the photodegradation process was governed by electron-hole pairs separation. According to Figure 4.6, 1.5wt% $BiPO_4$/g-C_3N_4 shows better light absorption and produced the most

electron-hole pairs, but due to its higher recombination rate as compare to 2.5wt% $BiPO_4/g\text{-}C_3N_4$, 1.5wt% g- $BiPO_4/g\text{-}C_3N_4$ resulted in low degradation efficiency. The mechanism of improved photocatalytic performance of modified photocatalyst was built to portray the main charge transfer activities between $g\text{-}C_3N_4$ and $BiPO_4$. In the presence of light solar irradiation, the photoexcited electron will bridge through the energy bandgap of $g\text{-}C_3N_4$ forming an electron-hole pair. The photogenerated electrons at the conduction band of $g\text{-}C_3N_4$ are transferred to the conduction band of $BiPO_4$ whereas the holes generated at the valence band of $BiPO_4$ will be donated to the valence band of $g\text{-}C_3N_4$. In this situation, the separation of electron-hole pairs was enhanced. The electron at the conduction band of $BiPO_4$ will reduce the O_2 adsorbed to $\bullet O_2^-$ that will decompose the pollutants. Meanwhile, pollutants are directly oxidized by the holes at the valence band of $g\text{-}C_3N_4$. Consequently, modified $BiPO_4/g\text{-}C_3N_4$ composite exhibits better photocatalytic performance than pure $BiPO_4$.

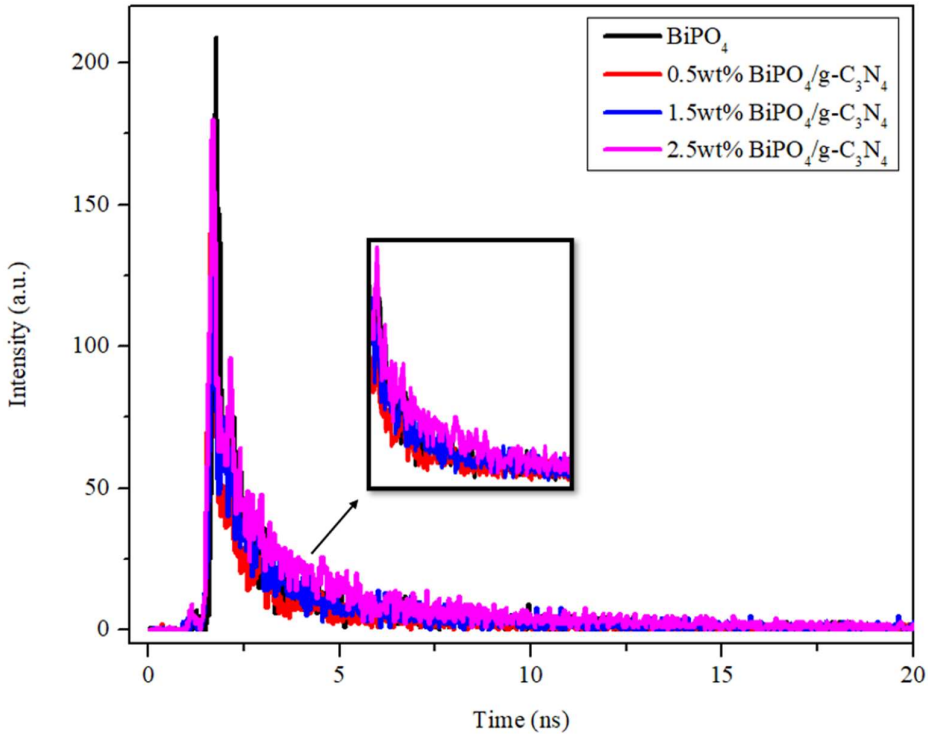

Figure 4.8: TRPL spectra of (a) $BiPO_4$, (b) 0.5wt% $BiPO_4/g\text{-}C_3N_4$, (c) 1.5wt% $BiPO_4/g\text{-}C_3N_4$, (d) 2.5wt% $BiPO_4/g\text{-}C_3N_4$.

4.1.2 Evaluation of sustainable sunlight photocatalytic performance of 2,4-DCPs by $BiPO_4/g\text{-}C_3N_4$.

The results of photodegradation experiments and control experiments of 20ppm 2,4-DCPs on as-prepared modified $BiPO_4$ and pure $BiPO_4$ under sunlight irradiation were shown in Figure 4.9. 2.5wt% $BiPO_4/g\text{-}C_3N_4$ attained complete removal in 90 mins under sunlight irradiation whereas pure $BiPO_4$ only achieved 41% degradation of 2,4-DCPs in the same duration of sunlight irradiation. This followed by 1.5wt% $BiPO_4/g\text{-}C_3N_4$ and 1.0wt% $BiPO_4/g\text{-}C_3N_4$ that achieved complete removal in 150 mins and 240 mins respectively. The enhanced performance of 2.5wt% $BiPO_4/g\text{-}C_3N_4$ is mainly contributed by the

presence of g-C_3N_4 that enhanced the charge carrier separation and vigorously generated active electrons and holes to form active radicals (Fan, Wang, and Chen, 2014). Moreover, the incorporation of g-C_3N_4 also contributed to the higher surface area of the composite that promotes adsorption sites and increased the pollutant molecules' contact that resulted in an enhanced photodegradation ability (Singh and Basu, 2020). Meanwhile, the control experiments with the absence of any photocatalysts show only a minimum (~2%) degradation of 2,4-DCPs indicating that this pollutant is a non-photosensitising nature where it is not able to degrade with the absence of photocatalysts.

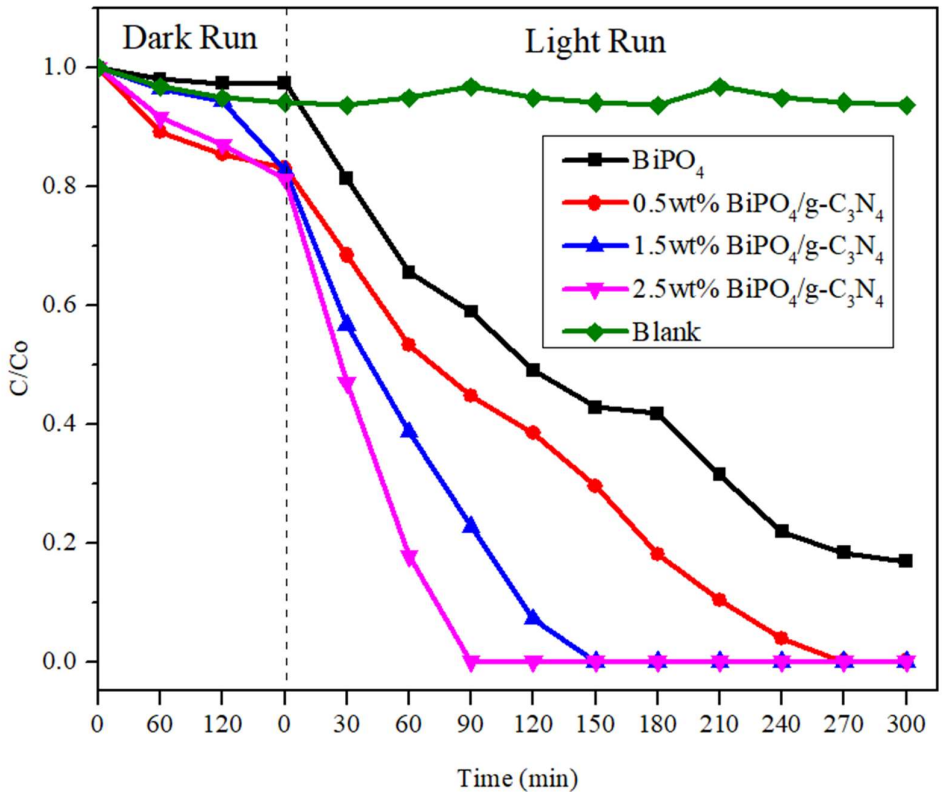

Figure 4.9: Photodegradation of 2,4-DCP using as-synthesized photocatalysts in the presence of sunlight.

The photodegradation rate of 2,4-DCPs fits well with the pseudo-first-order kinetic reaction. The following equation were applied:

$$ln\ ln\left(\frac{C}{Co}\right) = k \times t \quad (1)$$

Where k is the apparent rate constant of first-order reaction (min^{-1}), C is the pollutant concentration at a specific reaction time, Co is the initial concentration of the pollutant, t is the reaction time (Xu et al., 2012). Figure 4.10 depicts the calculated apparent rate constants of $BiPO_4$, 0.5wt% $BiPO_4$/g-C_3N_4, 1.5wt% $BiPO_4$/g-C_3N_4 and 2.5wt% $BiPO_4$/g-C_3N_4 were 0.17755, 0.25416, 0.49340 and 0.84313 h^{-1}, respectively. The rate constant of 2.5wt% $BiPO_4$/g-C_3N_4 is 4.7 times higher than pure $BiPO_4$. It can be concluded that the introduction of g-C_3N_4 promoted visible light absorption, prolonged the lifetime of charge carriers and hindered the recombination rate of photogenerated electrons as these positive effects were proved by Tauc's equation, TRPL analysis, and UV-DRS.

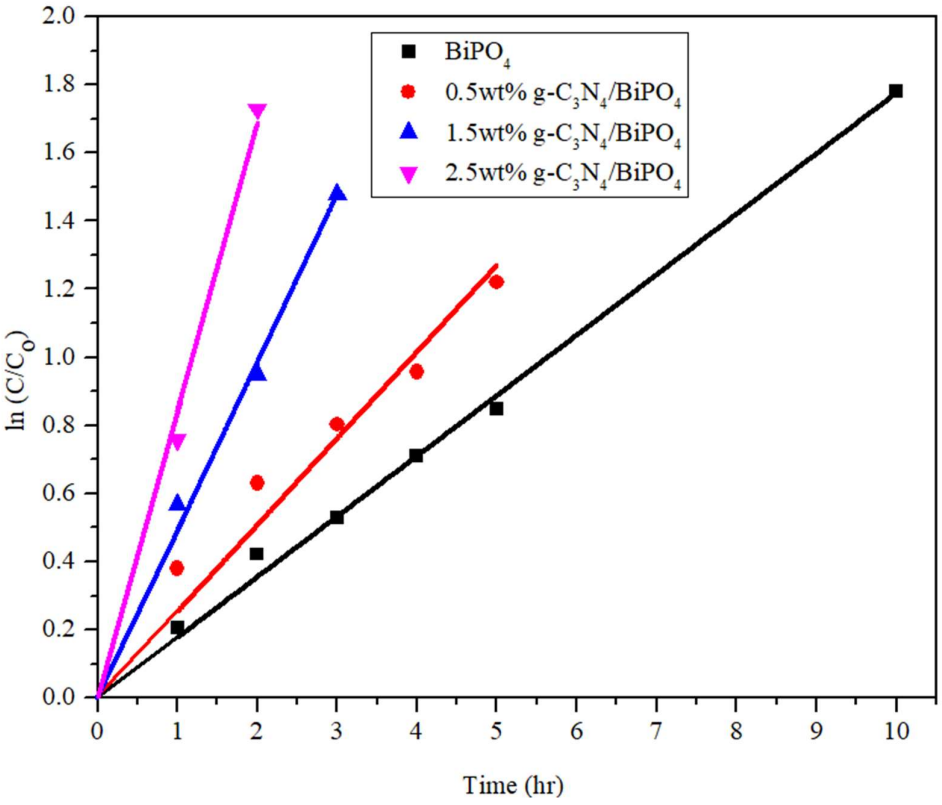

Figure 4.10: The kinetic study of 2,4-DCPs photodegradation using $BiPO_4$, 0.5wt% g-C_3N_4/$BiPO_4$, 1.5wt% g-C_3N_4/$BiPO_4$, and 2.5wt% g-C_3N_4/$BiPO_4$.

The mechanism of 2,4-DCP photodegradation is investigated through a scavenging analysis. This is to determine the active radicals by observing the effect of some radical scavengers on photodegradation. Figure 4.11 shows the scavenging analysis by using Isopropyl alcohol (IPA) as the •OH scavenger, benzoquinone (BQ) as the $•O_2$ scavenger, Ethylenediamine Tetraacetic acid disodium salt (EDTA) as the h^+ scavenger and dimethyl sulfoxide (DMSO) as electron scavenger. It is clear that photodegradation was slightly suppressed by IPA and has no significant changes in the presence of DMSO which concluded •OH and radical did not hold an essential role in the photocatalytic degradation

of 2,4-DCP. However, the photodegradation rate is heavily suppressed with the addition of EDTA and BQ. This indicates that h^+ and $\bullet O_2^-$ held the dominant role in photodegradation (Xia et al., 2017). In addition, h^+ is essential for hole oxidation that enhances the photocatalytic activity of the photocatalyst (Ilisz and Dombi, 1999). Meanwhile, $\bullet O_2^-$ plays an important role in the photodegradation of the phenolic compound as the superoxide radicals attack specifically the aromatic rings with low electronic density (Palominos et al., 2008). The presence of e- is vital for the production of superoxide radicals generated by the reaction between e- and dissolved oxygen of water (Yan et al., 2013). Figure 4.12 shows the electron mobility of the photodegradation of 2,4 DCPs. The scavenging analysis is further justified with the edge potential calculation of semiconductor at point of zero charges using Tauc's equations:

$$E_{VB} = X - E_C + 0.5E_g \quad (2)$$

$$E_{CB} = E_{VB} - E_g \quad (3)$$

Where E_C is the energy of free electrons (~4.5 eV vs NHE); E_{CB} and E_{VB} are the band edge potential for conduction band (CB) and valence band (VB); X is the electronegativity of semiconductor; Eg is the bandgap energy of semiconductor. The X values of $BiPO_4$ and g-C_3N_4 are 6.49 eV and 4.64 eV, respectively (Zhao, Wang, and Chen, 2014; Leong et al., 2015). The CB and VB edge potential of $BiPO_4$ are calculated at 0.33eV and 3.65eV, respectively and the CB and VB edge potential of g-C_3N_4 is calculated at -1.21eV and 1.49eV respectively. The unique ability of g-C_3N_4 in harvesting visible light and low bandgap energy enable it to generate active free electrons and holes when excited with sunlight irradiation (Sim et al., 2020). The free electrons will be excited from the VB to

the CB of g-C_3N_4 and then related to the CB of $BiPO_4$ as the edge potential of g-C_3N_4 (-1.21eV) was more negative than that of $BiPO_4$ (0.33eV). This excitation formation also contributed to the enhancement of electron-hole pairs separation because the free electrons are not trapped at the CB of $BiPO_4$. Meanwhile, at the VB level of g-C_3N_4 (1.49eV) which was less positive than the standard redox potential of OH^-/•OH (+1.99 eV vs. NHE) and H_2O/•OH (+2.38 eV vs NHE) leads to the holes left behind at the VB of g-C_3N_4 to directly oxidize 2,4-DCPs without reacting with H_2O to produce •OH radicals (Zhao et al., 2012; Ni et al., 2016). Moreover, the CB of $BiPO_4$ is less negative than the standard redox potential of O_2/•O_2^- (-0.33 eV vs. NHE) (Leong et al., 2015b). Consequently, O_2 adsorbed on the surface was reduced to form •O_2^- radicals that are responsible for the photodegradation of 2,4-DCPs.

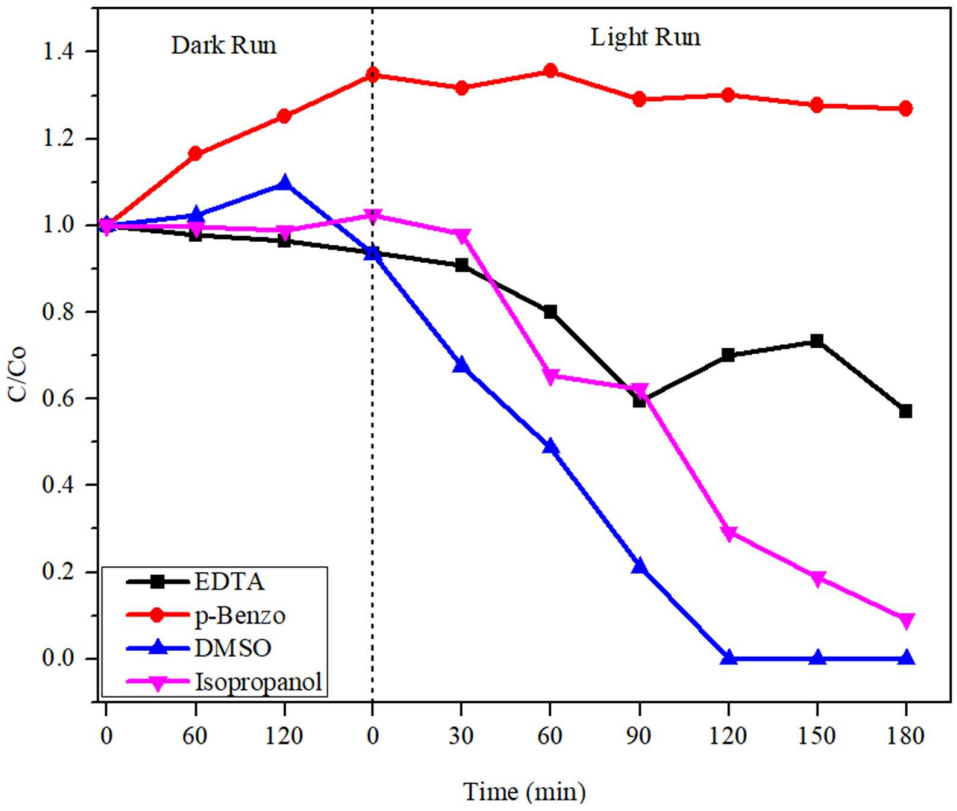

Figure 4.11: Scavenging test conducted on as-synthesized photocatalysts.

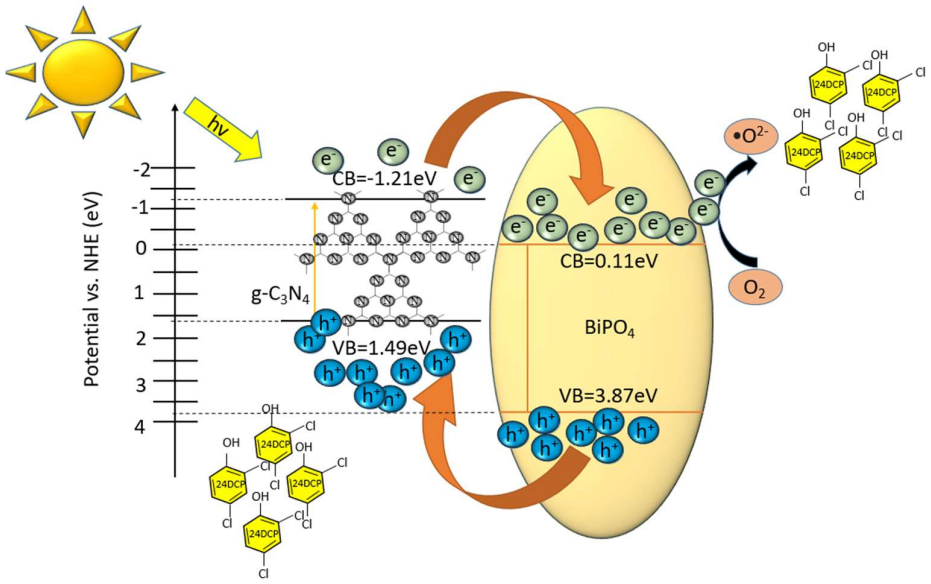

Figure 4.12: Proposed electron and hole mobility of the photodegradation of 2,4 DCPs under sunlight irradiation.

Recycle test was carried out to determine the stability and reusability of the as-synthesized samples using 2.5wt% $BiPO_4/g\text{-}C_3N_4$ that has the best photodegradation efficiency. Figure 4.13 displays the total photodegradation efficiency of the initial 2.5wt% $BiPO_4/g\text{-}C_3N_4$ together with its recycled activities. The degradation efficiency decreased from 100% to 73.22% and 76.15%. It can be observed from the Figure 4.13 4th cycle of recycling test has better result compare to 3rd cycle. This is attributed to the low light intensity on the day of 3rd cycle's experiment, the light intensity of photocatalytic evaluation was monitored and recorded using lux meter. The slight loss in photodegradation could occur due to the loss of photocatalyst during washing after centrifuging for each recycled test (Chan and Barteau, 2005). Therefore, it proved that the synthesized composites are stable materials.

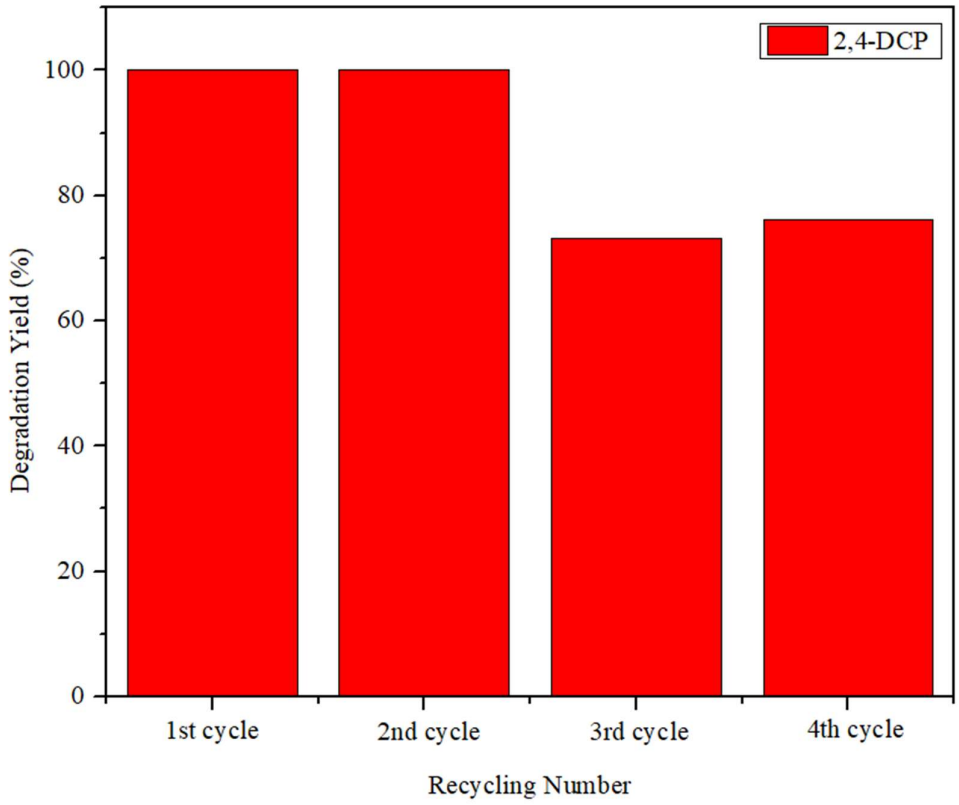

Figure 4.13: Stability test for prepared photocatalysts.

4.2 $BiPO_4$ modified with Silver Nanoparticles (Ag)

Introduction of Ag nanoparticles to $BiPO_4$ is via facile photodeposition method. The selection of silver as a dopant for $BiPO_4$ modification is due to its plasmonic characteristic that can broaden the solar spectrum absorption and the ability to facilitate electron-hole pairs efficiently.

4.2.1 Characterization of $BiPO_4$ modified with Ag Nanoparticles

The morphological and structural analysis of pure $BiPO_4$ and Ag modified $BiPO_4$ were investigated through FESEM, HRTEM and EDX. Figure 4.14(a-b) shows the FESEM images of 1.0wt% Ag/$BiPO_4$, indicating the doping of Ag on the surface of $BiPO_4$. Figure 4.14(c-e) are the HRTEM images of modified nanocomposites. It illustrated the nanocubic structure of $BiPO_4$. The presence of the dark spheres indicated the successful doping of Ag nanoparticles on the surface of $BiPO_4$. The EDX analysis further confirms the presence of element Bi, P, O, and Ag in as-prepared nanocomposite indicated the success of doping of Ag nanoparticles through the sustainable photodeposition method. The result of EDX analysis was shown in Figure 4.15.

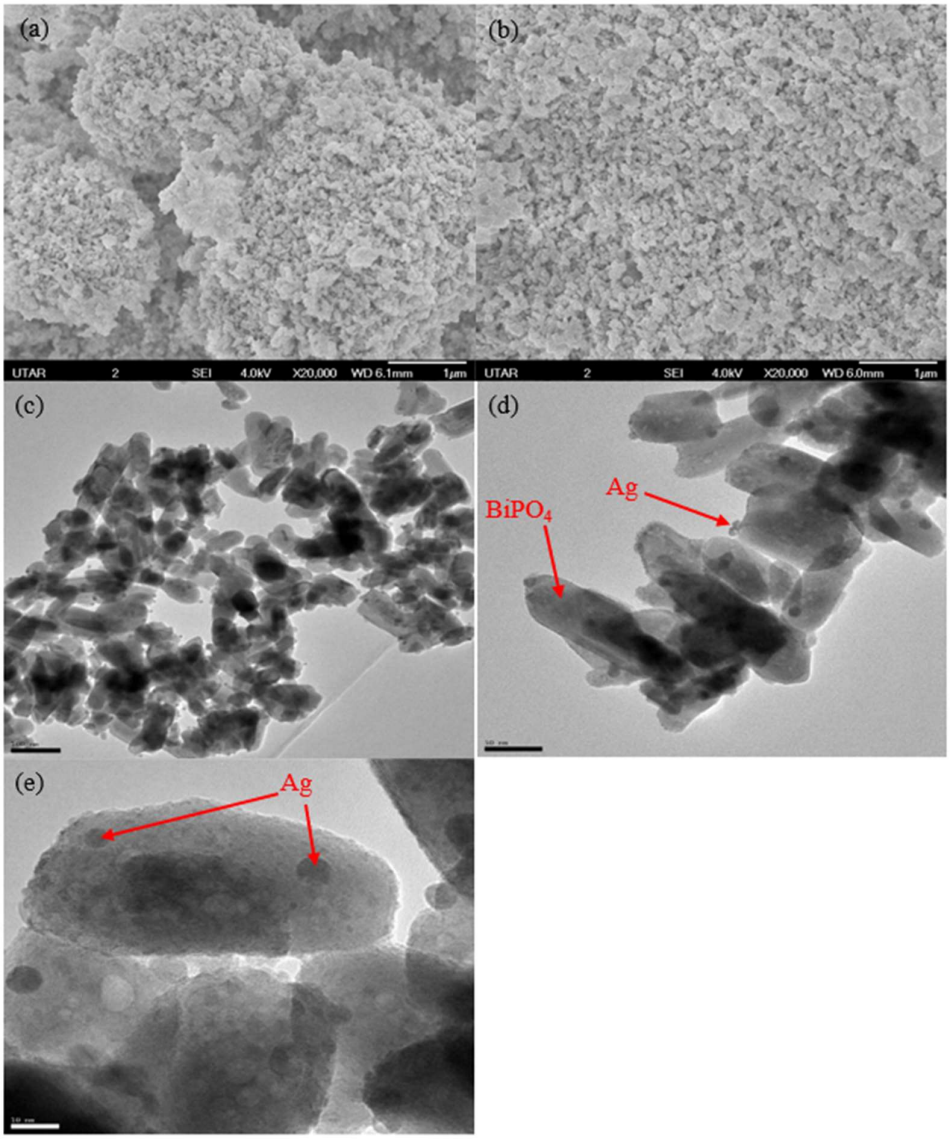

Figure 4.14: (a-b) FESEM images and (c-e) HRTEM of 1.0wt% Ag/$BiPO_4$.

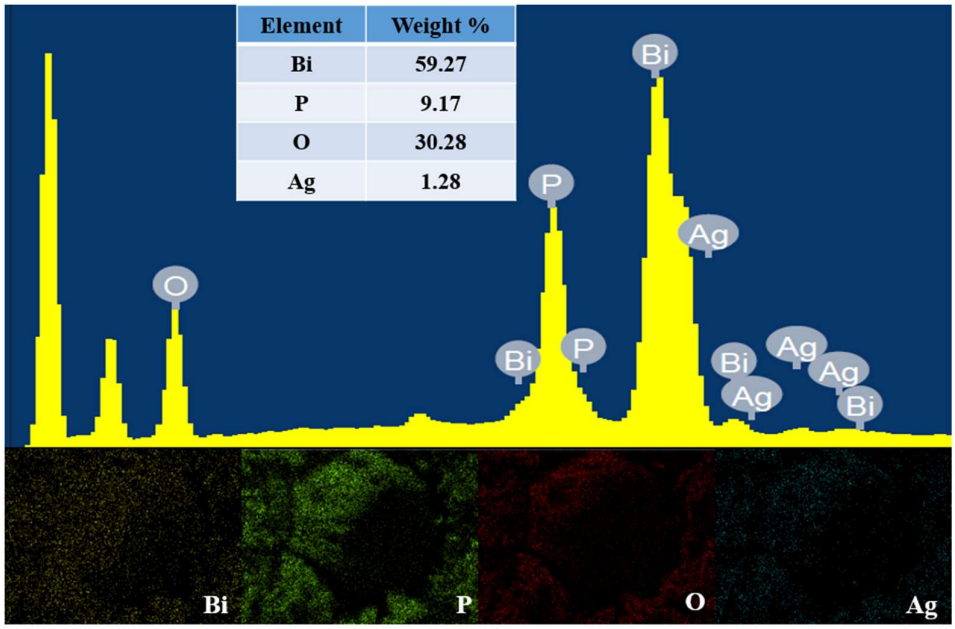

Figure 4.15: EDX analysis on 5.0wt% Ag/$BiPO_4$.

The determination of the crystalline phase of the composites was carried out via X-ray powder diffraction. Figure 4.16 depicted the XRD patterns of $BiPO_4$ and Ag/$BiPO_4$ composites with different Ag weight percentage loading (1.0wt% Ag/$BiPO_4$, 3.0wt% Ag/$BiPO_4$, 5.0wt% Ag/$BiPO_4$). Referring to Figure 4.16, the presence of peaks at 18.1° (011), 20° (-111), 25.41° (111), 26.53° (200), 29.50° (120), 31.30° (012), 34.14° (-202), 41.85° (211) and 48.68° (212) planes show the formation of $BiPO_4$. (JCPDS no.15-0767) (Zhang et al., 2014). It can be observed that there is no shift in the diffraction peak of pure $BiPO_4$ after the incorporation of Ag nanoparticles. This deduced that doping of Ag onto $BiPO_4$ with 70°C heating does not affect the lattice structure of $BiPO_4$. However, the presence of the diffraction peaks for Ag nanoparticles was not detected which might be due to the low Ag weight percentage loading.

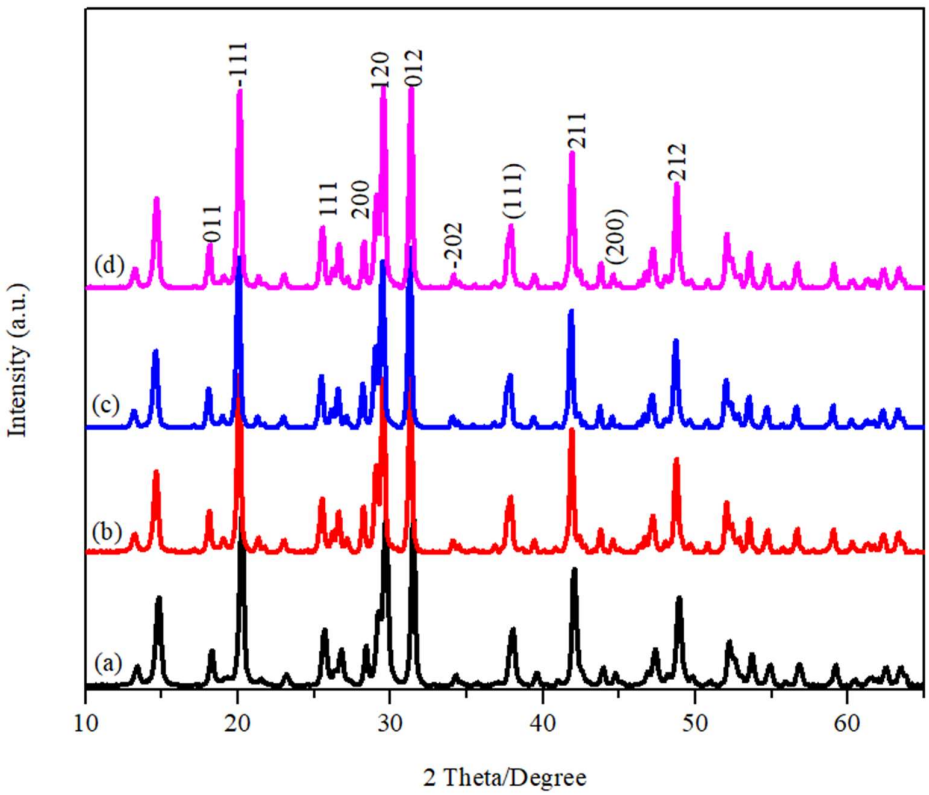

Figure 4.16: XRD diffraction pattern of (a) $BiPO_4$, (b) 1.0wt% Ag/$BiPO_4$, (c) 3.0wt% Ag/$BiPO_4$, (d) 5.0wt% Ag/$BiPO_4$.

FTIR analysis was conducted to determine the presence of the functional group in $BiPO_4$ and Ag/$BiPO_4$. Figure 4.17 shows the FTIR spectra for pure $BiPO_4$ and Ag/$BiPO_4$. The PO_4 group presence in $BiPO_4$ has an intense band centred at 1016 cm^{-1} due to the ν_3 stretching vibration. The band representing the presence of δ(O-P-O) and ν_4 (PO_4) were centred at 592 and 543 cm^{-1}, respectively (Romero et al., 1994). The absorption band centred at 3481 and 1615 cm^{-1} represents the ν(O-H) and δ(H-O-H) of water molecules, respectively (Liu et al., 2015). According to Figure 4.17, all characteristic peaks of $BiPO_4$ are the presence in Ag/$BiPO_4$ deduced that $BiPO_4$ had not suffered the loss of its character due to the introduction of Ag nanoparticles.

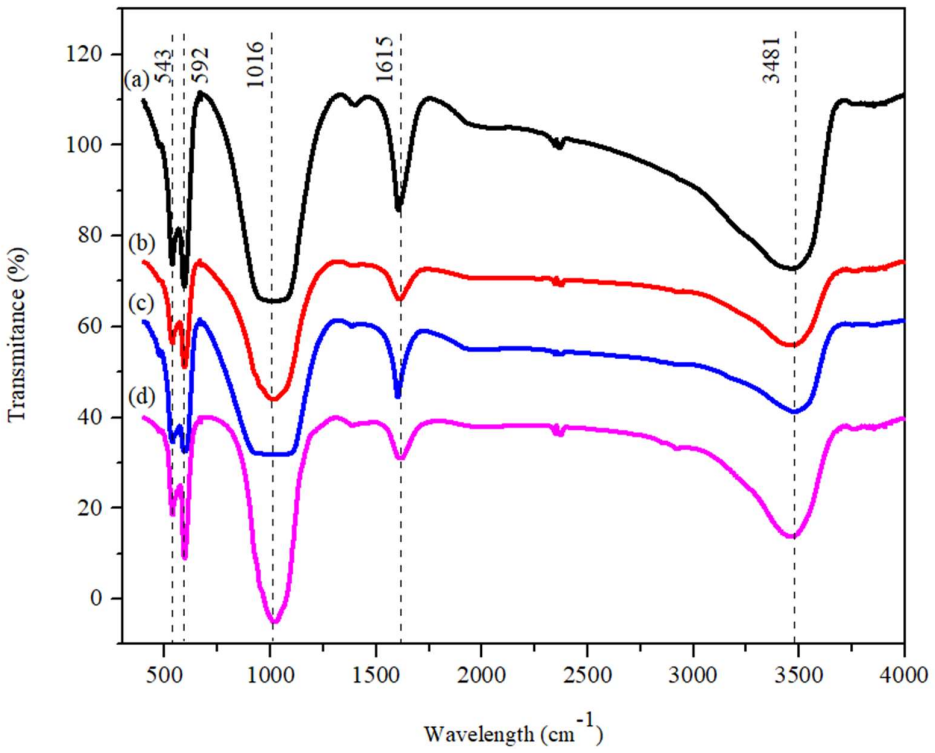

Figure 4.17: FTIR spectra for (a) $BiPO_4$, (b) 1.0wt% Ag/$BiPO_4$, (c) 3.0wt% Ag/$BiPO_4$ and (d) 5.0wt% Ag/$BiPO_4$.

XPS analysis was carried out to determine further the elemental composition and surface composition of as-prepared photocatalysts. The chemical elements P2p, Bi4f, O1s, and Ag3d are shown in Figure 4.18. Two peaks of P2p shown in Figure 4.18(b) are situated at 136.19 eV and 138.47 eV, corresponding to the doublet of P $2p_{1/2}$ and P $2p_{3/2}$, respectively (Chen et al., 2015). This indicates that phosphorus is in the pentavalent oxidation state. Meanwhile, the Bi4f element was revealed in Figure 4.18(c) with binding energy located at 165.12 eV and 162.82 eV, attributed to Bi $4f_{7/2}$ and Bi $4f_{5/2}$ confirming the presence of Bi in trivalent oxidation state (Ran et al., 2019). Furthermore, the binding energy of O1s element is discovered at 535.79 eV and 533.38 eV displayed in Figure 4.18(d) corresponding to the adsorbed -OH group

and the adsorbed oxygen (Li et al., 2014; Zou et al., 2015; Ma et al., 2018; Liang et al., 2018). Figure 4.18(e) illustrated the peaks for Ag3d. The peaks are located at 378.47 eV and 372.45 eV corresponding to Ag $3d_{5/2}$ and Ag $3d_{3/2}$, respectively. Ag 3d region has a well-separated spin-orbit component with the difference of an estimated 6.0 eV between Ag $3d_{5/2}$ and Ag $3d_{3/2}$, indicating the existence of zerovalent Ag (Zhang et al., 2013). The XPS results proved that Ag nanoparticles were successfully deposited on the $BiPO_4$.

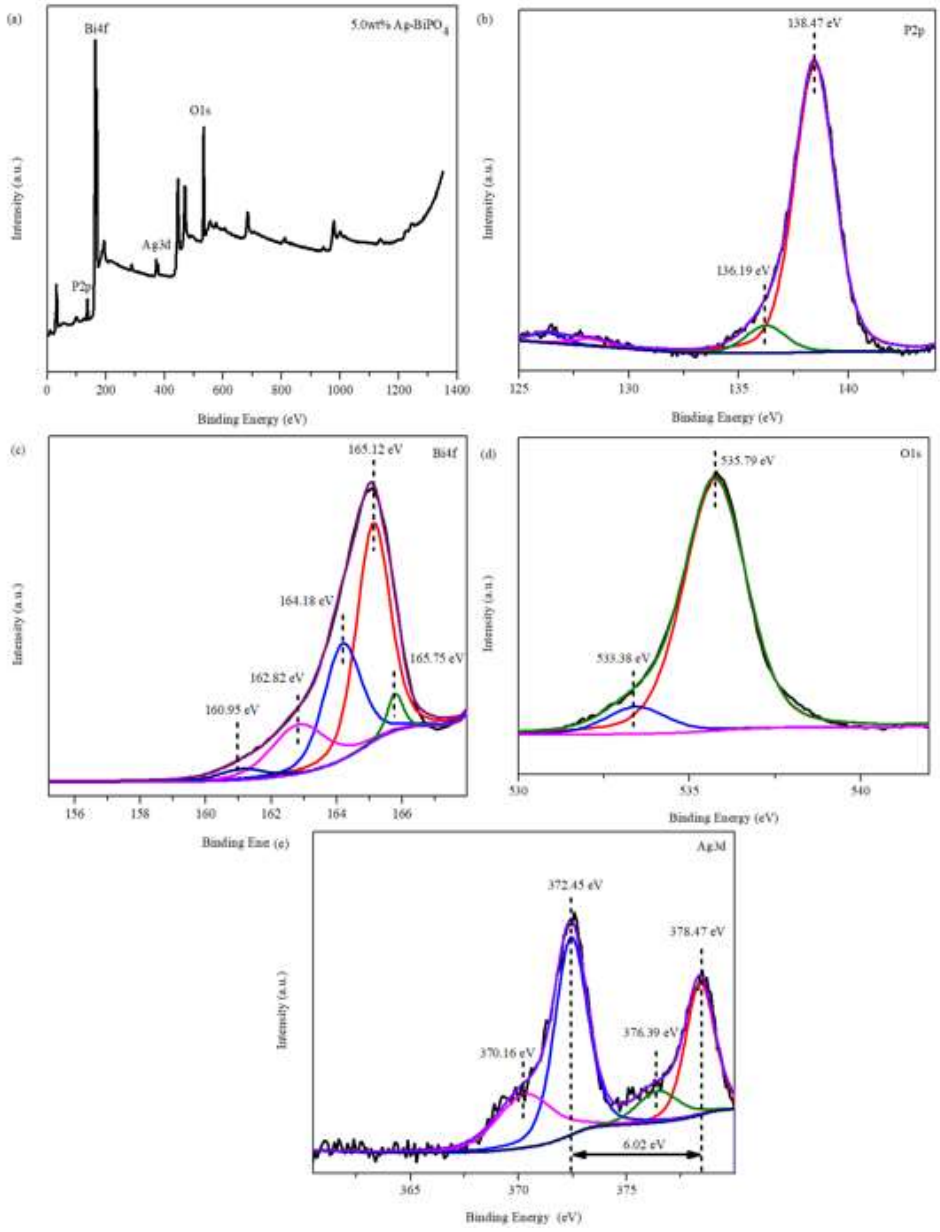

Figure 4.18: XPS spectra for 5.0wt% Ag-$BiPO_4$.

UV-DRS spectra of $BiPO_4$ and different weight percentages of Ag/$BiPO_4$ nanocomposites are displayed in Figure 4.19. Strong absorbance can be observed in the region 400-600nm. This is contributed by the superior SPR characteristic of Ag nanoparticles that enhance the light absorbance, especially

under the visible light region. When Ag nanoparticles are irradiated by solar light, it will harness energy from the visible light region and trigger the occurrence of surface plasmon oscillation of metal electrons. The metal electron density will be polarized to one side and oscillates in resonance with the light frequency resulting in the generation of localized surface plasmon resonance (LSPR). Electrons from CB of Ag nanoparticles will accumulate energy from the decay of LSPR producing highly energetic hot electrons which will be donated to $BiPO_4$, contributing to enhanced electron-hole pairs generation. The above condition resulted in an increment of quantum yield leading to photocatalytic processes (Bumaidad and Madkour, 2014; Fong and Yung, 2013; Paul and Giri, 2018). In addition, the difference in Fermi level caused the transfer of electrons to favor Ag nanoparticles, which make Ag an electron trapping center. This prevents early recombination of photogenerated electrons at the CB of $BiPO_4$ with the hole in VB of $BiPO_4$. The transferring of electrons contributes to high electron-hole pairs separation efficiency, prolonging the charge carrier lifetime, improving the photodegradation of pollutants. Furthermore, the presence of Ag nanoparticles on the surface of $BiPO_4$ can be confirmed as higher Ag loading resulted in better light absorbance at 400-600 nm. Thus, it narrows its bandgap energy of $BiPO_4$. Figure 4.20 depicted the bandgap energies of $BiPO_4$ and the different weight percentages of Ag/$BiPO_4$ calculated using Tauc's Equation (Ye et al., 2017). The estimated bandgap energy of $BiPO_4$, 1.0wt% Ag/$BiPO_4$, 3.0wt% Ag/$BiPO_4$, and 5.0wt% Ag/$BiPO_4$ are 3.88 eV, 3.85 eV, 3.82 eV and 3.75 eV, respectively. Hence, doping of Ag nanoparticles provides LSPR effect and enhance generation of active radicals that yield better photocatalytic performance (Huang, Wu and Lin, 2017).

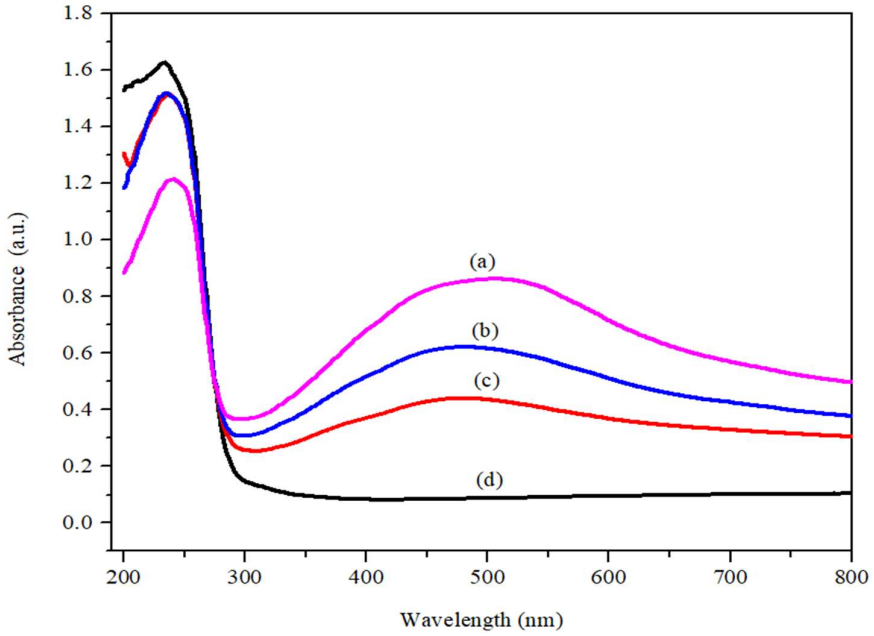

Figure 4.19: Uv-vis absorption spectra of (a) 5.0wt% Ag/$BiPO_4$, (b) 3.0wt% Ag/$BiPO_4$, (c) 1.0wt% Ag/$BiPO_4$ and (d) $BiPO_4$.

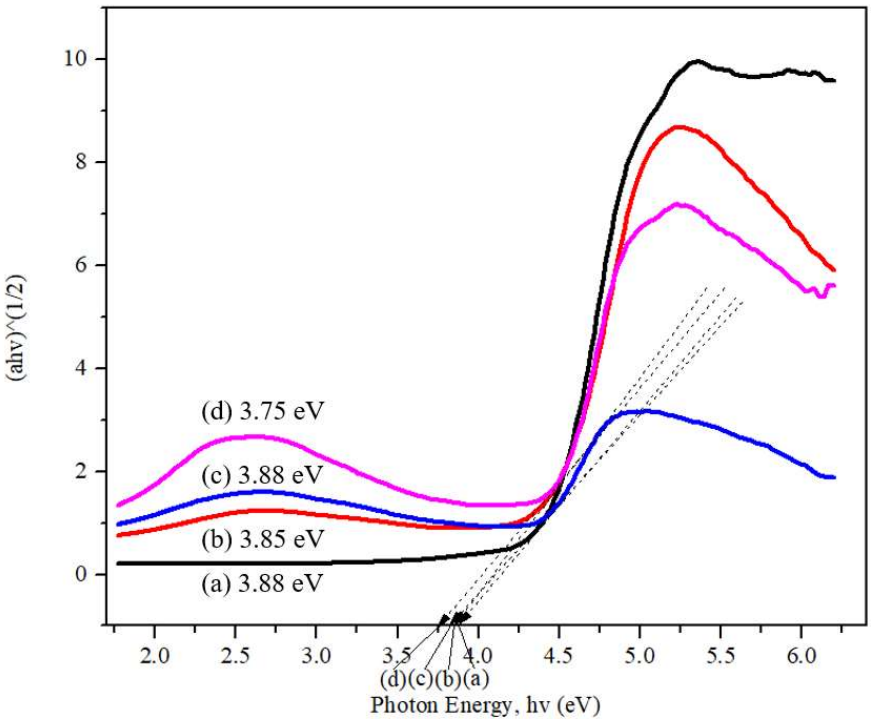

Figure 4.20: Energy bandgap of (a) $BiPO_4$, (b) 1.0wt% Ag/$BiPO_4$, (c) 3.0wt% Ag/$BiPO_4$ and (d) 5.0wt% Ag/$BiPO_4$.

TRPL analysis was carried out to study the charge carrier lifetime of $BiPO_4$ and Ag/$BiPO_4$. Figure 4.21 indicated that $BiPO_4$ exhibited the shortest charge carrier lifetime, whereas 5.0wt% Ag/$BiPO_4$ possessed the highest charge carrier lifetime. The prolonged lifespan of the charge carrier is due to the incorporation of plasmonic noble metal, Ag. The LSPR effect of Ag nanoparticles enhances the absorbance of visible light which allow higher generation of electron-hole pair for better photodegradation of pollutants (Wu et al., 2017). Apart from that, the heterostructure interface between Ag nanoparticles and $BiPO_4$ hinders the recombination rate of electron-hole pairs. Ag nanoparticles on the surface of $BiPO_4$ act as electron trapping centers, which hinder the recombination with the generated holes at the surface of $BiPO_4$ that resulted in a higher yield of generated free radicals. The generated free radicals will then be responsible for the degradation of 2,4-DCPs under the sunlight activation. (Liu et al., 2011). Thus, doping of Ag nanoparticles onto $BiPO_4$ allows better visible light absorption and hinders the recombination of electrons and holes.

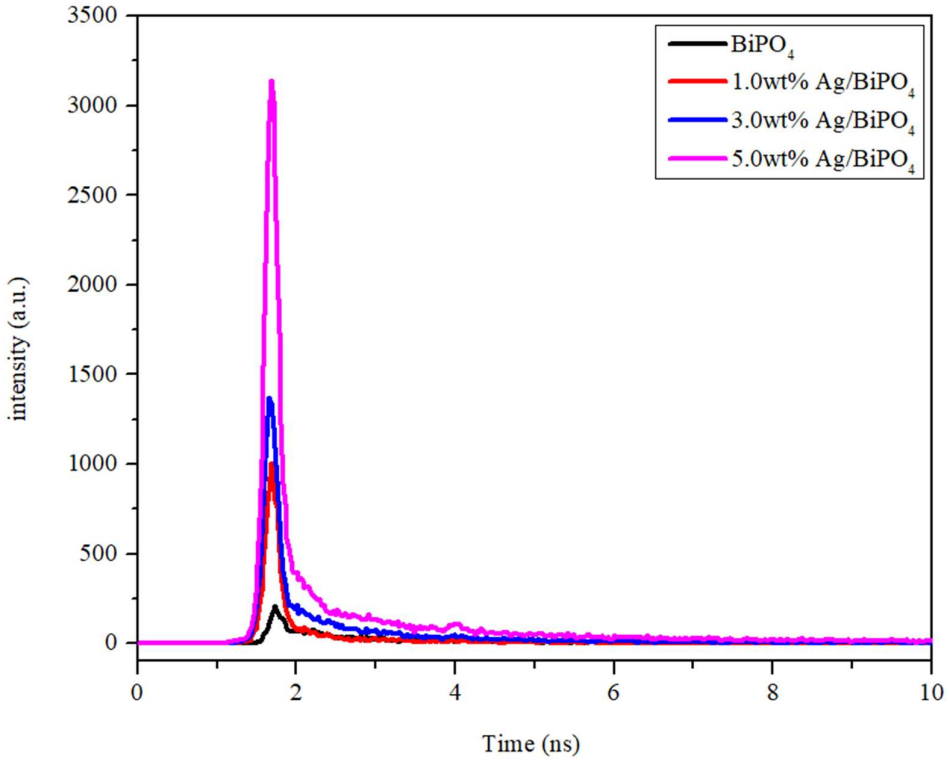

Figure 4.21: TRPL spectra of pure $BiPO_4$, 1.0wt% Ag/$BiPO_4$, 3.0wt% Ag/$BiPO_4$, and 5.0wt% Ag/$BiPO_4$.

4.2.2 Evaluation of sustainable sunlight photocatalytic performance of different weight percentages of Ag/$BiPO_4$ on the degradation of 2.4-DCPs.

The degradation of 2,4-DCPs in the presence of sunlight irradiation was conducted to study the photocatalytic degradation efficiency of modified $BiPO_4$ with Ag nanoparticles. Figure 4.22 displayed the photodegradation result of $BiPO_4$, 1.0wt% Ag/$BiPO_4$, 3.0wt% Ag/$BiPO_4$, and 5.0wt% Ag/$BiPO_4$. The dark reaction was carried for 24 h to attain a complete adsorption-desorption equilibrium. According to Figure 4.20, Ag/$BiPO_4$ possessed better photodegradation ability as compare to pure $BiPO_4$ which is due to the presence

of Ag nanoparticles that enhanced the visible light absorbance and retarded the recombination of the electron-hole pairs. In addition, the almost negligible degradation for blank indicated that 2,4-DCPs is a non-photosensitising pollutant and the presence of as-prepared photocatalysts fully carried out the photodegradation. The efficiency of 2,4-DCPs photodegradation of the experiment was in the following sequence: 5.0wt% Ag/$BiPO_4$ > 3.0wt% Ag/$BiPO_4$, > 1.0wt% Ag/$BiPO_4$ > $BiPO_4$. 5.0wt% Ag/$BiPO_4$ achieved 76.17% photodegradation efficiency which is 1.3 times high than the photodegradation efficiency of $BiPO_4$. This photocatalytic evaluation further confirms the importance of Ag doping that provides visible light absorption which enhances the photocatalytic performance of $BiPO_4$.

According to the photocatalytic degradation of 2,4-DCPs, Ag/$BiPO_4$ showed promising results that correlated well with the characterization analysis findings. Doping of Ag nanoparticles onto $BiPO_4$ allows a better absorbance of visible light in accordance with UV-DRS. This enhancement allows $BiPO_4$ to generate a higher amount of electron-hole pairs that enable better degradation of pollutants due to the massive production of free radicals. Furthermore, the generated electrons from $BiPO_4$ are then further trapped by the presence of Ag nanoparticles due to the formation of the Schottky junction between the Ag nanoparticle and $BiPO_4$ surface. In addition, the result of 5.0wt% Ag/$BiPO_4$ having the best photodegradation efficacy in comparison with other dopant loading and pure $BiPO_4$ is pursuant to TRPL characterization results as 5.0wt% Ag/$BiPO_4$ possessed the highest charge carrier lifetime leading to a high yield of free radicals formation. Hence, the incorporation of Ag nanoparticles is

favourable to the overall photocatalytic performance by broadening solar spectrum absorbance and facilitating efficient charge separation (Felukar et al., 2014; Zhang et al., 2013; Huang, Wu, and Lin et al., 2017).

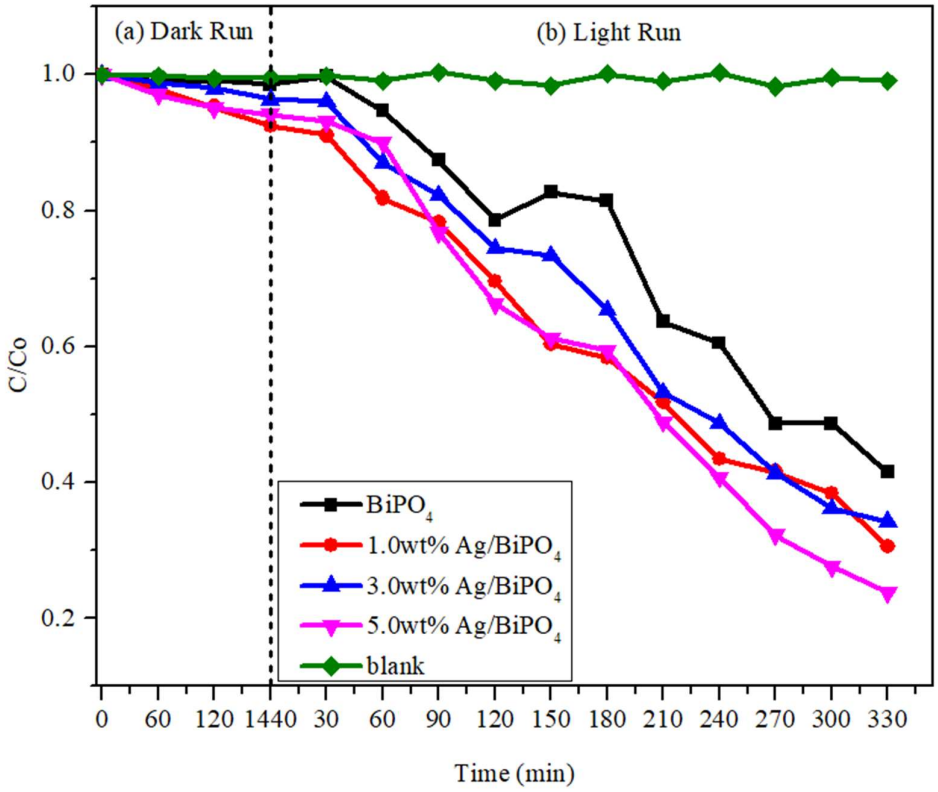

Figure 4.22: (a) Dark absorption and (b) Photodegradation of 2,4-DCP using $BiPO_4$, 1.0wt% Ag/$BiPO_4$, 3.0wt% Ag/$BiPO_4$, and 5.0wt% Ag/$BiPO_4$.

A kinetic study was conducted in order to have a better insight into the photocatalytic efficiency of Ag/$BiPO_4$, the photodegradation rate of 2,4-DCPs matched well with pseudo-first-order kinetic reaction. Figure 4.23 displays the rate constants for 2,4-DCPs degradation by $BiPO_4$, 1.0wt% Ag/$BiPO_4$, 3.0wt% Ag/$BiPO_4$, and 5.0wt% Ag/$BiPO_4$ were estimated to be 0.14549, 0.18759, 0.17354 and 0.23379 h^{-1}, respectively. It can be observed that the rate constant

for 5.0wt% Ag/$BiPO_4$ nanocomposite was approximately 1.6 times that $BiPO_4$. The result of the kinetic study is in accordance with TRPL result, UV-DRS and Tauc's equation, which further confirm doping of Ag nanoparticles enables the broadening of the visible light absorption spectrum, efficient electron-hole pairs separation and narrowing of energy bandgap.

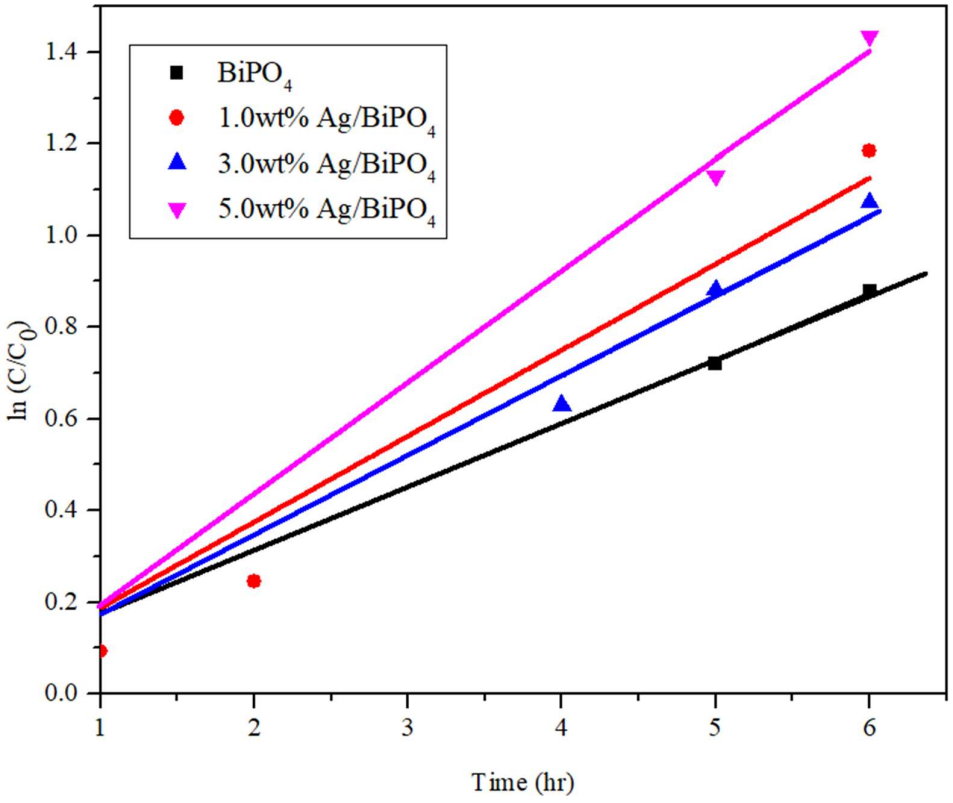

Figure 4.23: Kinetic studies of 2,4-DCPs photodegradation with $BiPO_4$, 1.0wt %Ag/$BiPO_4$, 3.0wt %Ag/$BiPO_4$, and 5.0wt %Ag/$BiPO_4$.

The mechanism of 2,4-DCPs photodegradation by Ag/$BiPO_4$, was studied through the scavenging test to determine the active radicals by observing the effect of different radical scavengers. The scavenging reagents that were used to inhibit electron (e), hydroxyl radicals (•OH), holes (h^+) and superoxide

anion radicals ($\bullet O_2^-$) were DMSO, IPA, EDTA and BQ, respectively. Figure 4.24 displayed the effects of different scavenging reagents on the photodegradation of 2,4-DCPs. Referring to Figure 4.24, the active radicals that play the dominant roles in the degradation of 2,4-DCPs for $Ag/BiPO_4$ are $\bullet O_2^-$ and •OH. It is clear that the addition of both BQ and IPA heavily suppressed the photodegradation ability of $Ag/BiPO_4$. Figure 4.25 depicted the electron mobility of the photodegradation of 2,4-DCPs using $Ag/BiPO_4$. The scavenging analysis is further justified with the edge potential calculation of semiconductor at point of zero charges using the following equations:

$$E_{VB} = X - E_C + 0.5E_g \quad (4)$$

$$E_{CB} = E_{VB} - E_g \quad (5)$$

Where E_C is the energy of free electrons (~4.5 eV vs normal hydrogen electrode (NHE)); E_{CB} and E_{VB} are the band edge potential for conduction band (CB) and valence band (VB); X is the electronegativity of semiconductor; and Eg is the bandgap energy of semiconductor. The X value of $BiPO_4$ is 6.49 eV (Li et al., 2015). The CB and VB edge potential of $BiPO_4$ are calculated at -0.18eV and 4.17eV, respectively. Ag nanoparticle has a Fermi level ($E_{F(Ag)}$ = 0.4 eV vs. NHE) (Kumat, 2007), that serves as a decent electron trapping center to facilitating efficient electron transfer from both surface and interior of $BiPO_4$ under UV light irradiation (Bi et al., 2012). When $Ag/BiPO_4$ was exposed to sunlight irradiation, the photoexcited electrons will bridge through the bandgap energy from VB to CB, generating electron-hole pairs. Subsequently, electrons in CB of $BiPO_4$ will be transferred to Ag nanoparticles which act as electron

trapping centers due to Ag nanoparticles having less negative assigned Fermi level (E_f) than CB of $BiPO_4$. Furthermore, the transfer of an electron from CB of $BiPO_4$ to Ag nanoparticles will accelerate by the internal electric field (Zhang et al., 2013). This is possible due to the formation of the Schottky junction between the $BiPO_4$ and Ag. Therefore, this phenomenon leads to a lower recombination rate of electron-hole pairs and increment of a photoexcited electron lifetime, contributing to a high yield of photocatalytic efficacy. Furthermore, the electrons at CB of $BiPO_4$ is less negative than the standard redox potential of $O_2/\bullet O_2^-$ (-0.33 eV vs. NHE) leading to a reduction of O_2 absorbed on the surface to $\bullet O_2^-$ radicals. Apart from that, the potential level of aligned Fermi level of Ag nanoparticle was higher than the standard redox potential of $O_2/\bullet O_2^-$ (Leong et al., 2015). Furthermore, Ag nanoparticles can harvest the light absorbance under the sunlight spectrum especially in the visible light region. Therefore, Ag nanoparticles do produce free electrons that will then react with the O_2. Consequently, the O_2 absorbed on the surface was reduced to $\bullet O_2^-$ by Ag nanoparticles through interfacial electrons transfer processes. Both generation of $\bullet O_2^-$ radicals site was responsible for photodegradation of 2,4-DCPs and led to an enhanced photocatalysis performance. Meanwhile, VB level of $BiPO_4$ was more positive than the standard redox potential of $OH^-/\bullet OH$ (+1.99 eV vs. NHE) and $H_2O/\bullet OH$ (+2.38 eV vs NHE) (Zhao et al., 2012; Ni et al., 2016). Thus, the h+ at VB involved in the generation of •OH radicals via oxidation of OH^- and H_2O, which will assist in the degradation of 2,4-DCPs. Due to most of the free electrons generated by $BiPO_4$ are trapped by the Ag nanoparticles, the potential of recombination between the generated electrons and holes in $BiPO_4$ does not make it possible. Hence, the generated holes will

then react with H_2O and form active •OH radicals. Both the formation of $•O_2^-$ and •OH radicals are the main species in enhancing the photodegradation of 2,4-DCPs under sunlight irradiation.

.

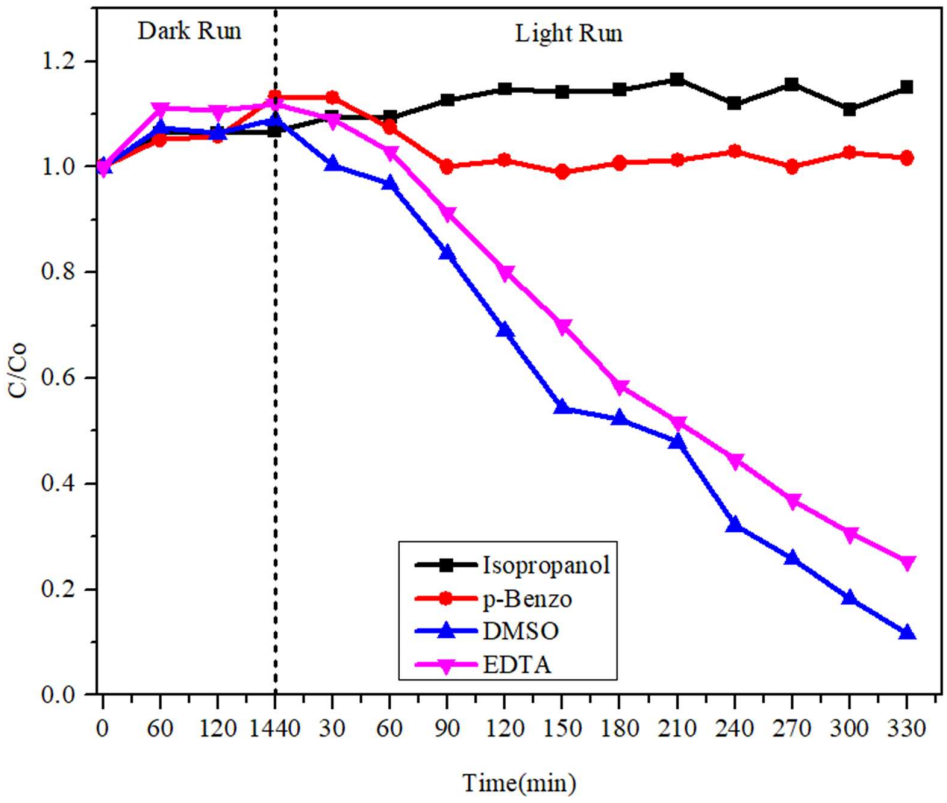

Figure 4.24: Scavenging test on photodegradation of 2.4-DCPs using Ag/$BiPO_4$.

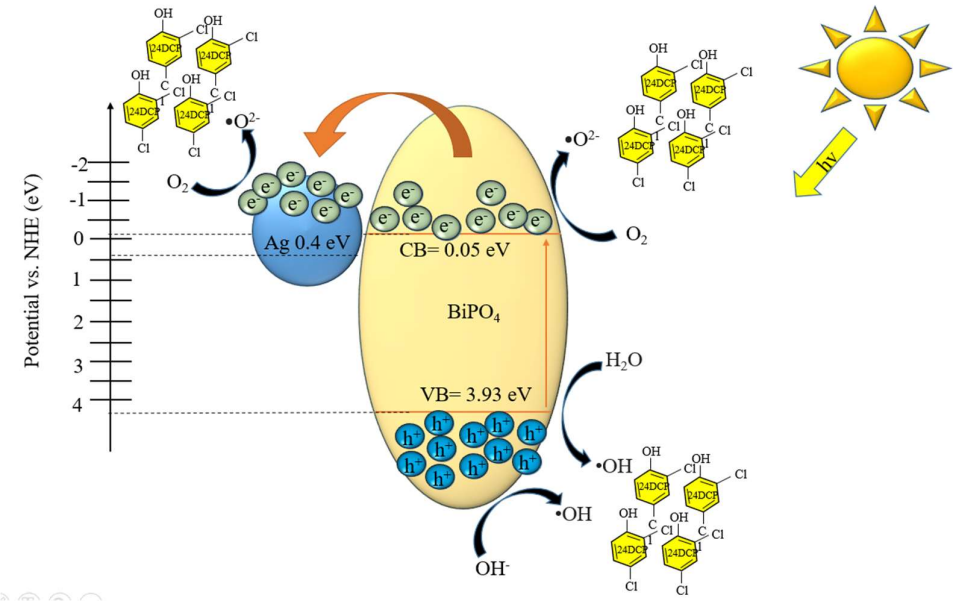

Figure 4.25: Proposed electron and hole mobility of photodegradation of 2,4-DCPs under sunlight irradiation.

The sustainable application of as-prepared nanocomposites is investigated through the recycling test to study the reusability and stability of the photocatalysts. Figure 4.26 shows the photodegradation of 2,4-DCP using 5.0wt% Ag/$BiPO_4$. The experiment was repeated 3 times by reusing the same photocatalysts. The photodegradation result of the repeated test showed decreased yet notable degradation efficiency as shown in Figure 4.26. The slight loss in photodegradation could occur due to the loss of photocatalyst during washing after centrifuging for each recycled test (Chan and Barteau, 2005). Thus, Ag modified $BiPO_4$ nanocomposites proved to have decent stability as photocatalysts.

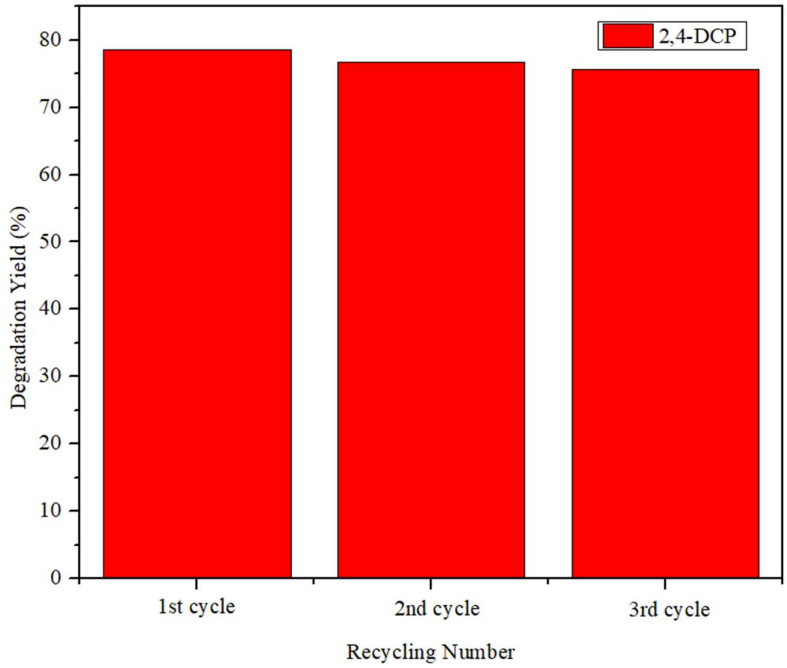

Figure 4.26: Recycling Test of 5.0wt% Ag/$BiPO_4$ on photodegradation of 2,4-DCPs.

4.3 Product cost-benefit analysis

The cost-benefit analysis of photocatalyst synthesis was calculated solely for practical evaluation purposes of this project and comparison was made among each as-prepared photocatalyst. Comparison of cost with the commercial product was not carried out due to difference in pricing for raw materials, electricity utilization, equipment, production quantity and production quality. The electricity bill was evaluated under commercial tariff A category using 200kWh in a month as stated in Tenaga Nasional Berhad (2020) Tariff Book.

$$Electrcity\ consumption = RM\ 0.43\ x\ Consumption\ per\ unit\ kWh \quad (6)$$

According to Table 4.1, 2.5wt% g-C_3N_4/$BiPO_4$ possesses the highest cost-benefit value by saving 37.28% compared to other dopant loading weight percentages of g-C_3N_4/$BiPO_4$ and different dopant loading of Ag/$BiPO_4$.

Hence, 2.5wt% g-C_3N_4/$BiPO_4$ is the best photocatalyst in comparison to other as-synthesized photocatalysts.

Table 4.1: Cost-benefit analysis of 2,4-DCP photodegradation using as-prepared photocatalysts for current study.

	$BiPO_4$	**0.5wt% g-C_3N_4/$BiPO_4$**	**1.5wt% g-C_3N_4/$BiPO_4$**	**2.5wt% g-C_3N_4/$BiPO_4$**	**1.0wt% Ag/$BiPO_4$**	**3.0wt% Ag/$BiPO_4$**	**5.0wt% Ag/$BiPO_4$**
Materials (RM)	8.50	8.52	8.56	8.64	8.52	8.56	8.60
Electric Consumption (RM)	9.44	18.77	18.77	18.77	18.74	18.74	18.74
Total Production Cost (RM)	17.94	27.29	27.33	27.41	27.26	27.3	27.34
Photocatalytic Efficiency after 90min (%)	41.06	55.21	77.23	100	30.39	25.54	33.71
Total Cost per photodegradation efficiency (RM)	43.70	49.43	35.39	27.41	89.70	106.89	81.10
Cost Saved (RM)		-5.73	8.31	16.29	-46	-63.19	-37.4
Cost Saved (%)		-13.11	19	37.28	-105.26	-144.60	-85.58

CHAPTER 5

CONCLUSION AND RECOMMENDATIONS

5.1 Conclusion

In summary, the objectives were achieved and proved in the current study. Pure $BiPO_4$ was successfully synthesized using a simple sol-gel route with bismuth (III) nitrate pentahydrate and ammonium dihydrogen phosphate as precursors. $BiPO_4$ was then modified using urea and silver nitrate, respectively as doping agents. $BiPO_4$/g-C_3N_4 was synthesized via a simple hydrothermal method whereas Ag/$BiPO_4$ was prepared through a facile photodeposition method. Each modification was carried out using different calculated dopant loading.

Different characterizations were conducted to investigate the physical and chemical properties of the as-synthesized nanocomposites. Different dopant loading of g-C_3N_4 and Ag nanoparticles were successfully deposited on $BiPO_4$. FESEM, EDX, HRTEM, FTIR and XRD analysis were used to prove dopant presence in as-synthesized nanocomposites. The optical properties and electron recombination efficiencies of $BiPO_4$/g-C_3N_4 and Ag/$BiPO_4$ were determined through UV-DRS and TRPL analysis.

The photocatalytic performance of $BiPO_4/g\text{-}C_3N_4$ and $Ag/BiPO_4$ were evaluated through photodegradation of 2,4-DCPs under sunlight irradiation. 2.5wt% $BiPO_4/g\text{-}C_3N_4$ and 5.0wt% $Ag/BiPO_4$ exhibited the highest photodegradation efficiencies. In a comparison of both modifications with different dopants, incorporation of $g\text{-}C_3N_4$ to $BiPO_4$ shows better improvement in terms of photodegradation efficiency. 2.5wt% $BiPO_4/g\text{-}C_3N_4$ performed four times better than pure $BiPO_4$ in 2,4-DCPs photodegradation. This is attributed to the superior characteristics of $g\text{-}C_3N_4$ which were proven by the UV-DRS and TRPL analysis. The narrow energy bandgap of $g\text{-}C_3N_4$ broadens the solar spectrum absorbance leading to massive generation of electron-hole pairs. Moreover, the unique polymeric nature of $g\text{-}C_3N_4$ allows multiple excitations of absorption of single-photon contributing to an effective generation of active radicals. According to an electron mobility study, the presence of $g\text{-}C_3N_4$ assists in facilitating photogenerated electrons, which in turn helps hinder the recombination rate of electron-hole pairs, enhancing the photodegradation of 2,4-DCPs.

The active radicals of $BiPO_4/g\text{-}C_3N_4$ and $Ag/BiPO_4$ were determined through a scavenging test. It was found out that photogenerated holes (h^+) and superoxide anion ($\bullet O_2^-$) held the dominant role in 2,4-DCPs photodegradation using $BiPO_4/g\text{-}C_3N_4$ whereas the main active radicals for $Ag/BiPO_4$ are hydroxyl (•OH) and $\bullet O_2^-$ radicals. Subsequently, the recycling test was conducted to evaluate the reusability and stability of both $BiPO_4/g\text{-}C_3N_4$ and $Ag/BiPO_4$ and found out that both as-synthesized nanocomposites still managed to achieve 70% and above of photodegradation even after 3 cycles.

This research portrays g-C_3N_4 and Ag nanoparticles' ability to improve $BiPO_4$ for better photodegradation efficiency in the presence of solar irradiation. The outcome of this research will provide a potential novelty development for facile, green and sustainable photocatalysis of various organic pollutants, energy conversion and energy generation in the future. Last but not least, each of the objectives of this research is achieved.

5.2 Recommendations

In this research, the incorporation of g-C_3N_4 and Ag nanoparticles into $BiPO_4$ exhibited enhancement of 2,4-DCPs photodegradation in the presence of sunlight. However, the following recommendations are taken into considerations for future research works:

i. Photo-remediation of real industrial wastewater and other categories of recalcitrant water pollutants, then evaluate the photodegradation efficiency.
ii. Application of as-synthesized nanocomposites into various materials such as filter membrane.
iii. Recyclability of as-synthesized nanocomposites in the large industrial wastewater treatment plant.

REFERENCES

Abirami, R., Senthil, T.S., Kalpana, S., Kungumadevi, L. and Kang, M., 2020. Hydrothermal synthesis of pure $PbTiO_3$ and silver doped $PbTiO_3$ perovskite nanoparticles for enhanced photocatalytic activity. *Materials Letters*, 279, pp. 128507.

Ahlborg, U.G., Thunberg, T.M. and Spencer, H.C., 1980. Chlorinated phenols: occurrence, toxicity, metabolism, and environmental impact, *Critical Reviews in Toxicology*, 7(1), pp. 1–35.

Ahn, M.Y., Dec, J., Kim, J.E. and Bollag, J.M., 2002. Treatment of 2,4-Dichlorophenol Polluted Soil with Free and Immobilized Laccase. *Journal of Environment Quality*, 31(5), pp. 1509.

Alalm, M.G., Samy, M., Ookawara, S. and Ohno, T., 2018. Immobilization of S-TiO_2 on reusable aluminum plates by polysiloxane for photocatalytic degradation of 2,4-dichlorophenol in water. *Journal of water process engineering*, 26, pp. 329-335.

Ali, W., Ullah, H., Zada, A., Muhammad, W., Ali, S., Shaheen, S., Alamgir, M.K., Ansar, M.Z., Khan, Z.U., Bilal, H. and Yap, P.S., 2020. Synthesis of TiO_2 modified self-assembled honeycomb ZnO/SnO_2 nanocomposites for exceptional photocatalytic degradation of 2, 4-dichlorophenol and bisphenol A. *Science of the Total Environment*, 746, pp. 141291.

Badia-Fabregat, M., Oller, I. and Malato, S., 2015. Overview on Pilot-Scale Treatments and New and Innovative Technologies for Hospital Effluent. *Hospital Wastewaters*, 60, pp. 209-230.

Bellona, C. and Drewes, J.E., 2007. Viability of a low-pressure nanofilter in treating recycled water for water reuse applications: a pilot-scale study. *Water Research*, 41(17), pp. 3948-3958.

Bessière, A., Badot, J.C., Certiat, M.C., Livage, J., Lucas, V. and Baffier, N., 2001. Sol–gel deposition of electrochromic WO_3 thin film on flexible ITO/PET substrate. *Electrochimica Acta*, 46(13-14), pp. 2251-2256.

Bhishma P. P. and Kumar, A., 2015. Biodegradation of 2,4-dichlorophenol by Bacillus endophyticus strain: optimization of experimental parameters using response surface methodology and kinetic study, *Desalination and Water Treatment*, 57(34), pp. 15932-15940.

Bi, Y., Hu, H., Ouyang, S., Jiao, Z., Lu, G. and Ye, J., 2012. Selective growth of Ag_3PO_4 submicro-cubes on Ag nanowires to fabricate necklace-like heterostructures for photocatalytic applications. *Journal of Materials Chemistry*, 22(30), pp. 14847-14850.

Bumajdad, A. and Madkour, M., 2014. Understanding the superior photocatalytic activity of noble metals modified titania under UV and visible light irradiation. *Physical Chemistry Chemical Physics*, 16(16), pp. 7146-7158.

Chan, S.C. and Barteau, M.A., 2005. Preparation of highly uniform Ag/TiO_2 and Au/TiO_2 supported nanoparticle catalysts by photodeposition. *Langmuir*, 21(12), pp. 5588-5595.

Chang, Q., Yang, W., Li, F., Xue, C., Wang, H., Li, N., Liu, H., Yang, J. and Hu, S., 2020. Green, energy-efficient preparation of CDs-embedded $BiPO_4$ heterostructure for better light harvesting and conversion. *Chemical Engineering Journal*, 391, pp. 123551.

Chen, D., Kuang, Z., Zhu, Q., Du, Y. and Zhu, H., 2015. Synthesis and characterization of $CdS/BiPO_4$ heterojunction photocatalyst. *Materials Research Bulletin*, 66, pp. 262-267.

Chen, Y. and Feng, L., 2020. Silver nanoparticles doped TiO_2 catalyzed Suzuki-coupling of bromo aryl with phenylboronic acid under visible light. *Journal of Photochemistry and Photobiology B: Biology*, pp.111807.

Choi, K.J., Kim, S.G., Kim, C.W. and Park, J.K., 2006. Removal efficiencies of endocrine disrupting chemicals by coagulation/flocculation, ozonation, powdered/granular activated carbon adsorption, and chlorination. *Korean Journal of Chemical Engineering,* 23, 399-408.

Chong, M. N., Jin, B., Christopher Chow, W. K. and Chris, S., 2010. Recent Development in photocatalytic water treatment technology: A review. *Water Research*, 44, pp. 2997-3027.

Choquette-Labbe, M., Shewa, W.A., Lalman, J.A. and Shanmugam, S.R., 2014. Photocatalytic degradation of phenol and phenol derivatives using a nano-TiO_2 catalyst: Integrating quantitative and qualitative factors using response surface methodology. *Water*, 6(6), pp. 1785-1806.

Coronado, J.M., Fresno, F., Hernández-Alonso, M.D. and Portela, R., 2013. Design of advanced photocatalytic materials for energy and environmental applications. Springer, London.

Crini, G. and Lichtfouse, E., 2019. Advantages and disadvantages of techniques used for wastewater treatment. *Environmental Chemistry Letters*, 17, pp. 145-155.

Cui, W., Chen, L., Sheng, J., Li, J., Wang, H., Zhou, Y., Sun, Y. and Dong, F., 2020. The pivotal roles of spatially separated charge localization centers on the

moleculer activation and photocatalysis mechanism. *Applied Catalysis B: Environmental*, 262, pp. 118251.

Cui, Y., Zhang, G., Lin, Z. and Wang, X., 2016. Condensed and low-defected graphitic carbon nitride with enhanced photocatalytic hydrogen evolution under visible light irradiation, *Applied Catalysis B: Environmental,* 181, pp. 413-419.

Czaplicka, M., 2004. Sources and transformations of chlorophenols in the natural environment, *Science of the Total Environment*, 322(1–3), pp. 21–39.

Dawoud, T.M., Pavitra, V., Ahmad, P., Syed, A. and Nagaraju, G., 2020. Photocatalytic degradation of an organic dye using Ag doped ZrO_2 nanoparticles: Milk powder facilitated eco-friendly synthesis. *Journal of King Saud University-Science*, 32(3), ppl 1872-1878.

Denchak, M., 2018. *Water Pollution: Everything You Need to Know* [Online]. Available at: https://www.nrdc.org/stories/water-pollution-everything-you-need-know [Accessed:3 December 2020]

Deng, Y., Feng, C., Tang, L., Zeng, G., Chen, Z. and Zhang, M., 2019. Nanohybrid Photocatalysts for Heavy Metal Pollutant Control, *Nanohybrid and Nanoporous Materials for Aquatic Pollution Control*, pp. 125–153.

Dolar, D., Gros, M., Rodriguez-Mozaz, S., Moreno, J., Comas, J., Rodriguez-Roda, I. and Barcelo, D., 2012. Removal of emerging contaminants from municipal wastewater with an integrated membrane system. *Journal of Hazardous Materials*, 239-240, pp. 64-69.

Dou, H., Long, D., Zheng, S. and Zhang, Y., 2018. A facile approach to synthesize graphitic carbon nitride microwires for enhanced photocatalytic H_2 evolution from water splitting under full solar spectrum. *Catalysis Science & Technology*, 8(14), pp. 3599-3609.

Fong, K.E. and Yung, L.Y.L., 2013. Localized surface plasmon resonance: a unique property of plasmonic nanoparticles for nucleic acid detection. *Nanoscale*, 5(24), pp. 12043-12071.

Fulekar, M.H., Singh, A., Dutta, D.P., Roy, M., Ballal, A. and Tyagi, A.K., 2014. Ag incorporated nano $BiPO_{4:}$ sonochemical synthesis, characterization and improved visible light photocatalytic properties. *Rsc Advances*, 4(20), pp. 10097-10107.

Geioushy, R.A., El-Sheikh, S.M., Azzam, A.B., Salah, B.A. and Farida, M., 2020. One-pot fabrication of $BiPO_4/Bi_2S_3$ hybrid structures for visible-light driven reduction of hazardous Cr (VI). *Journal of hazardous materials*, 381, pp. 120955.

Gershon, T., Shin, B., Bojarczuk, N., Hopstaken, M., Mitzi, D.B. and Guha, S., 2015. The role of sodium as a surfactant and suppressor of non-radiative recombination at internal surfaces in Cu_2ZnSnS_4. *Advanced Energy Materials*, 5(2), pp. 1400849.

Ghattavi, S. and Nezamzadeh-Ejhieh, A., 2020. GC-MASS detection of methyl orange degradation intermediates by AgBr/g-C_3N_4: Experimental design, bandgap study, and characterization of the catalyst. *International Journal of Hydrogen Energy*, 45(46), pp. 24636-24656.

Ghazal, S., Akbari, A., Hosseini, H.A., Sabouri, Z., Forouzanfar, F., Khatami, M. and Darroudi, M., 2020 Biosynthesis of silver-doped nickel oxide nanoparticles and evaluation of their photocatalytic and cytotoxicity properties, *Applied Physic A*,126, pp. 480.

Gore, A.C., Crews, D., Doon, L.L., Merrill, M.L., Patisaul, H. and Zota, A., 2014. Introduction of Endocrine Disrupting Chemicals (EDCs), *Endocrine Society*, pp. 1-56.

Gu, F., Wang, S.F., Song, C.F., Lü, M.K., Qi, Y.X., Zhou, G.J., Xu, D. and Yuan, D.R., 2003. Synthesis and luminescence properties of SnO_2 nanoparticles. *Chemical Physics Letters*, 372(3-4), pp. 451-454.

Guerrero-Araque, D., Ramírez-Ortega, D., Acevedo-Peña, P., Zanella, R. and Gómez, R., 2020. Photocatalytic degradation of 2,4-dichlorophenol on ZrO_2–TiO_2: influence of crystal size, surface area, and energetic states. *Journal of Materials Science: Materials in Electronics*, 31(4), pp. 3332-3341.

Guilivo, M., Alda,,L.d.M., Capri, E. and Barcelo, D., 2016. Human exposure to endocrine disrupting compounds: Their role in reproductive systems, metabolic syndrome and breast cancer. A review, *Environmental Research,* 151, pp. 251-264.

Guo, Y., Li, J., Gao, Z., Zhu, X., Liu, Y., Wei, Z., Zhao, W. and Sun, C., 2016. A simple and effective method for fabricating novel p–n heterojunction photocatalyst g-C_3N_4/$Bi_4Ti_3O_{12}$ and its photocatalytic performances. *Applied Catalysis B: Environmental*, 192, pp. 57-71.

Guo, Y., Wang, P., Qian, J., Ao, Y., Wang, C., and Hou, J., 2018 Phosphate Group Grafted Twinned $BiPO_4$ with Significantly Enhanced Photocatalytic Activity: Synergistic Effect of Improved Charge Separation Efficiency and Redox Ability. *Applied Catalysis B,* 234, pp. 90–99.

Habisreutinger, S.N., Schmidt-Mende, L. and Stolarczyk, J.K., 2013. Photocatalytic reduction of CO_2 on TiO_2 and other semiconductors. *Angew Chem Int Ed Engl.*, 52(29), pp. 7372-7408.

Hak, C.H., Leong, K.H., Chin, Y.H., Saravanan, P., Tan, S.T., Chong, W.C. and Sim, L.C., 2020. Water hyacinth derived carbon quantum dots and g-C_3N_4 composites for sunlight driven photodegradation of 2,4-dichlorophenol. *SN Applied Sciences*, 2, pp. 1-14.

Hak, C.H., Sim, L.C., Leong, K.H., Lim, P.F., Chin, Y.H. and Saravanan, P., 2018. M/g-C_3N_4 (M=Ag, Au, and Pd) composite: synthesis via sunlight photodeposition and application towards the degradation of bisphenol A. *Environmental Science and Pollution Research*, 25(25), pp. 25401-25412.

He, K., Xie, J., Liu, Z.Q., Li, N., Chen, X., Hu, J. and Li, X., 2018. Multi-functional Ni_3C cocatalyst/g-C_3N_4 nanoheterojunctions for robust photocatalytic H_2 evolution under visible light. *Journal of Materials Chemistry A*, 6(27), pp.13110-13122.

Huang, C.W., Wu, M.Y. and Lin, Y.W., 2017. Solvothermal synthesis of Ag hybrid $BiPO_4$ heterostructures with enhanced photodegradation activity and stability. *Journal of colloid and interface science*, 490, pp. 217-225.

Huang, F., Yan, A. and Zhao, H., 2016. Influences of Doping on Photocatalytic Properties of TiO_2 Photocatalyst. *Nanotechnology and Nanomaterials*., 2, pp. 31-80.

Huang, H., Qi, H., He, Y., Tian, N., and Zhang, Y., 2013. Enhanced Photocatalytic Activity of Eu^{3+}- and Gd^{3+}- doped $BiPO_4$. *Journal of Material Research,* 28(21), pp. 2977-2984.

Huang, Z., Wu, P., Gong, B., Zhang, X., Liao, Z., Chiang, P.C., Hu, X. and Cui, L., 2017. Immobilization of visible light-sensitive (N, Cu) co-doped TiO_2 onto rectorite for photocatalytic degradation of p-chlorophenol in aqueous solution. *Applied Clay Science*, 142, pp.128-135.

Humayun, M., Hu, Z., Khan, A., Cheng, W., Yuan, Y., Zheng, Z., Fu, Q. and Luo, W., 2019. Highly efficient degradation of 2,4-dichlorophenol over CeO_2/g-C_3N_4 composites under visible-light irradiation: detailed reaction pathway and mechanism. *Journal of hazardous materials*, 364, pp. 635-644.

Iliev, V., Tomova, D., Bilyarska, L., Eliyas, A. and Petrov, L., 2006. Photocatalytic properties of TiO_2 modified with platinum and silver nanoparticles in the degradation of oxalic acid in aqueous solution. *Applied Catalysis B: Environmental*, 63(3-4), pp. 266-271.

Ilisz, I., László, Z. and Dombi, A., 1999. Investigation of the photodecomposition of phenol in near-UV-irradiated aqueous TiO_2 suspensions. I: Effect of charge-trapping species on the degradation kinetics. *Applied Catalysis A: General*, 180(1-2), pp. 25-33.

Jun, D. Jiexiang, X., Mengxia, J., Hongping, L., Hui, X., Huaming, L. and Rong, C., 2015. The synergistic role of carbon quantum dots for the improved photocatalytic performances of Bi_2MoO_6. *Nanoscale*, 7, pp. 11433-11443.

Jun, D., Jiexiang, X., Mengxia, J., Bin, W., Sheng, Y., Qi, Z., Zhigang, C. and Huaming, L., 2016. Advanced photocatalytic performance of graphene-like BN modified BiOBr flower-like materials for the removal of pollutants and mechanism insight. *Applied Catalysis. B*., 183, pp. 254-262.

Kabir, E.R., Rahman, M.S. and Rahman, I., 2015. A review on endocrine disruptors and their possible impacts on human health. Environmental toxicology and pharmacology, 40(1), pp.241-258.

Kamat, P.V., 2007. Meeting the clean energy demand: nanostructure architectures for solar energy conversion. *The Journal of Physical Chemistry C*, 111(7), pp. 2834-2860.

Kolaei, M., Tayebi, M. and Lee, B.K., 2020. The synergistic effects of acid treatment and silver (Ag) loading for substantial improvement of photoelectrochemical and photocatalytic activity of $Na_2Ti_3O_7/TiO_2$ nanocomposite. *Applied Surface Science*, 540(1), pp. 148359.

Lee, K., Mazare, A., and Schmuki, P., 2014. One-Dimensional Titanium Dioxide Nanomaterials: Nanotubes. *Chemical Review,* 114(19), pp. 9385-9454.

Lei, G., Changcun, H. and Jing, L., 2011. Novel visible light-induced g-C_3N_4/Bi_2WO_6 composite photocatalysts for efficient degradation of methyl orange. *Applied Catalysis B*., 108-109, pp. 100-107.

Leong, K.H., Chu, H.Y., Ibrahim, S. and Saravanan, P., 2015a. Palladium nanoparticles anchored to anatase TiO_2 for enhanced surface plasmon resonance-stimulated, visible-light-driven photocatalytic activity. *Beilstein Journal of Nanotechnology*, 6(1), pp.428-437.

Leong, K.H., Liu S.L., Sim, L.C., Saravanan, P., Jang, M. and Ibrahim, S., 2015b. Surface reconstruction of titania with g-C_3N_4 and Ag for promoting efficient electrons migration and enhanced visible light photocatalysis, *Applied Surface Science,* 358, pp. 370-376.

Li, Y., Wang, Y., Huang, Y., Cao, J., Ho, W., Lee, S. and Fan, C., 2015. Controllable synthesis of phosphate-modified BiPO 4 nanorods with high photocatalytic activity: surface hydroxyl groups concentrations effects. *RSC advances*, 5(121), pp.99712-99721.

Li, Z., Yang, S., Zhou, J., Li, D., Zhou, X., Ge, C. and Fang, Y., 2014. Novel mesoporous g-C_3N_4 and $BiPO_4$ nanorods hybrid architectures and their enhanced visible-light-driven photocatalytic performances. *Chemical Engineering J*ournal, 241, pp. 344-351.

Liang, Q., Jin, J., Liu, C., Xu, S., Yao, C. and Li, Z., 2018. A stable $BiPO_4$/g-C_3N_4 nanosheet composite with highly enhanced visible light photocatalytic activity. *Journal of Materials Science: Materials in Electronics*, 29(3), pp. 2509-2516.

Liao, G., Chen, S., Quan, X., Yu, H. and Zhao, H., 2012. Graphene oxide modified gC_3N_4 hybrid with enhanced photocatalytic capability under visible light irradiation. *Journal of Materials Chemistry*, 22(6), pp. 2721-2726.

Liao, J., Cui, W., Li, J., Sheng, J., Wang, H., Chen, P., Jiang, G., Wang, Z. and Dong, F., 2020. Nitrogen defect structure and NO^+ intermediate promoted photocatalytic NO removal on H_2 treated g-C_3N_4. *Chemical Engineering Journal*, 379, pp. 122282.

Liu, J., Sun, Y., Li, Z., Li, S. and Zhao, J., 2011, Photocatalytic hydrogen production from water/methanol solutions over highly ordered Ag-$SrTiO_3$ nanotube arrays, *International Journal of Hydrogen Energy ,* 36, pp. 5811-5816.

Liu, J., Zhang, T., Wang, Z., Dawson, G., and Chen, W., 2011. Simple Pyrolysis of Urea into Graphitic Carbon Nitride with Recyclable Adsorption and Photocatalytic Activity, *Journal of Material Chemistry.*, 21, pp. 14398-401.

Liu, R., Yang, W., He, G., Zheng, W., Li, M., Tao, W. and Tian, M., 2020. Ag-Modified g-C_3N_4 Prepared by a One-Step Calcination Method for Enhanced Catalytic Efficiency and Stability. *ACS omega*, 5(31), pp. 19615-19624.

Liu, Y., Lv, Y., Zhu, Y., Liu, D., Zong, R., and Zhu, Y., 2014. Fluorine Mediated Photocatalytic Activity of $BiPO_4$. *Applied Catalysis B: Environmental,* 147, pp. 851-857.

Liu, Y., Sun, M., Liu, Y., Chen, G. and Zhang, X., 2015. Effects of aging time on phase, morphology, and luminescence by two-photon processes of $BiPO_4$: Er3+, Yb3+ in the solvothermal synthesis. *Optical Materials*, 45, pp. 32-36.

Locatelli, M., Sciascia, F., Cifelli, R., Malatesta, L., Bruni, P. and Croce, F., 2016. Analytical Methods for the endocrine disruptor compounds determination in environmental water samples, *Journal of Chromatography A*, 1434, pp. 1-18.

Lubrano, C., Genovesi, G., Specchia, P., Costantini, D., Mariani, S., Petrangeli, E., Lenzi, A. and Gnessi, L., 2013. Obesity and metabolic comorbidities: environmental diseases?. Oxidative medicine and cellular longevity.

Lv, H., Shen, X., Ji, Z., Qiu, D., Zhu, G. and Bi, Y., 2013. Synthesis of graphene oxide-BiPO4 composites with enhanced photocatalytic properties. *Applied surface science*, 284, pp. 308-314.

Ma, X., Hu, J., He, H., Dong, S., Huang, C. and Chen, X., 2018. New understanding on enhanced photocatalytic activity of g-C_3N_4/$BiPO_4$ heterojunctions by effective interfacial coupling. *ACS Applied Nano Materials*, 1(10), pp. 5507-5515.

Maeda, K., and Domen, K., 2007. New Non-Oxide Photocatalysts Designed for Overall Water Splitting under Visible Light, *Journal of Physical Chemistry C*, 111(22), pp. 7851–7861.

Mafa, P.J., Mamba, B.B. and Kuvarega, A.T., 2020. Photoelectrocatalytic evaluation of EG-CeO_2 photoanode on degradation of 2,4-dichlorophenol. *Solar Energy Materials and Solar Cells*, 208, pp. 110416.

Mahato, T.H., Prasad, G.K., Singh, B., Acharya, J., Srivastava, A.R. and Vijayaraghavan, R., 2009. Nanocrystalline zinc oxide for the decontamination of sarin. *Journal of hazardous materials*, 165(1-3), pp. 928-932.

Mamba, G. and Mishra, A. K., 2016. Graphitic carbon nitride (g-C_3N_4) nanocomposites: A new and exciting generation of visible light driven photocatalysts for environmental pollution remediation, *Applied Catalysis B: Environmental,* 198, pp. 347–377.

Matafonova, G., Shirapova, G., Zimmer, C., Giffhorn, F., Batoev, V. and Kohring, G., 2006. Degradation of 2,4-dichlorophenol by Bacillus sp. isolated from an aeration pond in the Baikalsk pulp and paper mill (Russia), *International Biodeterioration and Biodegradation*, 58, pp. 209–212.

Mehrabani-Zeinabad, M., 2016. *Advanced Oxidative Process for Treatment of Emerging Contaminants in Water*., PhD. University of Calgary.

Mills, A., Davies, R.H. and Worsley, D., 1993. Water purification by semiconductor photocatalysis, *Chemistry Society Review*, 22, pp. 417-425.

Molinari, R., Borgese, M., Drioli, E., Palmisano, L. and Schiavello, M., 2002. Hybrid processes coupling photocatalysis and membranes for degradation of organic pollutants in water, *Catalysis Today*, 75(1-4), 77–85.

Naciri, Y., Bouddouch, A., Bakiz, B., Taoufyq, A., Ezahri, M. and Benlhachemi, A., 2020. Photocatalytic degradation of sulfadiazine by $Zn_3(PO_4)_2/BiPO_4$ composites upon UV light irradiation. *Materials Today: Proceedings*, 22, pp. 48-51.

Nainani, R., Thakur, P. and Chaskar, M., 2012. Synthesis of silver doped TiO_2 nanoparticles for the improved photocatalytic degradation of methyl orange. *Journal of Materials Science Nd Engineering B*, 2(1), pp. 52-58.

Ni, Z., Dong, F., Huang, H. and Zhang, Y., 2016. New insights into how Pd nanoparticles influence the photocatalytic oxidation and reduction ability of g-C_3N_4 nanosheets. *Catalysis Science & Technology*, 6(16), pp. 6448-6458.

Ong, W., Ta, L., Ng, Y., Yong, S. and Chai, S., 2016. Graphitic Carbon Nitride ($g\text{-}C_3N_4$)-Based Photocatalysts for Artificial Photosynthesis and Environmental Remediation: Are We a Step Closer to Achieving Sustainability? *Chemistry Review,* 116(12), pp. 7159-7329.

Palominos, R., Freer, J., Mondaca, M.A. and Mansilla, H.D., 2008. Evidence for hole participation during the photocatalytic oxidation of the antibiotic flumequine. *Journal of photochemistry and photobiology A: chemistry*, 193(2-3), pp.139-145.

Pan, C. and Zhu, Y., 2010. New Type of $BiPO_4$ Oxy-Acid Salt Photocatalyst with High Photocatalytic Activity on Degradation of Dye. *Environmental Science & Technology,* 44(14), pp. 5570–5574.

Pan, C. and Zhu, Y., 2011a. Size-controlled synthesis of $BiPO_4$ nanocrystals for enhanced photocatalytic performance. *Journal of Materials Chemistry*, 21(12), pp. 4235-4241.

Pan, C., Li, D., Ma, X., Chen, Y. and Zhu, Y., 2011b. Effects of distortion of PO_4 tetrahedron on the photocatalytic performances of $BiPO_4$. *Catalysis Science & Technology*, 1(8), pp. 1399-1405.

Pan, C., Xu, J., Wang, Y., Li, D., and Zhu, Y., 2012. Dramatic Activity of C_3N_4 /$BiPO_4$ Photocatalyst with Core/Shell Structure Formed by Self-Assembly. *Advanced Functional Materials,* 22, pp. 1518–1524.

Pan, X. and Xu, Y.J., 2013. Defect-mediated growth of noble-metal (Ag, Pt, and Pd) nanoparticles on TiO_2 with oxygen vacancies for photocatalytic redox reactions under visible light. *The Journal of Physical Chemistry C*, 117(35), pp. 17996-18005.

Paul, D.R., Sharma, R., Panchal, P., Nehra, S.P., Gupta, A.P. and Sharma, A., 2020. Synthesis, characterization and application of silver doped graphitic carbon nitride as photocatalyst towards visible light photocatalytic hydrogen evolution. *International Journal of Hydrogen Energy*, 45(44), pp. 23937-23946.

Paul, K.K. and Giri, P.K., 2018. Plasmonic metal and semiconductor nanoparticle decorated TiO_2-based photocatalysts for solar light driven photocatalysis, *Reference Module in Chemistry, Molecular Sciences and Chemical Engineering,* pp. 786-794.

Qi, K., Cheng, B., Yu, J., and Ho, W., 2017. A review on TiO_2 -based Z-scheme photocatalysts, *Chinese Journal of Catalysis*, 38(12), pp. 1936–1955.

Ramos-Ramírez, E., Gutiérrez-Ortega, N.L., Tzompantzi-Morales, F., Barrera-Rodríguez, A., Castillo-Rodríguez, J.C., Tzompantzi-Flores, C., Santolalla-Vargas, C.E. and Guevara-Hornedo, M.D.P., 2020. Photocatalytic Degradation of 2,4-Dichlorophenol on NiAl-Mixed Oxides Derivatives of Activated Layered Double Hydroxides. *Topics in Catalysis*, pp. 1-18.

Ran, M., Wang, H., Cui, W., Li, J., Chen, P., Sun, Y., Sheng, J., Zhou, Y., Zhang, Y. and Dong, F., 2019. Light-induced generation and regeneration of oxygen vacancies in $BiSbO_4$ for sustainable visible light photocatalysis. *ACS applied materials & interfaces*, 11(51), pp. 47984-47991.

Ranjit, P. J. D., Palanivelu, K., and Lee, C.S., 2008. Degradation of 2,4-dichlorophenol in aqueous solution by sono-Fenton method. *Korean Journal of Chemical Engineering*, 25(1), pp. 112–117.

Rao, B.G., Mukherjee, D. and Reddy, B.M., 2017. Novel approaches for preparation of nanoparticles. In *Nanostructures for novel therapy* (pp. 1-36). Elsevier.Li, Y., White, T.J. and Lim, S.H., 2004. Low-temperature synthesis

and microstructural control of titania nano-particles. *Journal of solid-state chemistry*, 177(4-5), pp. 1372-1381.

Romero, B., Bruque, S., Aranda, M.A. and Iglesias, J.E., 1994. Syntheses, crystal structures, and characterization of bismuth phosphates. *Inorganic Chemistry*, 33(9), pp. 1869-1874.

Samer, M. 2015. Biological and Chemical Wastewater Treatment Processes. *Wastewater Treatment Engineering*, 1, pp. 1-2.

Samsudin, M.F.R., Ullah, H., Bashiri, R., Mohamed, N.M., Sufian, S. and Ng, Y.H., 2020. Experimental and DFT insights on microflower g-C_3N_4/$BiVO_4$ photocatalyst for enhanced photoelectrochemical hydrogen generation from lake water. *ACS Sustainable Chemistry & Engineering*, 8(25), pp. 9393-9403.

Serpone, N. and Emeline, A.V., 2012. Semiconductor photocatalysis—Past, present, and future outlook, *Journal of Physical Chemistry Letters*, 3, pp. 673-677.

Serpone, N., Emeline, A.V., Horihoshi, S., Kuznetsov, V.N. and Ryahchuk, V.K., 2012. On the genesis of heterogeneous photocatalysis: a brief historical perspective in the period 1910 to the mid-1980s, *Photochemical and Photobiological Sciences*, 11, pp. 1121-1150.

Sim, L.C., Koh, K.S., Leong, K.H., Chin, Y.H., Abd Aziz, A. and Saravanan, P., 2020. In situ growth of g-C_3N_4 on TiO_2 nanotube arrays: Construction of heterostructures for improved photocatalysis properties. *Journal of Environmental Chemical Engineering*, 8(1), pp. 103611.

Singh, J. and Basu, S., 2020. Synthesis of mesoporous magnetic Fe_2O_3/g-C_3N_4 monoliths for Rhodamine B removal. *Microporous and Mesoporous Materials*, 303, pp. 110299.

Sobana, N., Muruganadham, M. and Swaminathan, M., 2006. Nano-Ag particles doped TiO2 for efficient photodegradation of direct azo dyes. *Journal of Molecular Catalysis A: Chemical*, 258(1-2), pp. 124-132.

Stoyanova, Z. and Harizanova, H., 2019. Impact of Agriculture on Water Pollution. *Agrofor*, 4(1).

Singh, J., Yadav, P., Pal, A.K. and Mishra, V., 2020. Water pollutants: Origin and status. In *Sensors in Water Pollutants Monitoring: Role of Material* (pp. 5-20). Springer, Singapore.

Tan, G., She, L., Liu, T., Xu, C., Ren, H. and Xia, A., 2017. Ultrasonic chemical synthesis of hybrid mpg-C_3N_4/$BiPO_4$ heterostructured photocatalysts with improved visible light photocatalytic activity. *Applied Catalysis B: Environmental*, 207, pp. 120-133.

Tian, Q., Ran, M., Fang, G., Ding, L., Pan, A., Shen, K. and Deng, Y., 2020. $ZnAl_2O_4$/$BiPO_4$ composites as a heterogeneous catalyst for photo-Fenton treatment of textile and pulping wastewater. *Separation and Purification Technology*, 239, pp. 116574.

Tian, X., Xu, T., Wang, Y. and Meng, S., 2017. Hierarchical h-, m-and n-$BiPO_4$ microspheres: facile synthesis and application in the photocatalytic decomposition of refractory phenols and benzene. *RSC advances*, 7(58), pp. 36705-36713.

Tijani, J.O., Fatoba, O.O and Petrik, L.F., 2013. A Review of Pharmaceuticals and Endocrine-Disrupting Compounds: Sources, Effects, Removal, and Detections. *Water, Air, & Soil Pollution*, 224, pp. 1770-1798.

Tomei, M. C., Annesini, M. C. and Daugulis, A. J., 2012. 2,4-Dichlorophenol removal in a solid–liquid two phase partitioning bioreactor (TPPB): kinetics of

absorption, desorption and biodegradation. *New Biotechnology*, 30(1), pp. 44–50.

Tu, L., Hou, Y., Yuan, G., Yu, Z., Qin, S., Yan, Y., Zhu, H., Lin, H., Chen, Y. and Wang, S., 2020. Bio-photoelectrochemcial system constructed with $BiVO_4$/RGO photocathode for 2,4-dichlorophenol degradation: $BiVO_4$/RGO optimization, degradation performance and mechanism. *Journal of Hazardous Materials*, 389, pp. 121917.

Walton, R.I., 2002. Subcritical solvothermal synthesis of condensed inorganic materials. *Chemical Society Reviews*, 31(4), pp. 230-238.

Wang, C., Zhang, G., Zhang, C., Fan, W. and Shi, W., 2014. A facile one-step solvothermal synthesis of $BiPO_4$-graphene nanocomposites with enhanced photocatalytic activity. *Journal of Colloid and Interface Science*, 435, pp. 156-163.

Wang, K., Li, Y., Li, J. and Zhang, G., 2020. Boosting interfacial charge separation of $Ba_5Nb_4O_{15}$/g-C_3N_4 photocatalysts by 2D/2D nanojunction towards efficient visible-light driven H_2 generation. *Applied Catalysis B: Environmental*, 263, pp. 117730.

Wang, Q., Wang, P., Xu, P., Li, Y., Duan, J., Zhang, G., Hu, L., Wang, X. and Zhang, W., 2020. Visible-light-driven photo-Fenton reactions using $Zn_{1-1.5\ x}Fe_xS$/g-C_3N_4 photocatalyst: Degradation kinetics and mechanisms analysis. *Applied Catalysis B: Environmental*, 266, pp. 118653.

Wang, T., Lang, J., Zhao, Y., Su, Y., Zhao, Y. and Wang, X., 2015. Simultaneous doping and heterojunction of silver on Na 2 Ta 2 O 6 nanoparticles for visible light driven photocatalysis: the relationship between

tunable optical absorption, defect chemistry and photocatalytic activity. *CrystEngComm*, 17(35), pp. 6651-6660.

Wang, X., and Li, C., 2018 Roles of Phase-Junction in Photocatalysis and Photoelectrocatalysis, *Journal of Physical Chemistry C,* 122(37), pp. 21083-21096.

Wang, Y., Luo, W., Jiang, W., Wei, Z. and Zhu, Y. 2019. Controlled synthesis of g-C_3N_4@$BiPO_4$ core–shell nanorods via low temperature reassembled strategy, *Materials Today Advances*, 1, pp. 100006.

Wen, J., Xie, J., Chen, X. and Li, X., 2017. A review on g-C_3N_4-based photocatalysts. *Applied surface science*, 391, pp. 72-123.

Westerhoff, P., Yoon, Y., Snyder, S and Wert, E., 2005. Fate of Endocrine-DIsruptor, Pharmaceutical, and Personal Care Product Chemicals during Simulated Drinking Water Treatment Processes. *Environmental Science & Technology Letter.,* 39(17), pp. 6649-6663.

Wu, Y., Liu, H., Zhang, J. and Chen, F., 2009. Enhanced photocatalytic activity of nitrogen-doped titania by deposited with gold. *Journal of Physical Chemistry. C.*, 113(33), pp. 14689-14695.

Wu, Z., Zhang, Y., Wang, X. and Zou, Z., 2017. Ag@$SrTiO_3$ nanocomposite for super photocatalytic degradation of organic dye and catalytic reduction of 4-nitrophenol. *New Journal of Chemistry*, 41(13), pp. 5678-5687.

Xia, J., Zhao, J., Chen, J., Di, J., Ji, M., Xu, L., Chen, Z. and Li, H., 2017. Facile fabrication of g-C_3N_4/$BiPO_4$ hybrid materials via a reactable ionic liquid for the photocatalytic degradation of antibiotic ciprofloxacin. *Journal of Photochemistry and Photobiology A: Chemistry*, 339, pp.59-66.

Xiang, Q., Cheng, B. and Yu, J., 2015. Graphene-based photocatalysts for solar-fuel generation. *Angewandte Chemie International Edition*, 54(39), pp. 11350-11366.

Xu, H., Xu, Y., Li, H., Xia, J., Xiong, J., Yin, S., Huang, C. and Wan, H., 2012. Synthesis, characterization and photocatalytic property of AgBr/$BiPO_4$ heterojunction photocatalyst. *Dalton transactions*, 41(12), pp. 3387-3394.

Xu, J., Li, L., Guo, C., Zhang, Y. and Meng, W., 2013. Photocatalytic Degradation of Carbamazepine by Tailored $BiPO_4$: Efficiency, Intermediates and Pathway. *Applied Catalysis B: Environmental,* 130-131, pp. 285-292.

Yang, C., Qin, J., Xue, Z., Ma, M., Zhang, X., and Liu, R., 2017. Rational design of carbon-doped TiO_2 modified g-C_3N_4 via in-situ heat treatment for drastically improved photocatalytic hydrogen with excellent photostability, *Nano Energy,* 41, pp. 1-9.

Yang, M., Park, M.S. and Lee, H.S., 2006. Endocrine disrupting chemicals: human exposure and health risks. Journal of Environmental Science and Health Part C, 24(2), pp.183-224.

Yang, X. and Wang, D., 2018. Photocatalysis: from fundamental principles to materials and applications. *ACS Applied Energy Materials*, 1(12), pp. 6657-6693.

Yoshimura, M. and Byrappa, K., 2008. Hydrothermal processing of materials: past, present and future. *Journal of Materials Science*, 43(7), pp. 2085-2103.

Zhang, D., Su, C., Yao, S., Li, H., Pu, X. and Geng, Y., 2020. Facile in situ chemical transformation synthesis, boosted charge separation, and increased photocatalytic activity of $BiPO_4$/BiOCl p-n heterojunction photocatalysts under

simulated sunlight irradiation. *Journal of Physics and Chemistry of Solids*, 147, pp. 109630.

Zhang, G., Zhang, T., Li, B., Jiang, S., Zhang, X., Hai, L., Chen, X. and Wu, W., 2018. An ingenious strategy of preparing TiO_2/g-C_3N_4 heterojunction photocatalyst: In situ growth of TiO_2 nanocrystals on g-C_3N_4 nanosheets via impregnation-calcination method. *Applied Surface Science*, 433, pp. 963-974.

Zhang, M., Hou, Z., Ma, W., Zhao, X., Ma, C., Zhu, Z., Yan, Y. and Li, C., 2018. Fabrication of a Visible-Light In_2S_3/$BiPO_4$ heterojunction with enhanced photocatalytic activity, *New Journal of Chemistry*, 42, pp. 15136-15145.

Zhang, P., Zhang, J. and Gong, J., 2014. Tantalum-based semiconductors for solar water splitting. *Chemical Society Reviews*, 43(13), pp. 4395-4422.

Zhang, Y., Fan, H., Li, M. and Tian, H., 2013. Ag/$BiPO_4$ heterostructures: synthesis, characterization and their enhanced photocatalytic properties. *Dalton Transactions*, 42(36), pp. 13172-13178.

Zhang, Y., Selvaraj, R., Sillanpää, M., Kim, Y. and Tai, C.W., 2014. The influence of operating parameters on heterogeneous photocatalytic mineralization of phenol over BiPO4. *Chemical Engineering Journal*, 245, pp. 117-123.

Zhang, Y.H., Pan, Q.W., Chai, G.Q., Liang, M.R., Dong, G.P., Zhang, Q., and Qiu, J., 2013. Synthesis and luminescence mechanism of multicolor-emitting g-C_3N_4 nanopowders by low temperature thermal condensation of melamine, *Scientific Reports,* 3(1), pp. 1943.

Zhao, H., Tian, F. and Wang, R., 2014. R, Chen, A Review on bismuth-related nanomaterials for photocatalysis, *Reviews in Advanced Sciences and Engineering,* 3, pp.3-27.

Zhao, S., Chen, S., Yu, H. and Quan, X., 2012. g-C_3N_4/TiO_2 hybrid photocatalyst with wide absorption wavelength range and effective photogenerated charge separation. *Separation and Purification Technology*, 99, pp. 50-54.

Zhao, Y., Shi, H., Yang, D., Fan, J., Hu, X. and Liu, E., 2020. Fabrication of a Sb_2MoO_6/g-C_3N_4 photocatalyst for enhanced RhB degradation and H_2 generation. *The Journal of Physical Chemistry C*, 124(25), pp. 13771-13778.

Zheng, Y., Zhang, Z., and Li, C., 2017. A comparison of graphitic carbon nitrides synthesized from different precursors through pyrolysis, *Journal of Photochemistry and Photobiology A: Chemistry*, 332, pp. 32-44.

Zhong, H., Mirkovic, T. and Scholes, G.D., 2011. Nanocrystal synthesis. In *Comprehensive nanoscience and technology*, pp. 153-201.

Zhu, Y., Liu, Y., Lv, Y., Ling, Q., Liu, D., and Zhu, Y., 2014. Enhancement of Photocatalytic Activity for $BiPO_4$ via Phase Junction, *Journal of Material Chemistry A*, 2, pp. 13041–13048.

Zoeller, R.T., Brown, T.R., Doan, L.L., Gore, A.C., Skakkebaek, N.E., Soto, A.M., Woodruff, T.J. and Vom Saal, F.S., 2012. Endocrine-disrupting chemicals and public health protection: a statement of principles from The Endocrine Society. *Endocrinology*, 153, pp. 4097-4110.

Zong, S., Wei, W., Cui, H., Jiang, Z., Lu, X., Zhang, M., and Xie, J., 2015. A novel Synthesis of P/$BiPO_4$ Nanocomposites with Enhanced Visible-Light Photocatalysis. *Materials Research Innovations,* 19(5), pp. 361-367.

Zou, X., Dong, Y., Chen, Z., Dong, D., Hu, D., Li, X. and Cui, Y., 2016. Synthesis and characterization of $BiPO_4$/g-C_3N_4 nanocomposites with

significantly enhanced visible-light photocatalytic activity for benzene degradation. *RSC Advances.,* 6, pp. 20664–670.

Zou, X., Dong, Y., Li, X., Zhao, Q., Cui, Y. and Lu, G., 2015. Inorganic–organic photocatalyst $BiPO_4$/g-C_3N_4 for efficient removal of gaseous toluene under visible light irradiation. *Catalysis Communications*, 69, pp. 109-113.

APPENDICES

Appendix A: Experimental Setup for Photocatalytic Evaluation

LIST OF PUBLICATION

Ng, J.J., Leong, K.H., Sim, L.C., Chin, Y.H. and Pichiah, S., 2020, September. Visible light responsive BiPO4/g-C3N4 for enhanced photocatalysis of 2-4 dichlorophenol under solar irradiation. In *IOP Conference Series: Materials Science and Engineering* (Vol. 917, No. 1, p. 012007). IOP Publishing.

Ng, J.J., Leong, K.H., Sim, L.C., Oh, W.D., Dai, C. and Saravanan, P., 2020. Environmental remediation using nano-photocatalyst under visible light irradiation: the case of bismuth phosphate. In *Nanomaterials for Air Remediation* (pp. 193-207). Elsevier.